ABSTRACT

This dissertation reports on a precise measurement of the parity-violating asymmetry in electron-electron (Møller) scattering at a four-momentum transfer $Q^2 = 0.03$ $(\mathrm{GeV/c})^2$. The observed parity-violating asymmetry is $A_{PV} = -128 \pm 14$ (stat.) $\pm$ 12 (syst.) $\times 10^{-9}$. This is the most precise asymmetry ever measured in a parity-violating electron scattering. In the context of the Standard Model, the A_{PV} result determines the weak mixing angle, which is one of the fundamental parameters of the model. The result is $\sin^2\theta_W^{eff} = 0.2403 \pm 0.0014$, which is consistent with the Standard Model expectation at the current level of precision. The comparison between this measurement of the weak mixing angle at low Q^2 and at the Z^0 pole establishes the running of $\sin^2\theta_W$ with 6.5σ significance.

In addition, we report on the first observation of a transverse asymmetry in electron-electron scattering. The observed asymmetry is $A_T^{M\o ller} = 2.7 \times 10^{-6}$, which is consistent with the theoretical predictions. We also provide a new measurement of the transverse asymmetry in ep scattering $A_T^{ep} = 2 \times 10^{-6}$.

The consistency of the result with the theoretical prediction provides new limits on the TeV scale physics. A limit of 0.9 TeV was set on the mass of the extra Z' boson in the SO(10) Model. A limit of 14 TeV and 6 TeV was set on the compositness scales Λ_{ee}^{+} and Λ_{ee}^{-}, respectively. Finally a limit of 0.2 TeV was set on ratio of the doubly-charged Higgs mass to the $ee\Delta$ coupling $g_{ee\Delta}^2/m_\Delta^2$.

A SEARCH FOR NEW PHYSICS AT THE TEV SCALE VIA A PRECISE MEASUREMENT OF THE WEAK MIXING ANGLE IN MØLLER SCATTERINGF

WALED S. EMAM

DISSERTATION

Submitted in partial fulfillment of the requirements for the
degree of Doctor of Philosophy in Physics
in the Graduate School of Syracuse University

December 2004

Approved ....
Professor Paul Souder

Date

Contents

List of Figures

List of Tables

Acknowledgements

Many people from all over the world have helped me with my research. Among them, I am very grateful to my advisor Prof. Paul Souder, for his suggestions, help and encouragement. I acknowledge the time and effort that he has spent to teach and direct me. Paul stood beside me in more than one situation as a father, not as an advisor, and this is what I have likeed the most about him.

I received, and continue to receive, much academic counseling from Prof. Yury Kolomensky of University of California at Berkeley. I want to thank him especially for the detailed comments and suggestions on this and other work, his support and advice in other areas of academic life, and for inviting me to work with him at UC Berkeley. I would like to thank Profs. Krishna Kumar, Emlyn Hughes, Mike Woods, and Peter Bosted - the people who did their best to create E158 - for the help, support and advice.

I would also like to express appreciation to my college and my friend, Imran Younus. Over the past five years Imran has been witness to the many ups and downs of my own life. When I was at SLAC, I met wonderful people. Carlos, Mark, Pete, Klejda, Dave, Antonin, Lisa and Kent shared with me very hard shifts as well as very nice stories. I would also like to thank Mark Cooke, Brook, Khalid Kadir, Moatasem, Sohail, Ahmed, Mazen, Rusty, Talaat, Khalid Sarsour, and Mansour for welcoming me at UC Berkeley.

Many people on the faculty, staff, and graduate students of the Syracuse Graduate School assisted and encouraged me in various ways during my course of studies. I am especially grateful to Profs. Joseph Schechter, A.P. Balachandran, Mark Bowick, Eric Schiff, Tomasz Skwarnicki, Rafael Sorkin, Mark Trodden, and Richard

Holmes for all that they have taught me. My graduate studies would not have been the same without the social challenges provided by the staff of the physics department, and particularly, Diane Sanderson, Lee Pesce, Joyce McDonough, and Cindy Urtz.I would like to thank all my student-colleagues in the department. I am particularly thankful to my friends Abdou, Sherif, Badis, Sofiane, and Chaouki.

I would like to express my thanks to the High Energy staff members at the International Center for Theoretical Physics (ICTP) ate Trieste, not only for teaching me High Energy Physics, but also for their unlimited efforts and supports to make me think as a physicist. The faculty in my undergrad institute, Ain Shams University at Cairo, who helped me in various ways in the context of my research life are many. Profs. Shaaban Khalil and Shoukry Hassan particularly deserve my deepest thanks and respect.

Two people deserve special thanks. My friend, Osama, and his family, opened their hearts and home to me. His wife and my sister, Judy, made me feel as I am living among my family. Their daughter, Hana, gave me very pleasant time playing with her. My landlady and my friend, Bronya Feldmann, deserves many thanks for her help, kindness, support, welcoming me at her home, and giving me the opportunity to live with a very wonderful cat, Max, which used to give me a nice company after having a very hard day fighting with the beam systematics.

There are two persons above all others who deserve my deepest thanks and respect for their continued support not only during the writing of this dissertation but also through my whole entire life: my parents. I could not have done it without them. My sisters, Samah and Mervat, and my brother, Ahmed, deserve special thanks for their support and care over the years. Finally, I appreciate the patience of my fiancee, Hanan, who keeps waiting for me till E158 is over, so that we can get married. I would like to thank her for her support, care, and love.

إلى أبى وأمى
أهدى اليكما ما أنعم الله على به من علمه
جزاكم الله عنى خير الجزاء

Chapter 1

Parity-Violating Asymmetry in Longitudinally Polarized Møller Scattering

1.1 Introduction

In the 1970s, particle physics was reformulated when it was shown that all interactions among elementary particles except for gravity can be described by one theory called the Standard Model. This model, which has been verified experimentally, is considered to be the most successful theory so far. One of the essential parts of the Standard Model is the electroweak theory, which unifies electromagnetic and weak interactions. The theory contains a parameter, the weak mixing angle denoted by $\sin^2\theta_W$, which must be determined by experiments. This parameter is one of the most important parameters of the Standard Model. Several experiments have measured this parameter at different energy scale using different elementary particles.

Although the Standard Model has answered many important questions, it is believed to be incomplete. More inclusive theories like Superstrings and Supersymmetry are candidates to complete the Standard Model. However, none of these theories has been verified experimentally yet. The precise measurement of any of the Standard Model parameters, for example, the weak mixing angle, is important since any significant deviation from the predicted value will be a signal of a "new physics".

1.2 Electroweak Unification

In 1961, Glashow [1] published the first paper on the unification of weak and electromagnetic interactions; his original aim was to combine the weak and electromagnetic interactions into a single theory, so that they would appear not as unrelated phenomena, but rather as different manifestations of a fundamental "electroweak" interaction. Because of the enormous disparity in strength between weak and electromagnetic forces, Glashow suggested that the weak interactions were mediated by extremely massive particles. Of course, this immediately raised another question: Why is the electromagnetic mediator, γ, massless, when the weak mediators, $W^{\pm}$ and Z^0, are so heavy?

Glashow had no particularly good answer, but in 1967, Weinberg and Salaam [2] provided a solution –"Higgs mechanism." They formulated Glashow's model as a "spontaneously broken gauge theory". Then, in 1971, 't Hooft [3] demonstrated that the Glashow-Weinberg-Salaam scheme is renormalizable.

1.2.1 Left-Handed and Right-Handed Fermion Fields.

The weak interactions violate the conservation of parity while the electromagnetic interactions do not. Therefore, there is a difference in the structure between the electromagnetic and weak couplings: The electromagnetic vertex is purely vectorial (γ), whereas the weak vertex contains vector and axial vector parts. In particular, the $W^{\pm}$ coupling is mixed $V-A$ in character ($\gamma^{\mu}(1-\gamma^5)$) [4]. In order to build a unified theory, however, we need to have a unified structure.

This difficulty is solved by absorbing the matrix $(1-\gamma^5)$ into the particle spinor itself in order to create "chiral" fermion states. We then define the "right-handed" and "left-handed" spinor:

$$\psi_R = \frac{1+\gamma^5}{2}\psi, \quad \psi_L = \frac{1-\gamma^5}{2}\psi. \tag{1.1}$$

The neutrinos are known to be nearly massless. By assuming that they are exactly massless, the right-handed state of the neutrinos does not exist. Therefore, the left-handed leptons will form doublets whereas the right-handed ones will form singlets:

$$\begin{bmatrix} \nu_e \\ e \end{bmatrix}_L, e_R \quad \begin{bmatrix} \nu_\mu \\ \mu \end{bmatrix}_L, \mu_R \quad \begin{bmatrix} \nu_\tau \\ \tau \end{bmatrix}_L, \tau_R. \tag{1.2}$$

Consider, for example, the coupling of an electron and a neutrino to the W^-. The contribution to the amplitude ($\mathcal{M}$) from this vertex is given by

$$j_\mu^- = \overline{\nu}\gamma_\mu\left(\frac{1-\gamma^5}{2}\right)e, \tag{1.3}$$

which can be rewritten in terms of the chiral spinors:

$$j_\mu^- = -\overline{\nu}_L\gamma_\mu\left(\frac{1-\gamma^5}{2}\right)e_L. \tag{1.4}$$

The weak vertex factor is now purely vectorial, but it couples only left-handed electrons to left-handed neutrinos. It is still structurally different from the fundamental vertex in QED. However, the electromagnetic current itself can be written in terms of chiral spinors:

$$j_\mu^{em} = -\overline{e}\gamma_\mu e = \overline{e}_L\gamma_\mu e_L - \overline{e}_R\gamma_\mu e_R. \tag{1.5}$$

Now we can begin to build a unified theory.

1.2.2 Electroweak Lagrangian of Leptons

The construction of the Standard Model has been described in many review articles and texts [4–7]. We will try to present this construction for the importance of the concepts of this model. In the following, we will build a Lagrangian that is a non-abelian gauge invariant under the symmetry group $SU(2) \otimes U(1)$. Since the procedure is identical for all three families, we shall consider only one of them–say the electron family:

$$\psi_L = \begin{bmatrix} \nu_e \\ e \end{bmatrix}_L, \psi_R = e_R. \tag{1.6}$$

To construct the theory, we must use the "minimal coupling rule", in which we substitute ∇_μ for ∂_μ, in order to convert a globally invariant Lagrangian into a locally invariant one. However, the covariant derivative, ∇_μ, introduces a new vector field that requires its own free Lagrangian. Under the action of $SU(2)$ we demand the following behavior

$$\psi_L \to e^{i\theta(\mathbf{x}).\hat{\mathbf{T}}}\psi_L, \quad \psi_R \to e^{i\theta(\mathbf{x}).\hat{\mathbf{T}}}\psi_R, \tag{1.7}$$

where $\hat{T}_r = \hat{\tau}_r/2$, $r = 1, 2, 3$ are generators of the symmetry group, which can be represented as Pauli matrices $\hat{\tau}_r$. The covariant derivatives are then constructed as follows:

$$\nabla_\mu \psi_L = (\partial_\mu - \frac{ig}{2} W_\mu^r \hat{\tau}_r)\psi_L, \tag{1.8}$$

where g is the coupling constant and W_μ^r are the gauge fields for $SU(2)$. Since the right-handed electron is a singlet of this $SU(2)$, its covariant derivative will be identical to its ordinary derivative,

$$\nabla_\mu \psi_R = \partial_\mu \psi_R. \tag{1.9}$$

We should also include the contribution due to the $U(1)$ group to the covariant derivatives. Therefore, we have to determine the $U(1)$ transformation of the various fields. Under the action of $U(1)$, we demand the following behavior:

$$\psi_L \to e^{i\hat{Y}\theta(x)}\psi_L, \quad \psi_R \to e^{i\hat{Y}\theta(x)}\psi_R. \tag{1.10}$$

Here $\hat{Y}$ is the generator (just a number) of the $U(1)$ group, called the *weak hypercharge*. It is related to the electric charge Q and the third component of isospin (T_3) by Gell-Mann-Nishijima formula

$$Q = (T_3 + \frac{1}{2}Y). \tag{1.11}$$

Therefore, $Y = -2$ for singlets and $Y = -1$ for doublets, *i.e.*,

$$\hat{Y}\psi_L = -\psi_L, \quad \hat{Y}\psi_R = -\psi_R. \tag{1.12}$$

To make the derivatives covariant with respect to these transformations as well, we must introduce a new gauge field B_μ and write

$$\nabla_\mu \psi_L = (\partial_\mu - \frac{ig}{2} W_\mu^r \hat{\tau}_r - \frac{ig'}{2}\hat{Y} B_\mu)\psi_L, \tag{1.13}$$

and

$$\nabla_\mu \psi_R = (\partial_\mu - \frac{ig'}{2}\hat{Y} B_\mu)\psi_R, \tag{1.14}$$

g' is the $U(1)$ coupling constant. The factor 1/2 was chosen to simplify later expressions. Now we are in a position to write down the Lagrangian for the gauge fields and the leptons. This is given by

$$\mathcal{L} = \mathcal{L}_{leptons} + \mathcal{L}_{gauge}, \tag{1.15}$$

where

$$\mathcal{L}_{leptons} = \overline{\psi}_L i\gamma^\mu \nabla_\mu \psi_L + \overline{\psi}_R i\gamma^\mu \nabla_\mu \psi_R, \tag{1.16}$$

and

$$\mathcal{L}_{gauge} = -\frac{1}{4} F^r_{\mu\nu} F^{r\mu\nu} - \frac{1}{4} f_{\mu\nu} f^{\mu\nu}. \tag{1.17}$$

The field-strength tensors are

$$F^r_{\mu\nu} = \partial_\mu W^r_\nu - \partial_\nu W^r_\mu + g\varepsilon_{rst} W^s_\mu W^t_\nu, \tag{1.18}$$

and

$$f_{\mu\nu} = \partial_\mu B_\nu - \partial_\nu B_\mu. \tag{1.19}$$

Note that the gauge symmetry does not allow a mass term for leptons or gauge bosons. A Dirac mass term would be of the form $\overline{e}_L e_R$, which would break the $SU(2)$ invariance, since e_L is a part of a doublet that transforms differently from e_R, which is s singlet. Obviously, these masslessness properties are a phenomenological disaster: electrons, muons and taus have masses. Three gauge bosons must somehow get a mass, while gauge boson, coupling to the charge Q, must be massless.

The masses are generated through the Higgs mechanism. This mechanism involves the introduction of a scalar field $H(x)$, which is a doublet of the $SU(2)$

group with a hypercharge $Y = 1$. The contribution to the electroweak Lagrangian due to the Higgs scalar field will then be:

$$\mathcal{L}_{Higgs} = (\nabla_\mu H)^\dagger (\nabla^\mu H) - V(H^\dagger H), \tag{1.20}$$

where the potential is

$$V(H^\dagger H) = M^2 H^\dagger H + \lambda (H^\dagger H)^2, \tag{1.21}$$

The coupling of the scalars to the fermions, also known as Yukawa coupling, is then

$$\mathcal{L}_{Yukawa} = -h(\overline{\psi}_L H \psi_R + \overline{\psi}_R H^\dagger \psi_L), \tag{1.22}$$

where h is a Yukawa coupling constant. This interaction term is symmetric under local $SU(2)_L \otimes U(1)_Y$ transformations, and hypercharge neutral if the Higgs field has the hypercharge $Y = 1$. Therefore, the electroweak Lagrangian of the electron family takes the form

$$\begin{aligned}
\mathcal{L} &= \mathcal{L}_{leptons} + \mathcal{L}_{gauge} + \mathcal{L}_{Higgs} + \mathcal{L}_{Yukawa} \\
&= \overline{\psi}_L i\gamma^\mu \nabla_\mu \psi_L + \overline{\psi}_R i\gamma^\mu \nabla_\mu \psi_R - \frac{1}{4} F^r_{\mu\nu} F^{r\mu\nu} - \frac{1}{4} f_{\mu\nu} f^{\mu\nu} \\
&\quad + (\nabla_\mu H)^\dagger (\nabla^\mu H) - V(H^\dagger H) \\
&\quad - h(\overline{\psi}_L H \psi_R + \overline{\psi}_R H^\dagger \psi_L).
\end{aligned} \tag{1.23}$$

For spontaneous symmetry breaking, we require $M^2 < 0$. By choosing one gauge in which the vacuum expectation value of the scalar field is given by

$$H_0 = \begin{bmatrix} 0 \\ \upsilon/\sqrt{2} \end{bmatrix}, \tag{1.24}$$

where $\upsilon^2 = -m^2/\lambda$, both $SU(2)_L$ and $U(1)_Y$ symmetries are broken. We next expand the Lagrangian about the minimum of the Higgs potential V by writing

$$H = \frac{1}{\sqrt{2}} \begin{bmatrix} 0 \\ \upsilon + \sigma(x) \end{bmatrix}, \tag{1.25}$$

where $\sigma(x)$ is real scalar field, called the *Higgs boson.* The Yukawa term in the Lagrangian has become

$$\begin{aligned} \mathcal{L}_{Yukawa} &= -h\left\{\overline{\psi}_L H \psi_R + \overline{\psi}_R H^\dagger \psi_L\right\} \\ &= -h\frac{(\upsilon+\sigma)}{\sqrt{2}}\{\overline{e}_R e_L + \overline{e}_L e_R\} \\ &= -\frac{h\upsilon}{\sqrt{2}}\overline{e}e - \frac{h\upsilon}{\sqrt{2}}\sigma\overline{e}e. \end{aligned} \tag{1.26}$$

Therefore, the electron has acquired a mass of

$$m_e = \frac{h\upsilon}{\sqrt{2}}. \tag{1.27}$$

Similarly, the Higgs part in the Lagrangian has become:

$$\begin{aligned} \mathcal{L}_{Higgs} &= (\nabla_\mu H)^\dagger(\nabla^\mu H) - V(H^\dagger H) \\ &= \frac{1}{2}(\partial^\mu\sigma)(\partial_\mu\sigma) - M^2\sigma^2 \\ &\quad + \frac{\upsilon^2}{8}\{g^2|W_\mu^1 - iW_\mu^2|^2 + (g'B_\mu - gW_\mu^3)^2\} + \dots, \end{aligned} \tag{1.28}$$

plus interaction terms. We see that the Higgs field has a mass equal to

$$m_H^2 = -2M^2. \tag{1.29}$$

This is then the physical Higgs boson. If we define the charged gauge fields

$$W_\mu^\pm = \frac{W_\mu^1 \pm iW_\mu^2}{\sqrt{2}}, \tag{1.30}$$

and define the orthogonal combinations

$$Z_\mu = -B_\mu \sin\theta_W + W_\mu^3 \cos\theta_W, \tag{1.31}$$

$$A_\mu = B_\mu \cos\theta_W + W_\mu^3 \sin\theta_W, \tag{1.32}$$

where θ_W is called the weak mixing angle and it is defined by

$$\tan\theta_W = g'/g, \tag{1.33}$$

the Higgs part can be rewritten in the form

$$\begin{aligned}\mathcal{L}_{Higgs} &= \frac{1}{2}(\partial^\mu\sigma)(\partial_\mu\sigma) - M^2\sigma^2 \\ &\quad + \frac{g^2\upsilon^2}{8}\{W^{+2} + W^{-2} + \frac{1}{\cos\theta_W} Z^2\} + \cdots ,\end{aligned} \tag{1.34}$$

Proportional to $g^2\upsilon^2$, the term is recognizable as a mass term for the charged vector bosons $W_\mu^\pm$ and the neutral gauge boson Z_μ

$$M_{W^\pm} = g\upsilon/2, \tag{1.35}$$

$$M_{Z^0} = g\upsilon/2\cos\theta_W = M_W/\cos\theta_W, \tag{1.36}$$

whereas the field A_μ remains a massless gauge boson. We have achieved the desired particle content plus a massive Higgs scalar.

But, do the interactions also correspond to those in Nature?

The interactions among the gauge bosons and leptons may be read from $L_{leptons}$. Therefore, it is convenient to write $L_{leptons}$ in terms of the charged gauge bosons $W_\mu^\pm$ and the neutral ones Z_μ^0 and A_μ. The charged gauge bosons couplings to leptons are given by

$$\begin{aligned}L_{int}^W &= \frac{g}{\sqrt{2}}\{\overline{\nu}_L\gamma^\mu e_L W_\mu^- + \overline{e}_L\gamma^\mu\nu_L W_\mu^+\} \\ &= \frac{g}{2\sqrt{2}}\{\overline{\nu}\gamma^\mu(1-\gamma_5)eW_\mu^- + \overline{e}\gamma^\mu(1-\gamma_5)\nu W_\mu^+\} \\ &= \frac{g}{2\sqrt{2}}\{j^- W_\mu^- + j^+ W_\mu^+\},\end{aligned} \tag{1.37}$$

and

$$j^- = \overline{\nu}\gamma^\mu(1-\gamma_5)e, \qquad j^+ = \overline{e}\gamma^\mu(1-\gamma_5)\nu, \tag{1.38}$$

are the charged weak currents. Equation 1.37 describes the low-energy phenomenology (Fermi current-current interactions), provided that, we identify the coupling constant as

$$\frac{g^2}{8} = \frac{G_F M_W^2}{\sqrt{2}}, \tag{1.39}$$

With the help of Equation 1.36, we obtain the tree level estimate for the *electroweak breaking scale*:

$$\upsilon = (G_F\sqrt{2})^{-1/2} \simeq 246GeV. \tag{1.40}$$

Similarly, the neutral gauge boson A_μ couplings to leptons are given by

$$\begin{aligned} \mathcal{L}^A_{int} &= -g\sin\theta_W\{\overline{e}_L\gamma^\mu e_L + \overline{e}_R\gamma^\mu e_R\}A_\mu \\ &= -g\sin\theta_W\overline{e}\gamma^\mu e A_\mu, \end{aligned} \tag{1.41}$$

Therefore, we may identify A_μ as the photon, provided that, we set

$$g\sin\theta_W = e. \tag{1.42}$$

With the help of Equation 1.39 and Equation 1.42, the gauge bosons Masses can be rewritten in the form:

$$M_W^2 = \frac{e^2 G_F}{4\sqrt{2}\sin^2\theta_W}, \tag{1.43}$$

$$M_Z^2 = M_W^2/\cos^2\theta_W. \tag{1.44}$$

If symmetry breaking in Nature occurs by other mechanisms, the relationship between the masses will not as simple, and this can be parameterized as:

$$\rho = \frac{M_W^2}{M_Z^2\cos^2\theta_W}, \tag{1.45}$$

where $\rho = 1$ in the Glashow-Weinberg-Salam Model. For the neutral gauge boson Z_μ couplings to leptons, we get

$$\begin{aligned}
\mathcal{L}_{int}^{Z} &= \frac{g}{2\cos\theta_W}\overline{\nu}_L\gamma^\mu\nu_L Z_\mu \\
&\quad + \frac{g}{2\cos\theta_W}\{(2\sin^2\theta_W - 1)\overline{e}_L\gamma^\mu e_L + 2\sin^2\theta_W\overline{e}_R\gamma^\mu e_R\}Z_\mu \\
&= \frac{e}{2\cos\theta_W\sin\theta_W}\{\overline{\nu}\gamma^\mu(1-\gamma_5)\nu + \overline{e}\gamma^\mu(C_A - C_V\gamma_5)e\}Z_\mu,
\end{aligned} \tag{1.46}$$

where

$$C_A = -\frac{1}{2}, \qquad C_V = -\frac{1}{2} + 2\sin^2\theta_W. \tag{1.47}$$

Looking at one of the leptons l, we can write its couplings to the neutral gauge boson Z_μ in the form

$$\mathcal{L}_{int}^{Z} = \frac{e}{\cos\theta_W\sin\theta_W}\{\bar{l}_L\gamma^\mu(T_3 - \sin^2\theta_W)l_L + \bar{l}_R\gamma^\mu(-\sin^2\theta_W Q)l_R\}Z_\mu. \tag{1.48}$$

Here T_3 is the eigenvalue of $\hat{T}_3$ (notice that $\hat{T}_3 l_R = 0$) and eQ is the electric charge of the lepton l. Note that, for the neutrinos, the l_R term disappears in any event since $Q = 0$. In terms of Dirac fermions, the couplings can be written as

$$\mathcal{L}_{int}^{Z} = \frac{e}{2\cos\theta_W\sin\theta_W}\bar{l}\gamma^\mu(C_V^l - C_A^l\gamma_5)lZ_\mu, \tag{1.49}$$

where

$$C_A^l = T_3, \qquad C_V^l = T_3 - 2\sin^2\theta_W Q. \tag{1.50}$$

Therefore the neutral current that couples to Z^μ is given by

$$J_\mu^{NC} = \bar{l}\gamma_\mu(C_V^l - C_A^l\gamma_5)l. \tag{1.51}$$

1.3 Weak Mixing Angle Measurements

The physics beyond the Standard Model can be established in two distinct ways:

- Directly by observing the particles associated with this new theory.
- Indirectly by observing the influence of these new states on precision measurements.

For example, the Higgs particle has not been discovered yet, but high precision measurements at $Q^2 = M_Z^2$ [1] at LEP, combined with the values of M_W and m_t measured at the Tevatron, have constrained the mass of the Higgs boson to satisfy the bound $m_H < 196$ GeV [8]. There are many other indirect constraints on the Standard Model and its possible extensions that have been obtained by experiment.

The basic renormalized parameters of the Standard Model can be categorized as: masses, couplings, and mixing angles. In fact, the current experiments have measured a number of electroweak parameters at 1% or better. These experiments also test the Standard Model at the level of its radiative corrections. The precision measurement strategy is to experimentally determine all Standard Model observables as accuracy as possible. Some of these experiments measured the weak mixing angle. For example, $\sin^2\theta_W$ was derived from the low energy neutrino-nucleon scattering experiment NuTeV, which unfortunately does not match its Standard Model prediction [9].

Now we will review some of the measurements of the weak mixing angle. However, the comparison of $\sin^2\theta_W$ between experiments demands a common definition of that parameter. We begin by writing $\sin^2\theta_W$ in terms of the bare masses of the charged gauge bosons $W^{\pm}$, the neutral gauge boson Z, and the bare coupling

[1] Also known as the Z^o resonance or the Z^o-pole

constants e and g

$$\sin^2\theta_W^o = \frac{e_o^2}{g_o^2} = 1 - (M_W^o/M_Z^o)^2 = \frac{\pi\alpha^o}{\sqrt{2}(M_Z^o)^2 G_F^o}. \tag{1.52}$$

In fact, $\sin^2\theta_W$ is frequently used in two renormalization schemes: the on-shell framework and the $\overline{MS}$ approach [10–12]

$$\begin{aligned}
\sin^2\theta_W^{on-shell} &\equiv 1 - \frac{M_W^2}{M_Z^2}, && (1.53)\\
\sin^2\theta_W(0) &\equiv \frac{e^2(0)}{g^2}, && (1.54)\\
\sin^2\theta_W(\mu)_{\overline{MS}} &\equiv \frac{e^2(\mu)_{\overline{MS}}}{g^2(\mu)_{\overline{MS}}}, && (1.55)\\
\sin^2\theta_W^{eff} & \quad \text{(defined by LEP)}, && (1.56)
\end{aligned}$$

They all differ by finite calculable radiative corrections. In principle, one can therefore translate between different definitions. The first two definitions, for example, are related through a quantity called Δr that is a collection of one-loop corrections:

$$\sin^2\theta_W^{on-shell} = \frac{\sin^2\theta_W(0)}{1-\Delta r}. \tag{1.57}$$

The zero in $\sin^2\theta_W(0)$ indicates that the electric charge is renormalized at $q^2 = 0$. Unfortunately, employing any of these two definitions induces large radiative corrections in higher orders. These involve $\alpha M_t^2/M_W^2$ corrections, which can be misleading [10].

The minimal subtraction ($\overline{MS}$) definition, where μ is the mass scale of dimensional regularization, is theoretical rather than physical. This definition is useful for renormalization group studies and induces less complicated higher order corrections. In fact, employing $\sin^2\theta_W(M_Z)_{\overline{MS}}$ generally leads to small radiative corrections in neutral currents processes.

The final definition $\sin^2\theta_W^{eff}$ was invented for LEP studies. It has a numerical proximity to $\sin^2\theta_W(M_Z)_{\overline{MS}}$ [13]

$$\sin^2\theta_W^{eff} = \sin^2\theta_W(M_Z)_{\overline{MS}} + 0.0003. \tag{1.58}$$

Having explained the various definitions of $\sin^2\theta_W$, we now examine the measurements of $\sin^2\theta_W$ performed by different collaborations. The weak mixing angle has been precisely measured, at the Z-pole, by the LEP and the SLD collaborations. The results were in an excellent agreement with the Standard Model, but additional precise measurements away from the Z-pole were needed not only to test the Standard Model but also to probe for possible new physics phenomena beyond the Standard Model. Therefore, two other experiments -NuTev and APV- measured $\sin^2\theta_W$ at low energies away from the Z-pole.

Measurements at the Z-pole

The LEP [14] experiment at CERN and the SLD [15] experiment at SLAC measured forward-backward and left-right asymmetries from electron-positron (e^-e^+) collisions near the Z-pole. The SLD collaboration studied parity violation in Z production and decay into charge lepton pairs:

$$e^-_{L,R} + e^+ \rightarrow Z^o \rightarrow l^- + l^+, \tag{1.59}$$

where l represents an electron, a muon, or a tau lepton. These processes are characterized by the Z boson-lepton coupling asymmetries A_e, A_μ, and A_τ. Any of these asymmetries is defined as

$$A_l = \frac{2\upsilon_l a_l}{\upsilon_l^2 + a_l^2}, \tag{1.60}$$

where v_l and a_l are the effective vector and axial vector couplings of the Z boson to the lepton current, respectively. The Standard Model assumes lepton universality, so that all three pecies of leptonic asymmetry parameters are expected to be identical, and directly related to the effective weak mixing angle $\sin^2\theta_W^{eff}$

$$A_l = \frac{2(1-4\sin^2\theta_W^{eff})}{1+(1-4\sin^2\theta_W^{eff})^2}. \tag{1.61}$$

They reported a value of [15]

$$\sin^2\theta_W^{eff} = 0.23098 \pm 0.00026. \tag{1.62}$$

The result is in excellent agreement with the Standard Model predictions.

On the other hand, the LEP collaboration extracted $\sin^2\theta_W$ from several measurements. They measured the forward-backward asymmetry of $e^-_{L,R}+e^+ \to Z^o \to b\overline{b}$ and $e^- + e^+ \to Z^o \to c\overline{c}$ using samples of hadronic Z^o decays in which electrons and muons were observed. They reported a value of [14]

$$\sin^2\theta_W^{eff} = 0.23205 \pm 0.00068, \tag{1.63}$$

which is in excellent agreement with the Standard Model predictions as well.

Measurements Off the Z-Pole

Two experiments have measured $\sin^2\theta_W$ at low energies away from the Z-pole. First, the neutrino-nucleon scattering (NuTeV) experiment [9] at Fermi National Accelerator Laboratory (FNAL). The NuTeV collaboration extracted $\sin^2\theta_W$ from measurement of the ratio of neutral current and charged current cross sections in neutrino-nucleon deep inelastic scattering (Figure 1.1)

$$R^\nu = \frac{\sigma_{NC}(\nu_\mu N \to \nu_\mu X)}{\sigma_{CC}(\nu_\mu N \to \mu^- X)}, \quad R^{\overline{\nu}} = \frac{\sigma_{NC}(\overline{\nu}_\mu N \to \overline{\nu}_\mu X)}{\sigma_{CC}(\overline{\nu}_\mu N \to \mu^+ X)}, \tag{1.64}$$

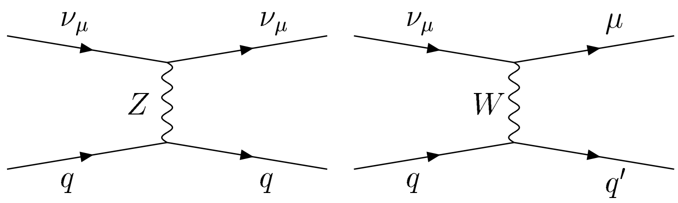

Figure 1.1: Lowest-order diagrams for $\nu_\mu q \rightarrow \nu_\mu q$ and $\nu_\mu q \rightarrow \mu^- q'$ in NuTeV experiment.

at $Q^2 \sim 30$ (GeV/c)^2. The cross sections are determined by the Lagrangian for weak neutral current $\nu - q$ scattering [9]:

$$\begin{aligned} \mathcal{L} &= -\frac{G_F}{\sqrt{2}}[\overline{\nu}\gamma^\mu(1-\gamma^5)\nu] \\ &\quad [\epsilon_L^q \overline{q}\gamma_\mu(1-\gamma^5)q + \epsilon_R^q \overline{q}\gamma_\mu(1-\gamma^5)q], \end{aligned} \tag{1.65}$$

where $\epsilon^q_{L,R}$ are the chiral quark couplings. The term $-Q\sin^2\theta_W$, where Q is the quark charge in units of e, contributes to $\epsilon^q_{L,R}$ for the weak neutral current but not for the charged one. Therefore, $\sin^2\theta_W$ can be extracted from the above ratio. The NuTev collaboration reported [9]

$$\sin^2\theta_W^{on-shell} = 0.2277 \pm 0.0013 \text{ (stat.)} \pm 0.0009 \text{ (syst.)}, \tag{1.66}$$

which is 3 standard deviations above the Standard Model prediction. The cause of this discrepancy is not known. It could be explained by theories beyond the Standard Model such as extra gauge bosons, new couplings, etc [16, 17].

Second the Atomic Parity Violation (APV) experiment [18] which measured the $6S \rightarrow 7S$ transition probability in atomic Cesium at $Q^2 \sim 10^{-4}$. They then extracted $\sin^2\theta_W$ from measurement of the weak charge of the nucleus

$$Q_W = \rho[Z(1 - 4sin^2\theta_W) - N]. \tag{1.67}$$

The Standard Model predicts $Q_W(^{133}Cs)$ to be [19]

$$Q_W(^{133}Cs)_{SM} = -73.19 \pm 0.03. \tag{1.68}$$

The APV collaboration achieved a result of [18]

$$Q_W(^{133}Cs)_{APV} = -72.69 \pm 0.48, \tag{1.69}$$

which is equivalent to

$$\sin^2\theta_W(M_Z)_{\overline{MS}} = 0.2292 \pm 0.0019. \tag{1.70}$$

The APV measurement of $\sin^2\theta_W$ is consistent with the Standard Model prediction ($+1.0\sigma$) [19]. Selected measurements of $\sin^2\theta_W^{eff}$ as a function of Q^2 are shown in Figure 1.2.

New Measurements

In the light of this situation new results from other experiments can add important information to these interesting deviations from the Standard Model predictions. Two new measurements involving polarized electron scattering: parity-violating Møller (ee) scattering at SLAC [20], which is known as E158, and elastic parity-violating Mott (ep) scattering at Thomas Jefferson National Accelerator facility (JLab) [21], which is known as QWEAK.

Both experiments have the same energy scale, $Q^2 \sim 0.03$ (GeV/c)^2, which makes the E158 and QWEAK measurements of $\sin^2\theta_W$ particularly interesting. Any agreement with the Standard Model would imply that the most likely explanation for NuTeV result is atomic and hadron structure effects.

This dissertaion reports on the most recent result measured by E158 which has determined the weak mixing angle off the Z-pole by measuring the right-left asymmetry in electron-electron (e^-e^-) scattering.

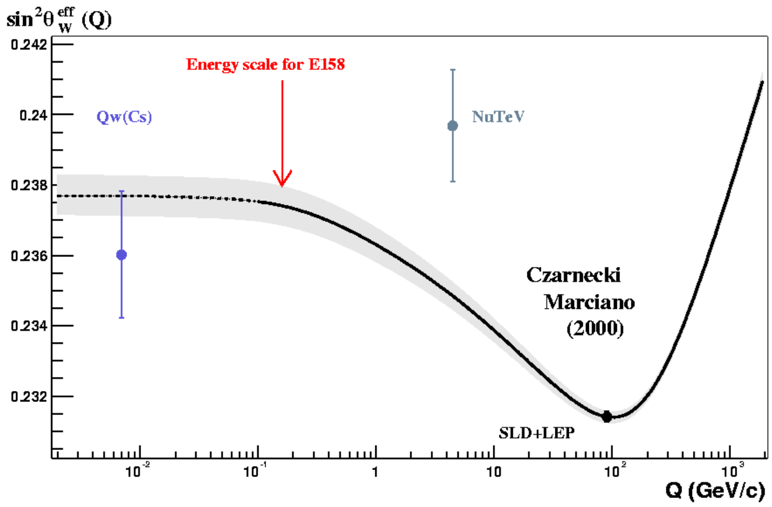

Figure 1.2: Measurements of $\sin^2\theta_W^{eff}$ as a function of the momentum transfer Q.

The QWEAK experiment has recently been proposed and approved at JLab using the continuous electron beam accelerator facility(CEBAF). QWEAK seeks to perform the most precise determination of the weak charge of the proton $Q_W(p)$ off the Z-pole, using parity-violating elastic ep scattering.

1.4 Parity-Violating Møller Scattering and $Q_W(e)$

We will now discuss the role of the neutral currents and the parity violating asymmetry in testing the Standard Model described above by measuring one of the most important parameters for this model- $\sin^2\theta_W$.

1.4.1 Why Parity-Violating Asymmetry?

Polarized electron scattering off an unpolarized target provides a clean window to study weak neutral interactions by measuring the asymmetry [22]

$$A_{PV} = \frac{d\sigma_R - d\sigma_L}{d\sigma_R + d\sigma_L}. \tag{1.71}$$

In these experiments, we separately measure the differential cross-sections, $d\sigma_R$ and $d\sigma_L$, for the scattering of left-handed and right-handed electrons on an unpolarized target, respectively. The asymmetry in Equation 1.71 is then obtained by computing the ratio of the difference to the sum of these cross-sections.

This asymmetry has the following features:

1. The asymmetry comes from the interference between the weak and electromagnetic amplitude. That is, the asymmetry is proportional to the G_F/α and hence larger than usual weak interaction effects which are $O(G_F^2)$ [10].

$$\begin{aligned} \sigma \quad & \alpha \quad \mid A_{em} + A_{weak} \mid^2, \\ A_{PV} \quad & \simeq \quad \frac{\mid A_{em} A_{weak} \mid}{\mid A_{em} \mid^2 + \mid A_{weak} \mid^2} \simeq \frac{\mid A_{weak} \mid}{\mid A_{em} \mid} \simeq \frac{G_F Q^2}{4\pi\alpha}. \end{aligned} \tag{1.72}$$

2. Most systematics errors that arise in cross-section measurement, such as the target thickness, beam energy, cancel in the ratio.

3. Finally, the relative sign between the weak and electromagnetic interactions, determined by the parity experiments, provides an additional check on various models. in fact, some models may predict the correct magnitude for the asymmetry, but the wrong sign!

Several experiments used polarized electron beams to study parity violation. These experiments are listed in Table 1.1. The first experiment, SLAC E122 performed from 1978-79 [23], studied deep inelastic scattering of polarized 18 GeV electrons from an unpolarized liquid deuterium target. E122 made the first observation of parity violation in a weak neutral scattering. It was one of the experiments that ensured the existence of the Standard Model. The next two experiments were performed at Mainz [24] and Bates [25]. They also gave results consistent with theory. Finally, SAMPLE [26] and HAPPEX [27] experiments, which search for strange form factors in the nucleon.

Experiment	**Reaction**	A_{PV}
SLAC E122 [23]	eD DIS	10^{-4}
Mainz [24]	eBe^9 QE	10^{-5}
Bates [25]	eC^{12} elastic	10^{-6}
Sample(Bates) [26]	ep elastic	10^{-5}
Happex [27]	ep elastic	10^{-5}

Table 1.1: History of parity experiments.

The size of the asymmetry, measured by these experiments, is in the range of $10^{-4} - 10^{-7}$, which is extremely small. Therefore, measuring these small asymmetries presents two unique problems:

1. Collection of a sufficient number N of events, since the statistical error, ΔA_{PV}, is proportional to $1/\sqrt{N}$. For the experiments in Table 1.1, N is in the range of $10^{10} - 10^{16}$

2. Control of systematic uncertainties.

1.4.2 Right-Left Asymmetry in Møller Scattering

We consider here the case of polarized Møller scattering $e^-e^- \to e^-e^-$. Our primary focus will be on the use of a very intense highly polarized electron beam ($P_e > 0.8$) in fixed target unpolarized electron scattering.

The right-left asymmetry for polarized electrons scattering on an unpolarized target is given by

$$\begin{aligned} A_{RL} &= \frac{d\sigma_R - d\sigma_L}{d\sigma_R + d\sigma_L} \\ &= \frac{(d\sigma_{RR} + d\sigma_{RL}) - (d\sigma_{LL} + d\sigma_{LR})}{(d\sigma_{RR} + d\sigma_{RL}) + (d\sigma_{LL} + d\sigma_{LR})}, \end{aligned} \tag{1.73}$$

where $d\sigma_{ij}$ denotes the cross section for an incoming electron of helicity i on a target of helicity j, which is given by $d\sigma_{ij} \sim \sum_{kl} |\mathcal{M}_{ij,kl}|^2$, where k and l are the helicity of the outcoming electrons. Since $d\sigma_{RL} = d\sigma_{LR}$ by rotational invariance,

$$\begin{aligned} A_{RL} &= \frac{d\sigma_{RR} - d\sigma_{LL}}{d\sigma_{RR} + d\sigma_{LL} + 2d\sigma_{RL}} \\ &= \frac{\sum_{kl}\{|\mathcal{M}_{RR,kl}|^2 - |\mathcal{M}_{LL,kl}|^2\}}{\sum_{kl}\{|\mathcal{M}_{RR,kl}|^2 + |\mathcal{M}_{LL,kl}|^2 + 2|\mathcal{M}_{RL,kl}|^2\}}. \end{aligned} \tag{1.74}$$

The tree level calculations of all helicity amplitudes, were performed several years ago [22] and were used to calculate the asymmetry.

The interaction Lagrangian is given by

$$\begin{aligned} \mathcal{L}_{int} &= g_\gamma j_\mu^{em} A^\mu + g_Z j_\mu^{NC} Z^\mu \\ &= g_\gamma[-\overline{e}\gamma_\mu e]A^\mu + g_Z[\overline{e}\gamma_\mu(C_V^e - C_A^e\gamma_5)e]Z^\mu, \end{aligned} \tag{1.75}$$

where

$$C_A^e = \frac{1}{2}, \qquad C_V^e = \frac{1}{2} - 2\sin^2\theta_W. \tag{1.76}$$

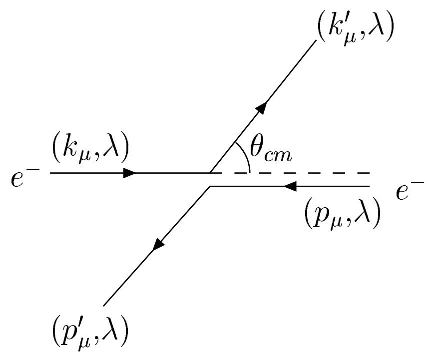

Figure 1.3: The kinematics of ee elastic scattering in the center-of-momentum frame. (k_μ, λ), etc, denote four-momenta and helicity of electrons.

and

$$g_\gamma = e, \qquad g_Z = \frac{e}{2\cos\theta_W \sin\theta_W}. \tag{1.77}$$

We consider the collision

$$e_1^-(k,\lambda) + e_2^-(p,\Lambda) \to e_3^-(k',\lambda')e_4^-(k',\Lambda'), \tag{1.78}$$

where (k, λ) denote four momenta and helicities, respectively. The Kinematics of the collision in the center-of-mass frame is shown in Figure 1.3. The four Feynman diagrams representing the tree-level amplitudes for ee scattering via γ and Z exchange are shown in Figure 1.4. The total amplitude is then given by [22]

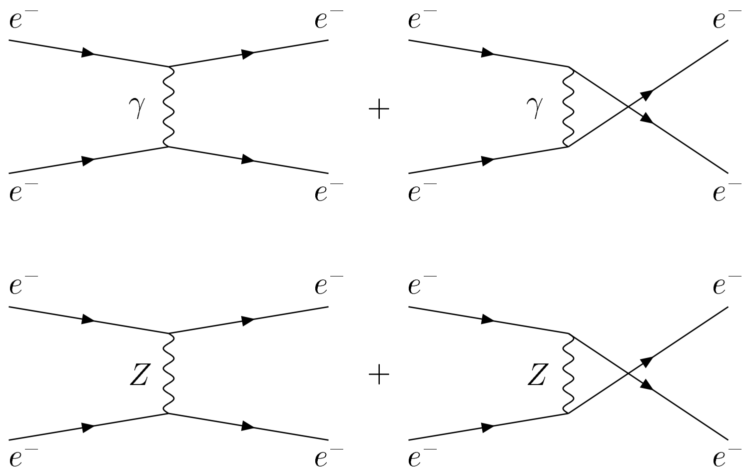

Figure 1.4: Lowest-order diagrams for $e^-e^- \to e^-e^-$, which lead to the right-left asymmetry, A_{RL}.

$$
\begin{aligned}
\mathcal{M}_{\lambda\Lambda,\lambda'\Lambda'} &= \frac{-g_\gamma^2}{ys}\overline{u}_{\lambda'}(k')\gamma_\mu u_\lambda(k).\overline{u}_{\Lambda'}(p')\gamma^\mu u_\Lambda(p) \\
&+\frac{g_\gamma^2}{(1-y)s}\overline{u}_{\Lambda}(p')\gamma_\mu u_\lambda(k).\overline{u}_{\lambda'}(k')\gamma^\mu u_\Lambda(p) \\
&+\frac{-2g_Z^2}{M_Z^2}\overline{u}_{\lambda'}(k')\gamma_\mu(C_V^e - C_A^e\gamma_5)u_\lambda(k).\overline{u}_{\Lambda'}(p')\gamma^\mu(C_V^e - C_A^e\gamma_5)u_\Lambda(p) \\
&+\frac{2g_Z^2}{M_Z^2}\overline{u}_{\Lambda}(p')\gamma_\mu(C_V^e - C_A^e\gamma_5)u_\lambda(k).\overline{u}_{\lambda'}(k')\gamma^\mu(C_V^e - C_A^e\gamma_5)u_\Lambda(p),
\end{aligned}
\tag{1.79}
$$

Here λ and Λ represent the initial electrons' helicities while λ' and Λ' represent the final electrons' helicities. The interference between these amplitudes, *i.e.* the electromagnetic and weak amplitudes, gives rise to the standard model prediction [22]

$$A_{RL}(e^-e^- \to e^-e^-) = \frac{G_F Q^2}{4\sqrt{2}\pi\alpha}\frac{1-y}{1+y^4+(1-y)^4}\,Q_W(e), \tag{1.80}$$

where

$$\begin{aligned} y &= \sin^2(\theta_{cm}/2), \\ Q^2 &= -q^2 = y(k' + k)^2 \\ &= y(2m^2 + 2mE_{beam})_{fixed\, target}, \\ q^2 &= (k' - k)^2. \end{aligned} \tag{1.81}$$

Here, Q^2 is the momentum transfer, G_F is the Fermi coupling constant, α is the fine structure constant, m is the electron mass, E is the incident beam energy, θ_{cm} is the scattering angle in the center-of-mass frame. In this expression, terms of order m/E and m/Q have been dropped since we assume $m^2 \ll Q^2 \ll m_Z^2$. At tree level, the weak charge of the electron, $Q_W(e)$, is given by

$$Q_W(e) = 4\sin^2\theta_W - 1, \tag{1.82}$$

where θ_W is the weak mixing angle. In terms of θ_{cm} [20],

$$A_{RL}(e^-e^- \to e^-e^-) = -mE\frac{G_\mu}{\sqrt{2}\pi\alpha}\frac{4\sin\theta_{cm}}{(3+\cos^2\theta_{cm})}Q_W(e). \tag{1.83}$$

For fixed target experiments, the asymmetry in Equation 1.80 is very small because of the tiny G_F factor and the $4\sin^2\theta_W - 1$ suppression factor. For $E =$ 50 GeV, $E' =$ 25 GeV (corresponding to $\theta cm = \pi/2$ where the asymmetry is maximal) and 100% beam polarization (*i.e.* $P_e = 1$), A_{RL} is -3.2×10^{-7}. Radiative corrections [28] reduce this asymmetry by more than 40%, as disscused in the following section.

If we measure the right-left asymmetry with a fractional statistical error of 10%, we can then measure the weak mixing angle with a precesion of 0.001, since the asymmetry is proportional to $(4\sin^2\theta_W - 1)$:

$$A_{RL} \propto (4\sin^2\theta_W - 1) \Rightarrow \frac{\delta\sin^2\theta_W}{\sin^2\theta_W} \simeq \frac{1-4\sin^2\theta_W}{4\sin^2\theta_W}\frac{\delta A_{RL}}{A_{RL}}. \tag{1.84}$$

Therefore, using the predicted Standard Model value of $\sin^2\theta_W$ at $Q^2 = 0.03$ $(\mathrm{GeV/c})^2$, $\sin^2\theta_W = 0.238$, one can get

$$\frac{\delta \sin^2\theta_W}{\sin^2\theta_W} \simeq 0.05\,\frac{\delta A_{RL}}{A_{RL}}. \tag{1.85}$$

Therefore, a measurement of the right-left asymmetry with a precession of $\delta A_{RL}/A_{RL} \simeq 0.1$ can result in a measurement of $\sin^2\theta_W$ with a precession of $\delta\sin^2\theta_W/\sin^2\theta_W \simeq 0.005$, *i.e.* $\delta\sin^2\theta_W \sim 0.001$.

1.4.3 One-Loop Radiative Corrections

A measurement of ΔA_{RL} to $\pm 1.4\times 10^{-8}$ is only useful if one knows the standard model prediction to that level of certainty. Such precision requires the inclusion of quantum loop effects. Indeed, because of the tree level prediction is suppressed by $4\sin^2\theta_W - 1$, one anticipates that the relative size of one-loop contributions without such a suppression factor will be quite big, and that indeed turns out to be the case.

The largest leading-order corrections to the right-left asymmetry A_{RL} at low energies come from three sources [28]:

1. γZ mixing and the W-loop diagrams.

2. WW and ZZ box diagrams.

3. Boxes containing one photon and the Z-loop diagrams.

Considering the one-loop radiative corrections to A_{RL}, Equation 1.80 is modified as [28]:

$$A_{RL} = \frac{G_\mu Q^2}{4\sqrt{2}\pi\alpha}\frac{1-y}{1+y^4+(1-y)^4}\,Q_W^{LO}(e), \tag{1.86}$$

in which the tree level suppression factor $Q_W(e) = 4\sin^2\theta_W - 1$ was replaced by the following leading-order expression:

$$Q_W^{LO}(e) = \rho\{4\sin^2\theta_W(Q^2) - 1 - \mathcal{F}_1(s,c) - \mathcal{F}_2(Q^2,y)\}, \tag{1.87}$$

$$\tag{1.88}$$

and

$$s \equiv \sin^2\theta_W(m_z)_{\overline{MS}},$$
$$c \equiv \cos^2\theta_W(m_z)_{\overline{MS}}.$$

Here ρ is a function of radiative terms and has a numerical value of almost one, $\rho \simeq 1.00122$.

The most important loop corrections come from the running $\sin^2\theta_W(Q^2)$. It comes from the γZ-mixing and the W-loop diagrams illustrated in Fig. 1.5 and is given by

$$\sin^2\theta_W(Q^2) = \kappa(Q^2)\sin^2\theta_W(m_z)_{\overline{MS}}, \tag{1.89}$$

where $\kappa(Q^2)$ is the electroweak form factor and at low Q^2 is given by:

$$\kappa(0) = 1.0301 \pm 0.0025. \tag{1.90}$$

This correction is very significant. At low Q^2, it represents a 3% shift in the effective $\sin^2\theta_W$. Since A_{RL} is proportional to $Q_W(e) = 4\sin^2\theta_W - 1$, that +3% increase in $\sin^2\theta_W$ gets amplified in A_{RL} and gives rise to a −38% reduction in A_{RL} [29].

The next source of one-loop corrections, $\mathcal{F}_1(s,c)$, comes from the WW and ZZ box diagrams shown in Figure 1.6

$$\mathcal{F}_1(s,c) = \frac{\alpha(m_z)}{4\pi s^2} - \frac{3\alpha(m_z)}{32\pi s^2 c^2}(1-4s^2)[1+(1-4s^2)^2]. \tag{1.91}$$

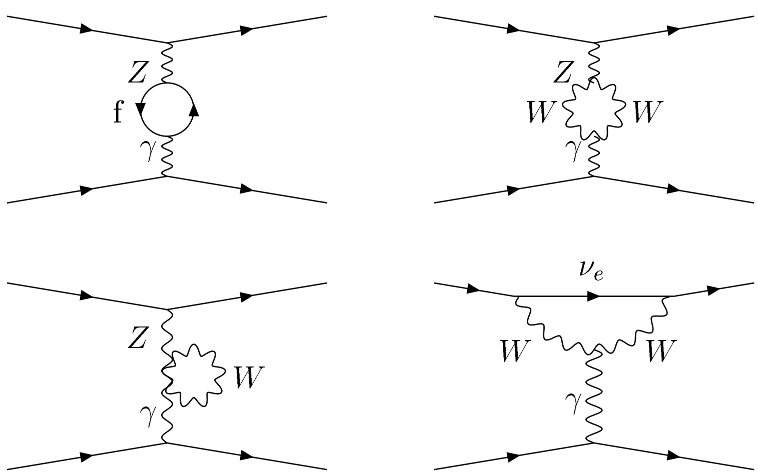

Figure 1.5: γZ mixing and W-loop diagrams

The WW box is not suppressed by $4\sin^2\theta_W - 1$ and gives rise to +4% increase in A_{RL}. On the other hand, the ZZ box diagrams are suppressed by $4\sin^2\theta_W - 1$. Therefore their contribution is tiny, 0.1%.

The last source of one-loop corrections, $\mathcal{F}_2(Q^2, y)$, comes from boxes containing one photon and Z-loop diagrams (see Figure 1.7) giving rise to Q^2 dependent corrections. For $y = 1/2$ and $Q^2 = 0.025$ GeV^2, $\mathcal{F}_2$ gives rise to a -6% reduction in A_{RL}.

Collecting all of the one-loop corrections, one finds, for $y = 1/2$ and $Q^2 = 0.025$ GeV^2,

$$Q_W^{LO}(e) = -0.046 \pm 0.002. \tag{1.92}$$

This represents a $40\% \pm 3\%$ reduction in the asymmetry because of quantum loop effects. For $y = 1/2$ and $Q^2 = 0.025$ GeV^2, one finds that the radiative corrections reduce A_{RL} from -2.97×10^{-7} to -1.80×10^{-7} [28].

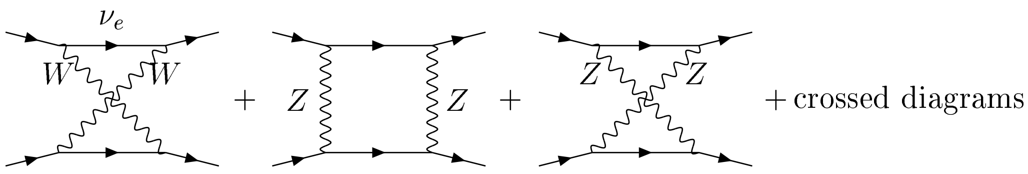

Figure 1.6: Box diagrams with two heavy bosons.

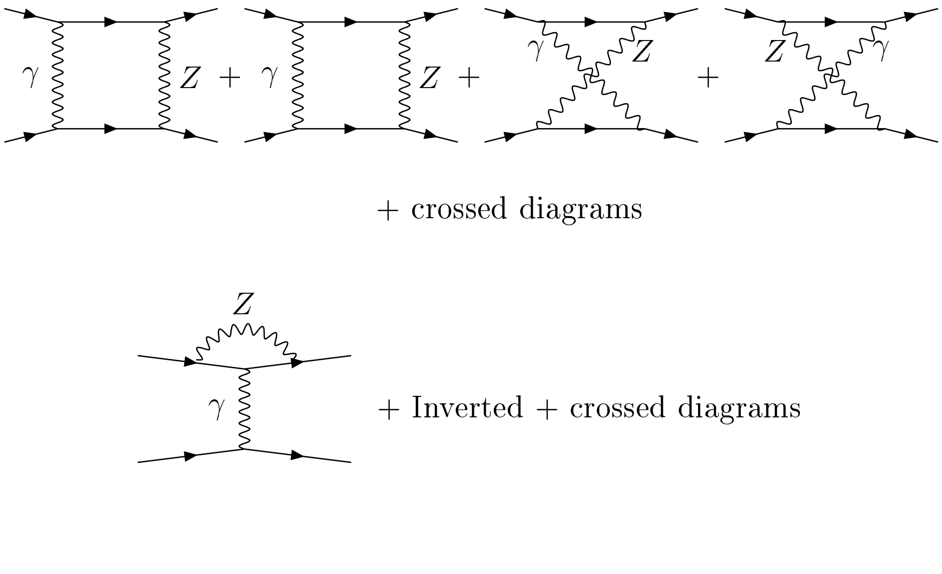

Figure 1.7: Boxes containing one photon and Z-loop diagrams.

1.5 Weak Mixing Angle and Physics Beyond the Standard Model

The Standard Model of elementary particles has been regarded only as a low-energy effective theory of the yet-more-fundamental theory. The Standard Model unfortunately cannot be valid to high energy scales up to the Plank scale ($\sim 1.2 \times 10^{19}$ GeV), where gravity is expected to become strong. Although the measurement reported in this thesis is not precise enough to be a major quantitative test of physics beyond the Standard Model, it can be sensitive to different aspects of new physics. In the following, we indicate how the proposed measurement may be sensitive to new physics. We consider four cases: 1) the effect of Z' bosons on low-energy neutral current phenomena 2) contact interactions 3) doubly-charged Higgs bosons 4) Supersymmetry. We discuss the latter in detail in the next section.

1.5.1 Extra Neutral Gauge Bosons

The Standard Model can be extended to include extra neutral gauge bosons (called Z's bosons) via the existence of one or more $U(1)$ gauge symmetries beyond the hypercharge gauge asymmetry, $U(1)_Y$. These extra gauge bosons arise quite naturally in Grand Unified theories [10, 33]. For example, the $SO(10)$ model has one such additional boson, which is denoted by Z_χ, while E_6 model has Z_χ as well as a second neutral boson,Z_ψ. The masses of these bosons are not specified, but limits, at the range of $\sim 1TeV$, have been set [22]. Neutral current experiments can set constrains on the mass of these extra Z' bosons in terms of the known Z and the weak mixing angle as well.

If we consider adding two new neutral gauge bosons, $Z_i, i = \chi, \psi$, to the Standard Model, the fermionic sector of the electroweak neutral current interaction Lagrangian is given by [22],

$$\mathcal{L}_{int} = eA^\mu J_\mu^{em} + \frac{e}{\sin\theta_W \cos\theta_W} Z^\mu J_\mu^{NC} + g' \Sigma_i Z_i^\mu J_\mu^i, \tag{1.93}$$

where g' is the coupling for the new gauge bosons. The combinations [10]

$$\begin{aligned} Z_\beta^\mu &= Z_\chi^\mu \cos\beta + Z_\psi^\mu \sin\beta, \\ Z'^\mu_\beta &= -Z_\chi^\mu \sin\beta + Z_\psi^\mu \cos\beta, \end{aligned} \tag{1.94}$$

with $-\pi/2 \leq \beta \leq \pi/2$, can be taken as mass eigenstates with m_{Z_β} and $m_{Z'_\beta}$. Given the above interactions, A_{PV} is increased by a factor [22]

$$\begin{aligned} \frac{A_{PV}^{E_6}}{A_{PV}^{SM}} = 1 \quad &+ \quad 7\frac{m_Z^2}{m_{Z_\beta}^2}(\cos^2\beta + \sqrt{\frac{5}{3}}\sin\beta\cos\beta) \\ &+ \quad 7\frac{m_Z^2}{m_{Z'_\beta}^2}(\sin^2\beta - \sqrt{\frac{5}{3}}\sin\beta\cos\beta). \end{aligned} \tag{1.95}$$

For $SO(10)$ model, $\beta = 0$, that expression simplifies to

$$\frac{A_{PV}^{SO(10)}}{A_{PV}^{SM}} = 1 + 7\frac{m_Z^2}{m_{Z_\chi}^2}. \tag{1.96}$$

Therefore, if the Z' interacts with electrons, E158 would measure a non-Standard Model contribution to the expected Møller asymmetry. Conversely, if the E158 result for $\sin^2\theta_W$ is within 2σ from the predicted Standard Model value, a lower limit of 600 to $900 GeV$ can be set on the mass of the Z' [22].

1.5.2 Contact Interactions

The SM assumes the known quarks and leptons to be pointlike. Many authors have proposed models in which quarks and leptons are composite structures: bound

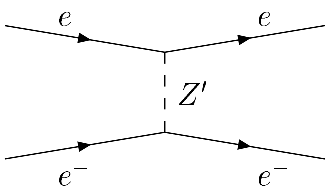

Figure 1.8: Tree-level diagram contributing to Møller scattering mediated by the extra neutral guage boson, Z'.

states of more fundamental constituents, which are often called "preons". Such composite structure could include the existence of new low-energy contact interactions (preon-binding interactions), governed by a coupling of strength 4π and a mass scale Λ [33, 34].

Considering only helicity and flavor conserving interactions, the general four-electron contact interaction Lagrangian takes the form [34]

$$\mathcal{L}_{cont} = \frac{4\pi}{2\Lambda_{ee}^2}[\eta_{LL}(\overline{\psi}_L\gamma_\mu\psi_L)^2 + \eta_{RR}(\overline{\psi}_R\gamma_\mu\psi_R)^2 + \eta_{LR}(\overline{\psi}_L\gamma_\mu\psi_L)(\overline{\psi}_R\gamma_\mu\psi_R)], \quad (1.97)$$

where Λ_{ee} is the composite mass scale for electron contact interactions. The quantities η_{LL}, η_{RR}, and η_{LR} can take values of $\pm 1, 0$ depending on the model under consideration. In analogy to Equation 1.52, one may write [33]

$$\sin^2\theta_W^{cont} - \sin^2\theta_W^{SM} = \pm\frac{\pi}{G_F\sqrt{2}}\,\frac{\eta_{LL}+\eta_{RR}+\eta_{LR}}{\Lambda_{ee}^2}. \quad (1.98)$$

E158 is sensitive to LL-RR interactions of the form $(\overline{\psi}_L\gamma_\mu\psi_L)^2 - (\overline{\psi}_R\gamma_\mu\psi_R)^2$. Therefore we can define positive and negative deviations from the Standard Model by choosing $\eta_{LL} = \eta_{RR} = \pm 1$ and $\eta_{LR} = 0$. *i.e.*

$$\sin^2\theta_W^{meas} - \sin^2\theta_W^{SM} = \pm\frac{\pi}{G_F\sqrt{2}}\,\frac{\eta_{LL}+\eta_{RR}}{\Lambda_{ee}^{\pm 2}}. \quad (1.99)$$

In this case, E158 will be capable of setting a 2σ limit on Λ_{ee} at 10 TeV.

1.5.3 Doubly-Charged Higgs Bosons

Doubly-charged Higgs bosons are a natural feature of right-left-symmetric models, which provide an attractive extension of the Standard Model. These theories contain two W bosons W_L and W_R and two neutral guage bosons Z_1 and Z_2. The W_L and Z_1 are those already discovered. In the fermion sector, RL models contain the usual quarks and charged leptons as well as three light-neutrinos (couple to the Standard Model type W_L) and three heavy-neutrinos (couple mainly to W_R). Regarding the Higgs sector of RL models, the Higgs fields of the minimal models are one bidoublet ϕ, one left-handed triplet Δ_L, and one right-handed triplet Δ_R. These fields can be represented by the 2×2 matrices [36]:

$$\phi \equiv \begin{bmatrix} \phi_1^o & \phi_1^+ \\ \phi_2^- & \phi_2^o \end{bmatrix}, \tag{1.100}$$

$$\Delta_L \equiv \begin{bmatrix} \Delta_L^+/\sqrt{2} & \Delta_L^{++} \\ \Delta_L^o & +\Delta_L^+/\sqrt{2} \end{bmatrix}, \tag{1.101}$$

$$\Delta_R \equiv \begin{bmatrix} \Delta_R^+/\sqrt{2} & \Delta_R^{++} \\ \Delta_R^o & +\Delta_R^+/\sqrt{2} \end{bmatrix}. \tag{1.102}$$

doubly-charged Higgs bosons couple charged-lepron pairs, other Higgs bosons, and guage bosons. They contribute to Møller scattering at tree level as shown in Figure 1.9. The process is described by the Lagrangian [37]

$$\mathcal{L}_{Moller} = \frac{g_{ee\Delta}^2}{2M_\Delta^2}\,\overline{\psi}_R\gamma_\mu\psi_R\,\overline{\psi}_R\gamma^\mu\psi_R + H.C., \tag{1.103}$$

where $g_{ee\Delta}^2$ is the $ee\Delta$ coupling. This equation is similar to the one used by Eichten, Lane, and Peskin (Equation 1.97) to describe the contact interactions, which leads to [37]

$$\frac{g_{ee\Delta}^2}{2M_\Delta^2} = \frac{4\pi}{\Lambda_{ee}^2}. \tag{1.104}$$

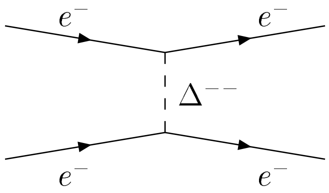

Figure 1.9: Tree-level diagram contributing to Møller scattering mediated by doubly-charged Higgs boson, Δ^{--}.

Therefore, limits on the composite mass scale Λ_{ee} for $\eta_{RR} = 1$ can be easily converted into limits on the ratio $g^2_{ee\Delta}/2M^2_{\Delta}$.

For the parity violating Møller asymmetry measured by E158, $\Lambda_{ee} = 10$ TeV corresponds to $g^2_{ee\Delta}/2M^2_{\Delta} \sim 10^{-7}$ GeV^{-2}. This is an improvement of an order of magnitude compared to limits of $g^2_{ee\Delta}/2M^2_{\Delta} \leq 10^{-6}$ GeV^{-2} set by $(g-2)_\mu$ and muonium-antimuonium experiments [2] [20].

[2]The transformation of muonium ($\mu^+e^- \equiv M$) into antimuonium ($\mu^-e^+ \equiv \overline{M}$) is a process in which the lepton flavor L_f is changed by 2 units (*i.e.* $\Delta L_f = 2$). Feinberg and Weinberg described this process by the Hamiltonian [38]:

$$\mathcal{L}_{Moller} = \frac{G_{M\overline{M}}}{\sqrt{2}} \, \overline{\psi}_\mu \gamma_\mu (1+\gamma^5)\psi_e \, \overline{\psi}_\mu \gamma^\mu (1+\gamma^5)\psi_e + H.C., \tag{1.105}$$

where $G_{M\overline{M}}$ is a four-fermion coupling constant. The first search for this process was carried out by a group at the Los Alamos Meson Facility in the late 1960s.

1.6 Parity-Violating Møller Scattering as a Probe of Supersymmetry

In this section we will show that the E158 precise measurement of the weak mixing angle of the SM can be used as a probe of Supersymmetry (SUSY). SUSY is considered to be the most promising candidate for a unified theory. It is just a generalization of the Standard Model, but it requires the existence of additional "superparticles", that are necessary to complete the symmetry. In other words, the scenario of the proton and antimatter may be repeated: at least doubling the degrees of freedom with an explicitly broken new symmetry. Antimatter does exist, so may "supermatter". Despite the absence of experimental evidences, there are several theoretical arguments, that support SUSY.

i- It turns out that the gauge coupling constants become equal at $\mu \simeq 2 \times 10^{16}$ GeV given the Minimal Supersymmetric Standard Model (MSSM) particle content [39]. On the other hand, the three gauge coupling constants miss each other quite badly with the Non-Supersymmetric Standard Model particle content (Figure 1.10). This observation obviously suggests the possibility of supersymmetric grand unification.

ii- The local version of supersymmetry leads to a partial unification of the Standard Model and Gravity, the so-called "Supergravity" [39].

iii- Why is the typical energy scale associated with the electroweak symmetry breaking–roughly, the typical size of all masses of elementary particles–so much smaller than the Planck energy? From a technical standponit, the question should be, "Why is the Higgs boson so much

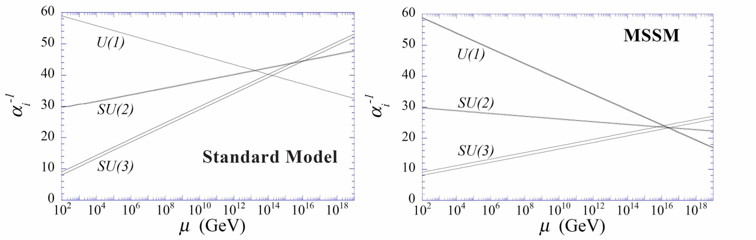

Figure 1.10: Running of the gauge coupling constants in the Standard Model and in the MSSM.

> lighter than the Planck mass?" This question is known as "hierarchy problem." The most popular theory–but not the only proposed theory-to solve the hierarchy problem (i.e. to answer the question) is Supersymmetry.

We will give a small preview of one of the most realistic SUSY theories, the Minimal Supersymmetric Standard Model (MSSM), then we will discuss the weak mixing angle within this model.

1.6.1 Supersymmetric Extension of the Standard Model

The construction of the Minimal Supersymmetric Standard Model (MSSM) has been described in many review articles and texts [39–42]. The MSSM is essentially a straightforward supersymmetric version of the Standard Model with the minimal particle content. It is the most widely studied realistic SUSY.

Superfields

Superfields were first introduced by Salam and Strathdee. All particles in supersymmetric Yang-Mills theories fall into such superfields, which have both bosons and fermions. There are two types of superfields: chiral and vector superfields.

Chiral superfields Φ has only two physical degree of freedom, which can then describe the left- or right-handed component of an SM fermion. The same superfields will also contain bosonic partenetrs, the *sfermions.* The chiral superfields are functions of $x, \theta, \overline{\theta}$, with θ,$\overline{\theta}$ being anti-commuting two-component Weyl spinors $\{\theta, \theta\} = \{\theta, \overline{\theta}\} = \{\overline{\theta}, \overline{\theta}\} = 0$. They take the form [41]

$$\Phi_L(x, \theta) = \phi(x) + \theta^\alpha \psi_\alpha(x) + \theta^\alpha \theta^\beta \epsilon_{\alpha\beta} F(x), \tag{1.106}$$

where ϕ is a complex scalar field, ψ is a Weyl fermion, and F is a non-dynamical auxiliary complex scalar field. Lagrangians for chiral superfields consist of two parts, the Kähler potential and the superpotential. The Kähler potential is nothing but the kinetic terms for the fields. The superpotential is defined by a holomorphic function, $W(\Phi)$, of the chiral superfields in order to eliminate the non-dynamical auxiliary field F.

Vector superfields $V(x, \theta, \overline{\theta})$ are supersymmetric generalization of the gauge fields. In the MSSM, the spin-0 bosons and the spin-1/2 fermions of the SM are described by the ciral superfields, while the spin-1 gauge bosons of the SM are described by the vector superfields. In the W-Z gauge [3], the superfield may take the general form [41]

$$V(x, \theta, \overline{\theta}) = -\theta \sigma_\mu \overline{\theta} A^\mu(x) + i\theta\theta\overline{\theta}\overline{\lambda}(x) - i\overline{\theta}\overline{\theta}\theta\lambda(x) + \frac{1}{2}\theta\theta\overline{\theta}\overline{\theta} D(x), \tag{1.107}$$

where A^μ a vector (gauge) field, λ a Weyl fermion (gaugino), and D is a non-dynamical auxiliary real scalar field. Lagrangians for vector superfields are the kinetic terms for these fields.

[3]The Wess-Zumino (W-Z) gauge is a representation for the superfields, in which several auxiliary fields are equal zero.

Particle Content

Particles in the MSSM come in three generations in a similar way to the SM. Each generation is described by five left-chiral superfields [42]:

fermion	sfermion
$L^I = \begin{bmatrix} \nu_e^I \\ e_L^I \end{bmatrix}$	$\tilde{L}^I = \begin{bmatrix} \tilde{\nu}_e^I \\ \tilde{e}_L^I \end{bmatrix}$
$E^I = (e_L^I)^c$	$\tilde{E}^I = (\tilde{e}_L^I)^c$
$Q^I = \begin{bmatrix} u_L^I \\ d_L^I \end{bmatrix}$	$\tilde{Q}^I = \begin{bmatrix} \tilde{u}_L^I \\ \tilde{d}_L^I \end{bmatrix}$
$U^I = (u_L^I)^c$	$\tilde{U}^I = (\tilde{u}_L^I)^c$
$D^I = (d_L^I)^c$	$\tilde{D}^I = (\tilde{d}_L^I)^c$

where $I = 1, 2, 3$ refers to the three generations. For the quarks and leptons, we normally have left-handed and right-handed fields in the SM. In order to promote them to chiral superfields, all right-handed fields were charge-conjugated so that they become left-handed Weyl spinors.

The gauge sector is described by vector superfields [42]:

gauge	gaugino	
W_μ^r	$\tilde{W}_\mu^r$	weak isospin gauge fields, $r = 1, 2, 3$.
B_μ	$\tilde{B}_\mu$	weak hypercharge gauge fields.
G_μ^a	$\tilde{G}_\mu^a$	QCD gauge fields, $a = 1, \cdots, 8$.

For the Higgs sector, a Higgs chiral superfield has to be introduced in order to break $SU(2) \times U(1)_Y$. The SM Higgs can be easily embedded into a chiral supermultiplet H. However, we need two of them since the superpotential can be constructed as a holomorphic function of chiral superfields and not of thier complex conjugates. Therefore, we need to introduce another chiral supermultiplet. In all, we have two chiral supermultiplets for the Higgs sector: H_u has hypercharge $Y = -1/2$, while H_d has hypercharge $Y = +1/2$ [42]:

$$\begin{array}{ll} \underline{\text{Higgs}} & \underline{\text{Higgsino}} \\ H_u = \begin{bmatrix} H_u^+ \\ H_u^0 \end{bmatrix} & \tilde{H}_u = \begin{bmatrix} \tilde{H}_u^+ \\ \tilde{H}_u^0 \end{bmatrix} \\ & \\ H_d = \begin{bmatrix} H_d^0 \\ H_d^- \end{bmatrix} & \tilde{H}_d = \begin{bmatrix} \tilde{H}_d^0 \\ \tilde{H}_d^- \end{bmatrix} \end{array}$$

Superpotential

In order to define the theory, we have to write down the superpotential and introduce *soft breaking terms* (without them it is impossible to break spontaneously the gauge symmetry, and also, we know that SUSY is broken in our world). "Soft" here means that the cancellation of quadratic divergencies is maintained. The most general form of a superpotential which preserves the gauge invariance of the Standard Model is [39]

$$\begin{aligned} W &= (\lambda_U)_{IJ} H_u Q^I U^J + (\lambda_D)_{IJ} H_d Q^I D^J + (\lambda_E)_{IJ} H_d L^I E^J + \mu H_u H_d \\ & \quad (\lambda_U')_{IJK} U^I D^J D^K + (\lambda_D')_{IJK} Q^I D^J L^K + (\lambda_E')_{IJK} L^I E^J L^K + \mu_I' L^I H_u. \end{aligned} \tag{1.108}$$

The first three terms correspond to the Yukawa terms in the SM. The subscripts I, J, K are generations indices. The matrices λ_D and λ_U give masses and mixing between quarks as described by the CKM. The matrix λ_E is diagonal in order to leave neutrinos exactly massless. The parameter μ gives mass to both fermions and bosons of the chiral supermultiplets H_u and H_d.

Regarding the soft breaking terms, such terms can be divided into two classes: mass terms for the sfermions, gauginos and Higgsinos, and Yukawa-type coupling terms (trilinear terms):

$$\begin{aligned}
\mathcal{L}_{soft} &= \mathcal{L}_1 + \mathcal{L}_2, && (1.109)\\
-\mathcal{L}_1 &= m^2_{\tilde{L}}|\tilde{L}|^2 + m^2_{\tilde{E}}|\tilde{E}|^2 + m^2_{\tilde{Q}}|\tilde{Q}|^2 + m^2_{\tilde{U}}|\tilde{U}|^2 + m^2_{\tilde{D}}|\tilde{D}|^2 \\
&\quad + \frac{1}{2}M_1\tilde{B}\tilde{B} + \frac{1}{2}M_2\tilde{W}\tilde{W} + \frac{1}{2}M_3\tilde{G}\tilde{G} \\
&\quad + m^2_{\tilde{H}_u}|\tilde{H}_u|^2 + m^2_{\tilde{H}_d}|\tilde{H}_d|^2, && (1.110)\\
-\mathcal{L}_2 &= (\lambda_E)_{IJ}H_d\tilde{L}^I\tilde{E}^J + (\lambda_U)_{IJ}H_u\tilde{Q}^I\tilde{U}^J + (\lambda_D)_{IJ}H_d\tilde{Q}^I\tilde{D}^J \\
&\quad + B\mu H_u H_d + c.c. && (1.111)
\end{aligned}$$

Note that the mass-squared parameters for squarks and sleptons are all hermitian 3×3 matrices while the coupling B is a complex number.

R-parity

Because of the Baryon-Lepton (B-L) invariance, the MSSM superpotential possesses a discrete symmetry called the R-parity and defined by [41]:

$$R_p = (-1)^{2s+3B+L}, \quad (1.112)$$

where s is the spin of the particle. Under R_p, all Standard Model particles, namely quarks, leptons, gauge bosons, and Higgs bosons, carry even parity while their superpartners odd due to the $(-1)^{2s}$ factor. This fact has two consequences. First, the Lightest Supersymmetric Particle (LSP) is stable. Second, superparticles can be produced or annihilate only in pairs. Therefore, the typical signature of supersymmetry at collider experiments is the missing energy, since superparticles can be produced only in pairs, and they decay eventually into the LSP, which escapes detection [41].

Higgs Sector

So far, we defined the field content and all initial parameters of the MSSM. To obtain the physical spectrum of particles present in the theory, one should carry out the standard procedure of the gauge symmetry breaking via vacuum expectation values of the neutral Higgs fields [39]

$$\langle H_u \rangle = \begin{bmatrix} 0 \\ \upsilon_u \end{bmatrix}, \quad \langle H_d \rangle = \begin{bmatrix} \upsilon_d \\ 0 \end{bmatrix}. \tag{1.113}$$

Using these equations, the masses for all fermions, sfermions, gauge bosons, gauginos, Higgs, and Higgsinos can be worked out.

Each of the two Higgs doublets has four real scalar fields, *i.e.*, we should expect eight physical particles. However, three of these scalar fields are eaten by W^+, W^-, Z^0 bosons when the symmetry is broken. Therefore, we are left with five physical scalar fields: two CP-even scalars h^0, H^0, a CP-odd scalar A^0, and two charged scalar H^+ and H^-. Their masses are given by [39]

$$m_{A^0}^2 = 2\mu^2 + m_{H_u}^2 + m_{H_d}^2, \tag{1.114}$$

$$m_{H^\pm}^2 = m_W^2 + m_{A^0}^2, \tag{1.115}$$

$$m_{h_0}^2, m_{H_0}^2 = \frac{1}{2}(m_{A^0}^2 + m_Z^2 \pm \sqrt{m_{(A^0}^2 + m_{Z)}^2)^2 - 4m_{A^0}^2 m_Z^2 \cos^2 2\beta}). \tag{1.116}$$

Here, $\tan\beta = \upsilon_u/\upsilon_d$.

The mass spectrum for the gauginos and Higgsinos are more complicated because once $SU(2)_L \times U(1)_Y$ is broken they mix among themselves. As a result, all neutral "inos", namely two neutral Higgsinos $\tilde{H}_u^0$, $\tilde{H}_d^0$, the neutral wino $\tilde{W}^3$, and the neutral bino $\tilde{B}$, mix with each other to form four Majorana fermions called *neutralinos*: $\tilde{\chi}_i^0$ for $i = 1, 2, 3, 4$

$$\left[\ \tilde{B} \quad \tilde{W}^3 \quad \tilde{H}_d^0 \quad \tilde{H}_u^0\ \right] \begin{bmatrix} M_1 & 0 & -m_Z s_W c_\beta & m_Z s_W s_\beta \\ 0 & M_2 & m_Z c_W c_\beta & -m_Z c_W s_\beta \\ -m_Z s_W c_\beta & m_Z c_W c_\beta & 0 & -\mu \\ m_Z s_W s_\beta & -m_Z c_W s_\beta & -\mu & 0 \end{bmatrix} \begin{bmatrix} \tilde{B} \\ \tilde{W}^3 \\ \tilde{H}_d^0 \\ \tilde{H}_u^0 \end{bmatrix}$$

Here, $s_W = \sin\theta_W$, $c_W = \cos\theta_W$, $s_\beta = \sin\beta$,$c_\beta = \cos\beta$. Similarly, the charged Higgsinos $\tilde{H}_u^+$, $\tilde{H}_d^-$ and the charged winos $\tilde{W}^+$, $\tilde{W}^-$ mix with each other and form two massive Dirac fermions *charginos*: $\tilde{\chi}_i^\pm$ for $i = 1, 2$

$$\left[\ \tilde{W}^- \quad \tilde{H}_u^-\ \right] \begin{bmatrix} M_2 & \sqrt{2} m_W s_\beta \\ \sqrt{2} m_W c_\beta & \mu \end{bmatrix} \begin{bmatrix} \tilde{W}^+ \\ \tilde{H}_u^+ \end{bmatrix}$$

The masses and mixing angles of the charginos and neutralinos are therefore completely determined by the values of the four parameters M_1, M_2, μ, and $\tan\beta$.

1.6.2 Weak Charge and Supersymmetry

Conservation of R-parity in the MSSM implies that every vertex must have an even number of superparticles. Consequently, for a process like the Møller scattering, $ee \to ee$, all superparticles must live in loops [43] such as those shown in Fig 1.11. Including these loop corrections, the weak charge of a fermion f is modified to [44]

$$Q_W(f) \quad = \quad 2T_3^f - 4\kappa Q_f \sin^2\theta_W + \lambda. \tag{1.117}$$

Here, $\kappa = 1 + \delta\kappa$ and λ denoting the SM radiative corrections as well as SUSY loop corrections:

$$\delta\kappa = \delta\kappa_{SM} + \delta\kappa_{SUSY}, \quad \lambda = \lambda_{SM} + \lambda_{SUSY}, \tag{1.118}$$

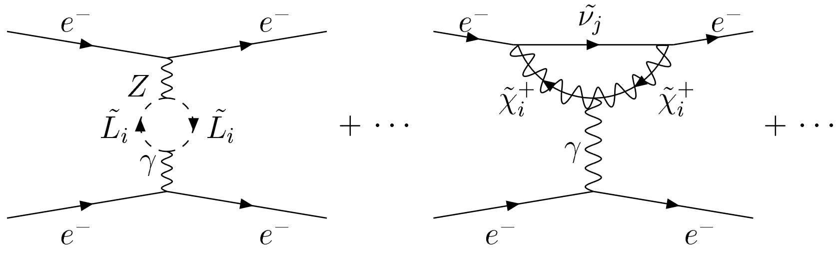

(a) (b)

Figure 1.11: SUSY loop corrections to $Q_W(e)$. Shown are corrections from sleptons contributing to γZ mixing diagram (a) and a chargino-loop diagram (b).

and

$$\begin{aligned}
\delta\kappa_{SUSY} &= \alpha(\frac{c^2}{c^2 - s^2})T + \alpha[\frac{1}{4s^2(c^2 - s^2)}]S \\
&+ \frac{c}{s}[\frac{\Pi_{\gamma Z}(Q^2)}{Q^2} - \frac{\Pi_{\gamma Z}(M_Z^2)}{M_Z^2}] \\
&+ (\frac{c^2}{c^2 - s^2})[\frac{\Delta\alpha}{\alpha} - \frac{\Pi_{\gamma\gamma}(M_Z^2)}{M_Z^2}]. \qquad (1.119)
\end{aligned}$$

The oblique parameters, T and S, and the two gauge boson self-energies, $\Pi_{\gamma Z}$ and $\Pi_{\gamma\gamma}$, come from the γZ mixing diagrams, which are the main SUSY contributions to $\delta\kappa$.

Calculated running of the weak mixing angle in the SM and the MSSM is shown in Figure 1.12. From this figure, it is apparent that another measurement of the weak mixing angle at the TeV energy scale would be useful to probe the SUSY and this is what the LHC will explore.

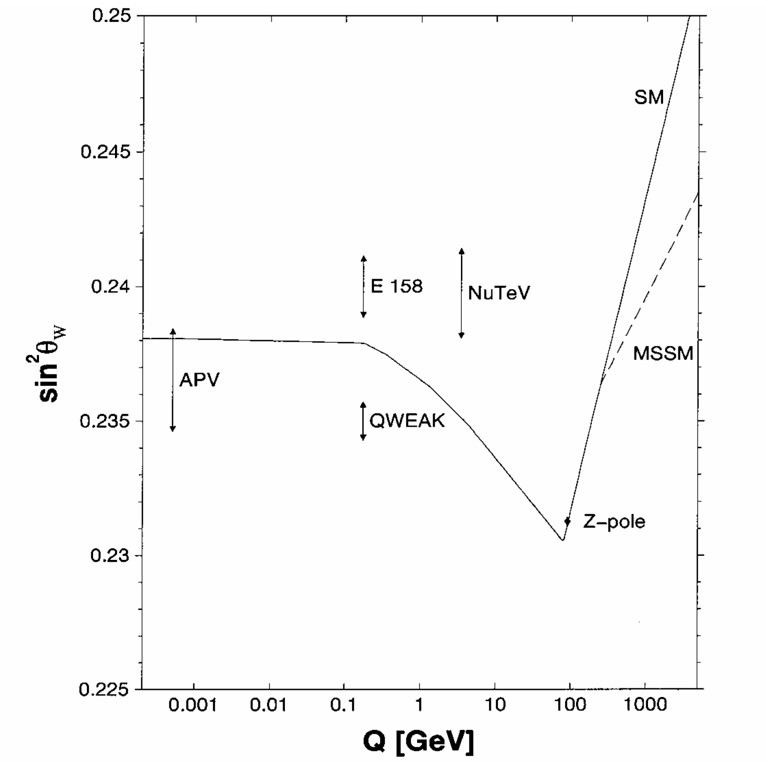

Figure 1.12: Running of the weak mixing angle in the SM, defined in the $\overline{MS}$ renormalization scheme. The dashed line indicates the reduced slope for the minimal supersymmetric standard model. E158 and QWAEK measurements have arbitrarily chosen vertical locations [44].

The possible SUSY shifts in $Q_W(e)$ and $Q_W(p)$ have opposite sign while in other new physics scenarios $\delta Q_W(e)/Q_W(e)$ or $\delta Q_W(p)/Q_W(p)$ can have either sign. This implies that a deviation of $\sim 2\sigma$ or more could help to distinguish between the MSSM and other new physics scenarios. On the other hand, agreement between the results of E158 and QWEAK and the SM prediction can not produce any significant constraints on the MSSM. Now the question is: will the E158 and QWEAK experiments observe correlated deviations?

Chapter 2

Experimental Overview and Background Processes

In the previous chapter, we discussed the motivation and the need for another measurement for the weak mixing angle. We also discussed how the weak mixing angle and the right-left asymmetry, A_{RL}, in Møller scattering are related to each other. E158 collaboration carried out this measurement using the 48-GeV polarized electron beam in End Station-A (ESA) at the Stanford Linear Accelerator Center (SLAC). This chapter provides an overview of the experiment, while Chapter 3 describes those components of the experiment that are most relevant to the topic of this dissertation. In Chapters 4, 5, and 6, we will describe several aspects of the analysis of the experiment. Conclusions and a brief discussion about the future experiments will be provided in Chapter 8.

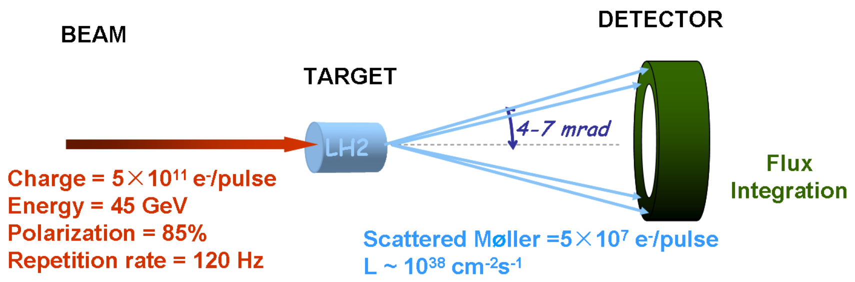

Figure 2.1: A schematic of the experimental setup in E158.

2.1 Overview of the Experiment

The main components of the experiment setup consist of the following:

1. Polarized electron Beam: to create a beam of electrons whose net longitudinal polarization is as large as possible with rapid reversal.

2. Accelerator: to achieve the required kinematics.

3. Target: to create a specific desired interaction, *i.e.*, Møller scattering.

4. Spectrometer: to select out the desired scattered electrons in the desired kinematic range.

5. Detectors: to detect and quantify the scattered flux.

A schematic of the E158 experiment is shown in Figure 2.1.

As a source of polarized electrons, we used the SLAC intense and highly polarized electron beam. This beam met the requirements of our measurement in terms of high intensity, hight polarization, and rapid reversal. In fact, the polarized electron source at SLAC can produce 5×10^{11} electrons per pulse at a repetition rate of 120 Hz. These electrons were accelerated in the LINAC and precisely monitored along their path. Inside ESA at SLAC the electrons hit a liquid hydrogen target. The flux coming out from the target has different types of scatters; including Møller, ep, primary beam, etc. The Moller scatters had to be focused on the detector face and separated as much as possible from all other types of scatters. Therefore, we used a spectrometer composed of several magnets and collimators. Møller scatters were then detected by a copper/quartz fiber calorimeter.

In the next section, we will focus on the background processes for which the spectrometer was accurately designed. A schematic of the experiment is shown in Figure 2.1.

2.2 Background Processes

There are number of background processes to Møller scattering in E158 listed below that can be grouped into four categories: electrons, pions, photons, neutrons.

2.2.1 Electrons

The *ep* scattering process was expected to occur in E158, where the incident electron scatters off a nuclear proton in the liquid hydrogen target. The spectrometer was designed to separate Møller and *ep* scatters. However, there was still significant amount of the *ep* flux hitting the Møller detector.

The dynamics of this process is not simple as the Møller scattering, but rather it is complicated, since the proton is a bound state composed of three quarks, antiquark pairs, and gluons. This state is bound by the strong interactions that are described by the theory of Quantum Chromodynamics.

In fact, the are three types of *ep* scattering:

1. Elastic *ep* scattering

This process happens at low Q^2: $Q^2 < 0.01$ GeV^2. Here the proton behaves as a point like, *i.e.*, this process is described by the theory of QED instead of QCD. In addition, the parity-violating asymmetry in elastic *ep* scattering has approximately the value of the corresponding Møller asymmetry.

2. Inelastic *ep* scattering

   This process happens when the incident electron radiates before scattering off the proton. In this case, the proton falls apart and all kinds of hadrons may come out: pions, kaons, etc. The parity-violating asymmetry in this process is not well known theoretically but it is much larger than the asymmetry in either Møller or elastic *ep* scattering. Therefore, it is the most important contribution to the experimental Møller asymmetry.

3. Deep Inelastic *ep* scattering

   This process happens at high Q^2: $Q^2 > 1$ GeV^2. In this case, the incident electron penetrates the proton and interact with one of the quarks. Electrons from deep inelastic scattering (DIS) are produced at large angles with respect to the spectrometer acceptance. Hence they do not contribute to the background in E158.

At $Q^2 = 0.03$ GeV^2, which is the energy scale of E158, the *ep* scattering is a superposition of both elastic and inelastic. An accurate estimate of the elastic and inelastic *ep* distribution in the Møller detector is then required. A correction to the experimental (Møller) asymmetry, due to this background, was estimated from data that was collected by the *ep* detector (see Section 3.4.1), as well as Monte Carlo simulations.

2.2.2 Pions

Pions are generated in E158 through three processes–real and virtual photoproduction and deep inelastic *ep* scattering. High-energy pions, unlike electrons, can punch through the collimators. Pions produced in the deep inelastic scattering process are the most important pion background. A correction to the experimental asymmetry due to the π flux was determined from data that was collected by the pion detector (see Section 3.4.2).

2.2.3 Photons

There are three primary sources of background photons:

1. Synchrotron Radiation

   One source of the background photons is the synchrotron radiation (SR). A transverse polarization in a transverse field results in the emission of a synchrotron radiation. The synchrotron radiation in E158 is generated at two different places along the experiment.

   First, a synchrotron light is emitted in the large bend in A-Line before the spectrometer. This synchrotron light results in beam asymmetries, and its effect is measured by the synchrotron light monitor (SLM).

   Second, a synchrotron light is emitted in the spectrometer dipoles in particularly in dipole D3. This synchrotron light may contribute to the asymmetry measured by Møller detector. In fact, the SR from this dipole can have an asymmetry of $A_{SR} = 100$ ppm for a 100% vertical polarization [45]. This asymmetry is suppressed by the small amount of residual vertical polarization and the small SR background in the Møller detector [1].

2. High-Energy Photons

   There was a significant amount of high-energy photons generated at the target once the beam passed through. However, this light was suppressed by the photon collimator (see Section 3.3.2). Unfortunately, this collimator itself became a source of high-energy photons from showers occurring at its inner edge. The same thing took place with the momentum collimator, leading us to the conclusion that this light could have contributed to the experimental asymmetry.

3. Low-Energy Photons

   A small flux of low-energy electrons scattered off the aluminum beam pipe and gave rise to secondary (low-energy) photons that were able to hit the detector.

2.2.4 Neutrons

A small flux of neutrons and other neutral hadrons were generated in the calorimeter from the scattered electron flux. These hadrons penetrated the shielding and gave rise to a significant response in the PMTs. Corrections to the experimental asymmetry due to the neutral backgrounds (photons and neutrons) were made using data that was taken under special experimental configurations.

[1] The spectrometer was designed to suppress this synchrotron flux as much as possible using some collimators. However, its effect must be measured.

Chapter 3

Experiment Technique

3.1 Polarized Electron Beam

The polarization can be a powerful tool for suppressing backgrounds as well as for carrying out precision electroweak measurements as we shall see. The power of polarization has already been demonstrated at the Stanford Linear Collider (SLC) where $\sin^2\theta_W$ has been very precisely determined using e^- polarization ($P_{e^-} \simeq 77\%$) at the Z pole [46]. The left-right asymmetry for $e^+e^- \to hadrons$

$$A_{LR} = \frac{\sigma(e^+e^-_L \to hadrons) - \sigma(e^+e^-_R \to hadrons)}{\sigma(e^+e^-_L \to hadrons) + \sigma(e^+e^-_R \to hadrons)} \tag{3.1}$$

has been measured to about $\pm 2\%$ and used to obtain $\sin^2\theta_W(m_Z)_{MS}$ to about $\pm 0.0004\%$. At the Z pole, A_{LR} is predicted (at the tree level) to be

$$A_{LR} = \frac{2(1-4\sin^2\theta_W)}{1+(1-4\sin^2\theta_W)^2}, \tag{3.2}$$

i.e.,

$$\frac{\Delta\sin^2\theta_W}{\sin^2\theta_W} \simeq \frac{1}{10}\,\frac{\Delta A_{LR}}{A_{LR}}. \tag{3.3}$$

At the SLC, the dominant systematic error is a $\pm 0.5\%$ polarization uncertainty which contributes a $\pm 0.0001\%$ uncertainty in $\sin^2\theta_W$. Because the e^- polarization is not 100%, the experiment actually measures

$$A_{LR}^{measured} = \frac{N_L - N_R}{N_L + N_R} = A_{LR} P_{e^-} \tag{3.4}$$

where N_i, $i = L, R$, are the number of events for each polarization setting. Therefore, the $\pm 0.5\%$ uncertainty in P_{e^-} leads to about a $\pm 0.0001\%$ systematic error in $\sin^2\theta_W$.

3.1.1 Source

Polarized electrons can be produced by various techniques. The requirements of an ideal source are: high intensity, hight polarization, and rapid reversal of helicity. Given these considerations, photoemission from a Gallium Arsenide (GaAs) photocathode is the best choice. The source consisted of four main parts: laser bench, diagnostics bench, helicity-control bench, and cathode diagnostic bench. A schematic diagram of the SLAC-E158 Polarized Electron Source is shown in Figure 3.1.

At the laser bench, the laser beam was generated using a flashlamp-pumped Ti:Sapphire laser. The laser bench also included pulse-shaping optics. At the diagnostics bench, the laser beam was divided into three branches. Two of them were used to monitor the characteristics of the laser beam while the third and main branch was traveling through to the helicity-control bench.

A circularly polarized light was produced at the helicity-control bench. The circular polarization of the laser, which in turn determines the polarization of electrons, was controlled by two linear polarizers and two Pockels cells known as the CP and PS cells. A Pockels cell is a birefringent crystal whose birefringence

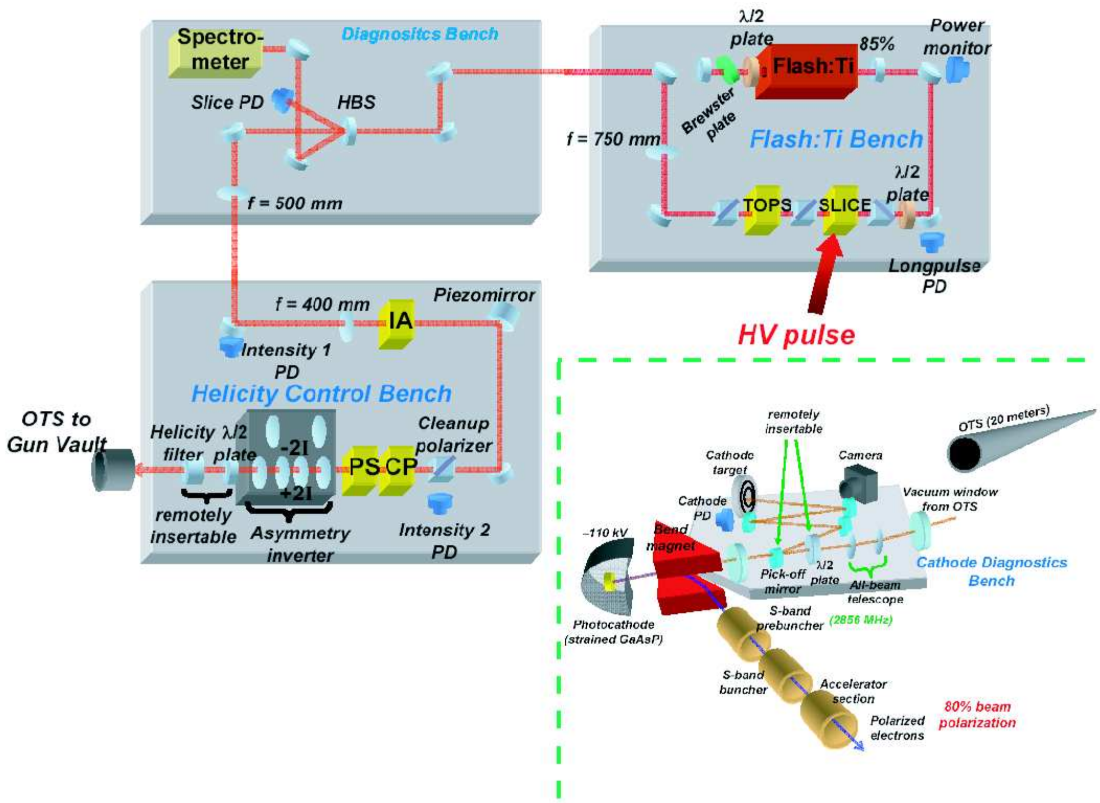

Figure 3.1: Polarized electron source overview

is controlled by an applied high voltage. The axes of the linear polarizers and the PS Pockels cell are along the x and y axes, while the axes of the CP Pockels cell are along u and v (the u and v axes are rotated by 45° with respect to x and y). This configuration can generate arbitrary elliptical polarization. The electric field vector following the PS cell can be expressed by [47]

$$|E\rangle = \begin{bmatrix} E_x \\ E_y \end{bmatrix} = \begin{bmatrix} \sin(\frac{\delta_{CP}}{2}) \\ e^{i(\frac{\pi}{2}+\delta_{PS})}\cos(\frac{\delta_{CP}}{2}) \end{bmatrix}, \tag{3.5}$$

where δ_{CP} and δ_{PS} are the polarization phase shifts imparted by the CP and PS Pockels cells. The laser circular polarization following the PS cell is given by

$$P_\gamma = \sin\delta_{CP}\cos\delta_{PS}. \tag{3.6}$$

Nominally, $\delta_{CP} = \pm\pi/2$ and $\delta_{PS} = 0$ gives perfect $\pm$circular polarization. A positive phase shift on the CP Pockels cell produces one helicity, while a negative HV pulse produces the opposite helicity. The sign of the phase shift is set by a pseudo-random number generator that updates at $120Hz$ (the electron beam pulse rate) [48]. The purpose of the helicity-control bench was not only to generate highly polarized laser beam, but also to reduce beam helicity-correlated asymmetries through asymmetry reversal devices as will be discussed later.

The laser beam was then transmitted via a 20-m long optical transport system (OTS) to the cathode diagnostic bench where a photoemission from a GaAs photocathode took place. The photoemission is a three step process:

1. An electron is exited from the valence band to the conduction band by light from the laser beam.

2. The electron diffuses to the photocathode surface.

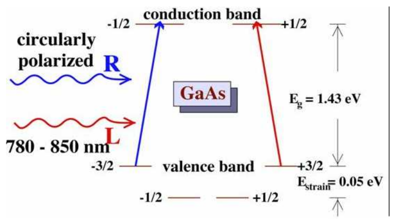

Figure 3.2: A schematic diagram shows the photoemission process from a Gallium Arsenide (GaAs) photocathode to create polarized electrons.

3. The electron escapes to the vacuum. It is then accelerated and injected to the main accelerator.

As shown in Figure 3.2, the right-helicity light excites electrons from the $P_{-3/2}, m_J = -3/2$ to the $S_{1/2}, m_J = -1/2$ level and the left-helicity light will excite electrons from the $P_{3/2}, m_J = +3/2$ to the $S_{1/2}, m_J = +1/2$ level. The cathode was operated so that the emitted electrons move in the opposite direction of the incoming light, so that a right- and left-helicity laser light yielded left- and right-helicity electrons, respectively, as defined in Figure 3.3. After exiting the cathode, the emitted polarized electron beam was bent by 38° as it entered the accelerator.

3.1.2 Accelerator

The polarized electron beam, coming out from the cathode, is accelerated through the SLAC's two-mile accelerator, LINAC, which can achieve a maximum beam energy of 51 GeV. The LINAC consists of 30 sectors; each one has a group of 8 klystrons.

At the end of the LINAC, the polarized electron beam passes through the A-Line, where the beam must bend 24.5° in order to enter End Station A (ESA).

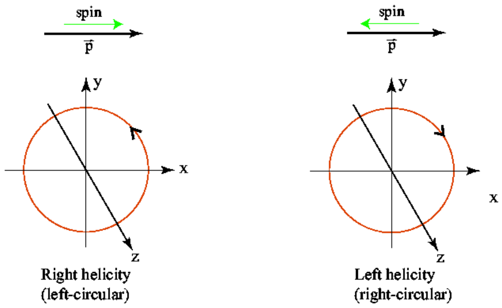

Figure 3.3: Definition of right- and left-helicity for the electron beam (top) and the laser beam (bottom).

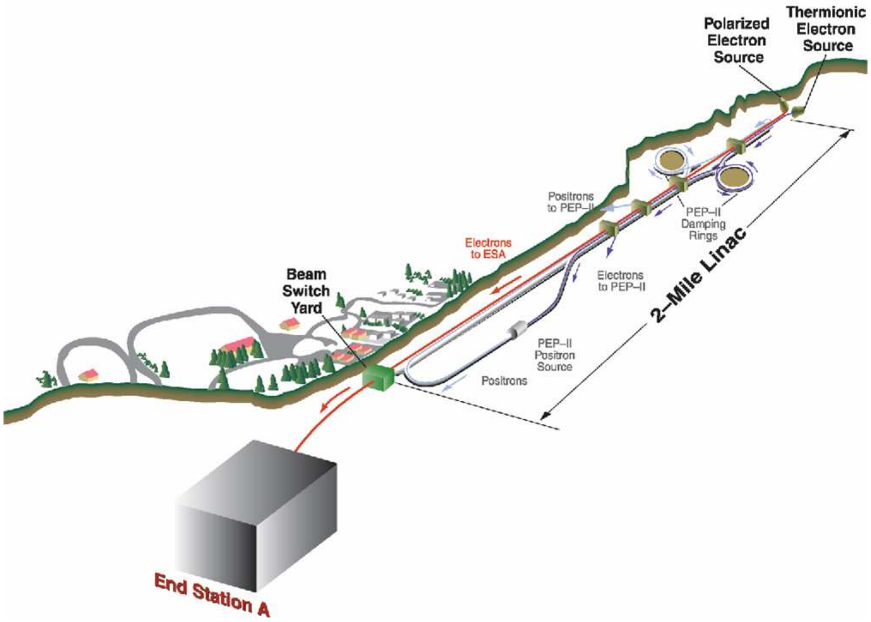

Figure 3.4: Overview of SLAC accelerator, A-Line, and End Station A

Twelve dipole and twelve quadrupole magnets are used together to bend the beam in the A-Line area. This is where the $g-2$ precession happens and the sign of the physics asymmetry is reversed if the beam energy is raised from 45.0 GeV up to 48.3 GeV. The target, spectrometer and detectors were placed inside the ESA,.

3.1.3 Feedback System

In parity violation experiments, we measure a certain quantity, *e.g.* the asymmetry, under certain experimental conditions. We then reverse the experimental conditions and measure the same quantity again. To measure the asymmetry, we only reverse the helicity of the electron beam. Other than the helicity, all experimental conditions should be the same at a level below the statistical precision of the asymmetry measurement.

Ideally, changing the voltage on the Pockels cell changes no laser beam characteristics except for the helicity. In practice, the intensity and the position of the beam on the cathode are correlated with the helicity.

Because of the differences in the laser intensity and position at the cathode, helicity-correlated differences in the beam parameters originate. They then propagate through the accelerator and result in helicity correlations with the intensity, position, angle, and energy at the target, which in turn can lead to false asymmetries known as *"beam asymmetries"*. These false asymmetries have the same size of the statistical precision that we seek to achieve in the experiment.

E158 used different methods to control the beam asymmetries.

1. The electron beam helicity was chosen pseudo-randomly at 120 Hz.

2. A great deal of suppression in helicity-correlated differences can be achieved at the electron source with the help of a feedback loop that controls the

helicity reversal in the optics leading to the photocathode, and with the help of physics asymmetry reversals as well as false beam asymmetry reversals (as discussed in the previous chapter).

3. A cross-check was also provided by the luminosity monitor that is supposed to measure null asymmetry.

4. E158 required very precise monitoring of all beam parameters in order to trace any helicity-correlated differences in beam parameters and make the appropriate corrections to the experimental asymmetry.

Helicity Sequence

The helicity of the electron beam was governed by an electronic system called PMON. Each electron pulse was first divided into four quadruplets. Two pair of pulses were then created using these four quadruplets. This was done by choosing the helicities of the first and second quadruplets randomly (using PMON). The helicities of the other quadruplets, however, had to be complements of the first and second helicities. For example, if the helicities of the first and second quadruplets were chosen to be LR, the helicities of the other quadruplets had to RL. The first pair is called *timeslot0* and the second pair is called *timeslot1*. In principle, the asymmetries observed by the two timeslots should not be different. Therefore, it can be used as a method to supress helicity-correlated asymmetries.

Feedback Loop

Feebback is essential for suppressing any charge asymmetry at the electron source. If the source system induces a charge asymmetry A^{ind}, the overall beam asymmetry

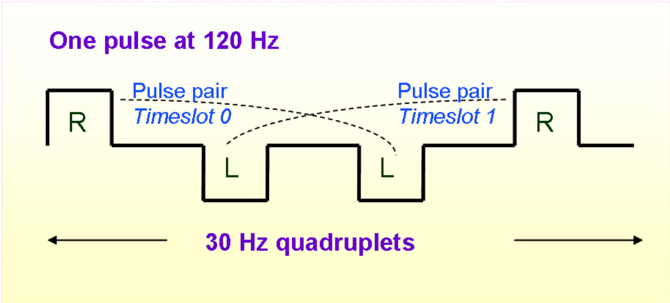

Figure 3.5: A schematic shows the helicity sequence technique.

is then given by [49],

$$A_k^{beam} = A_k^{ind} + A_k^{stat}, \tag{3.7}$$

where k is the number of the current feedback loop and A_k^{stat} is due to stat fluctuations. The induced charge asymmetry A_k^{ind} is given by the following formula,

$$\begin{aligned} A_1^{ind} &= 0, \\ A_k^{ind} &= A_{k-1}^{ind} - A_{k-1}^{beam}, \end{aligned} \tag{3.8}$$

which leads to

$$A_k^{beam} = A_k^{stat} + A_{k-1}^{stat}. \tag{3.9}$$

The results of this feedback algorithm on the beam asymmetry is shown in Table 3.1.

The average beam asymmetry over N feedback cycles is then,

$$\begin{aligned} A_{ave}^{beam} &= \frac{1}{N}\sum_{k=1}^{N} A_k^{beam} \\ &= \frac{1}{N}\sum_{k=1}^{N} [A_k^{stat} - A_{k-1}^{stat}] \\ &= \frac{A_N^{stat}}{N}. \end{aligned} \tag{3.10}$$

Feedback Cycle	A_k^{beam}
1	A_1^{stat}
2	$A_2^{stat} - A_1^{stat}$
3	$A_3^{stat} - A_2^{stat}$
k	$A_k^{stat} - A_{k-1}^{stat}$

Table 3.1: The feedback algorithm on the beam asymmetry.

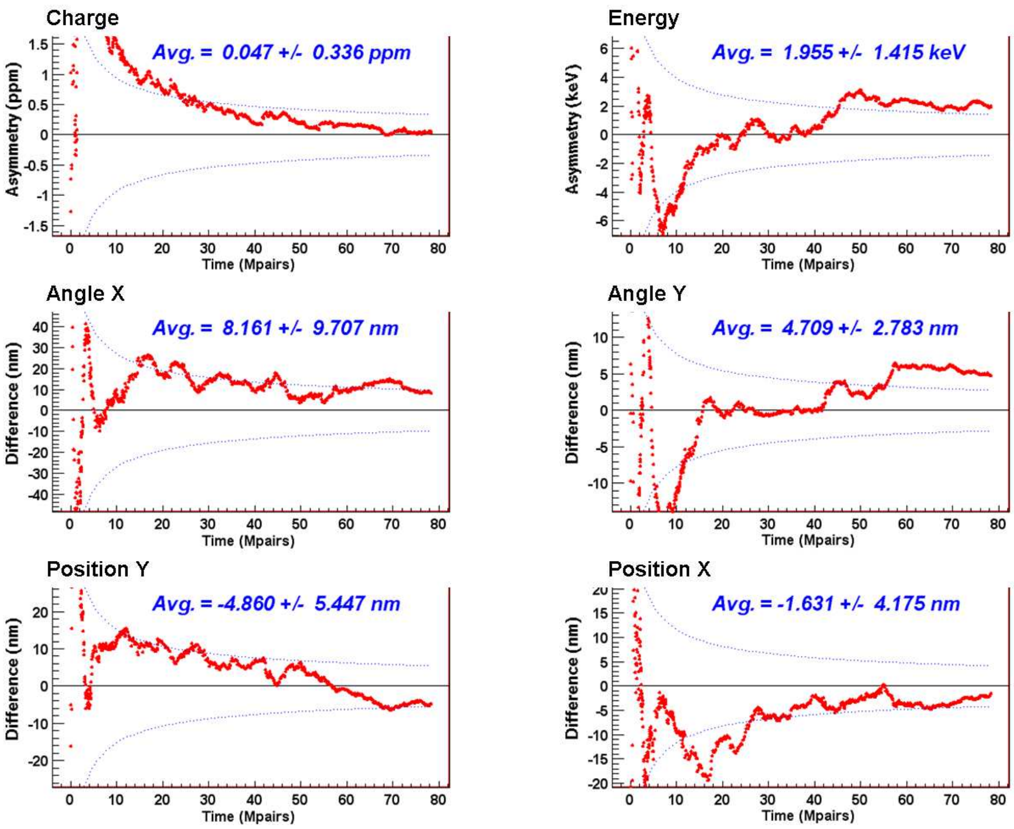

Figure 3.6: Shown is the average beam asymmetry, which approaches zero with the help of the feedback loop.

By following this basic prescription, the average beam asymmetry approaches zero [50] as shown in Figure 3.6.

3.1.4 Asymmetry Reversals

A powerful way to cancel the systematic effects is to reverse the sign of the physics asymmetry by a method that leaves the sign of the systematic effects unchanged. This is done in two different methods: first by rotating a half-wave plate in the laser transport line and second by changing the beam energy. Another way to cancel the systematic effects is to reverse the sign of the false beam asymmetry and keep the physics asymmetry unchanged. This is done by the "asymmetry inverter" device.

Half Wave Plate

Immediately before the cathode, there is an insertable half wave plate that reverse the polarization of the laser beam independently from the Pockels cell.

$g-2$ Precession

An additional method for flipping the sign of the physics asymmetry is the $g-2$ spin precession in the A-Line, which reverses the polarization of the electron beam by 180° provided that the beam energy is raised from 45.0 GeV up to 48.3 GeV. Consequently, E158 runs at both energies (the highest energies available at SLAC) at which the electron polarization is longitudinal.

Asymmetry Inverter

It is a system of four lenses sitting immediately before the half wave plate. They reverse the beam position and intensity and leave the sign of the physics asymmetry unchanged. In other words, they do the opposite job that the half wave plate does. Ideally, adding two equal sets of data with opposite-sign beam asymmetries should then cancel beam asymmetries.

3.1.5 Beam Monitoring

It was very important to verify that the helicity reversal did not change the physical characteristics of the beam. The differential cross-section depends to a certain extent on the energy, position, and angle of the beam. If there are systematic differences in any of these parameters, which correlated to the helicity of the beam, there will be contributions to the measured asymmetry. These contributions could definitely affect our interpretation of the final result. Therefore, E158 required very precise monitoring of all beam parameters, in order to trace any helicity-correlated systematic differences in these parameters.

Four kinds of devices have been used to monitor the beam parameters: toroids for charge, beam position monitors (BPMs) for position, angle, and energy, a wire array for beam spot size, and a polarimeter detector for polarization. A schematic of these monitoring devices is shown in Fig. 3.7. The polarimeter detector is out of scope since it was placed inside ESA between the profile detector and the Møller detector.

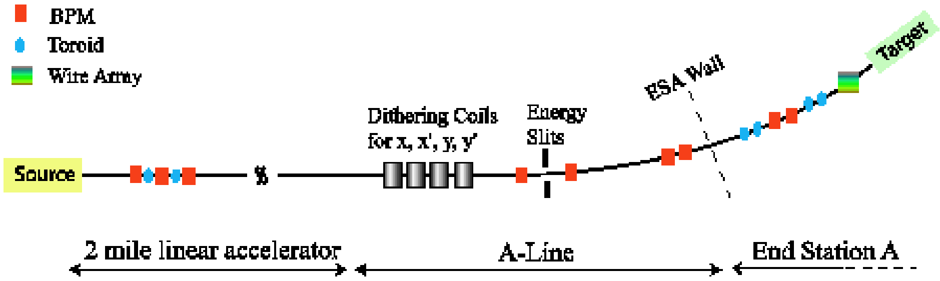

Figure 3.7: Beam monitoring devices

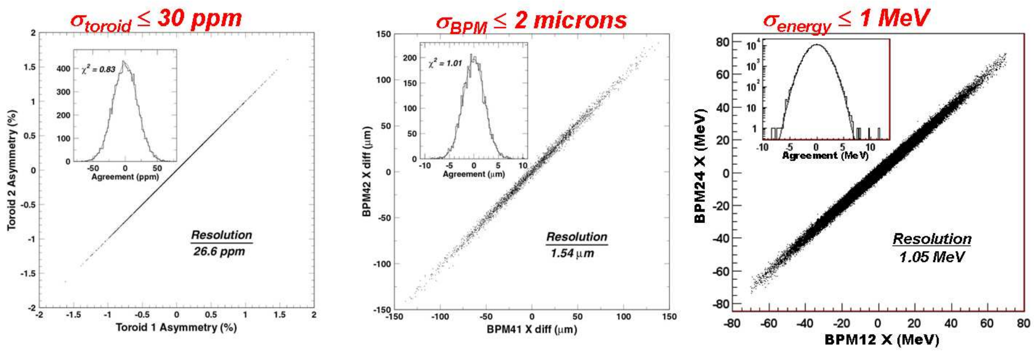

Figure 3.8: BPMs resolutions

Wire Array

The wire array was used to measure the beam size, also known as the *spotsize*, and to provide a two-dimensional profile for the beam intensity, when it is inserted in the beam path. It is a movable unit consisting of two planes of very thin wires, one running horizontally and the other vertically, and an aluminum foil sitting next to the two planes. The Aluminum foil was set at some particular high voltage, so that pulses can be induced through the wires when the beam hits these individual wires. The aluminum foil has a one inch hole through which the beam can pass.

Polarimeter

The polarimeter is a movable Cherenkov colarimeter used to measure the longitudinal polarization of the electron beam by measuring the right-left asymmetry when the electron beam scatters off a longitudinally polarized iron foil target.

The polarimeter detector was placed between the profile detector and the Møller detector. It consistes of six quartz plates sandwiched between seven tungsten plates. The Cherenkov light, which was produced at these plates, is transfered through a light guide made of an aluminum tube. The Cherenkov light is then reflected by a mirror to be collected by a PMT.

During the polarization measurement, which happened every other day, the liquid hydrogen target was removed and the foil target was moved into the electron beam. The *holy* collimator (see Section 3.3.4) was also inserted during the measurement in order to minimize the background scatters.

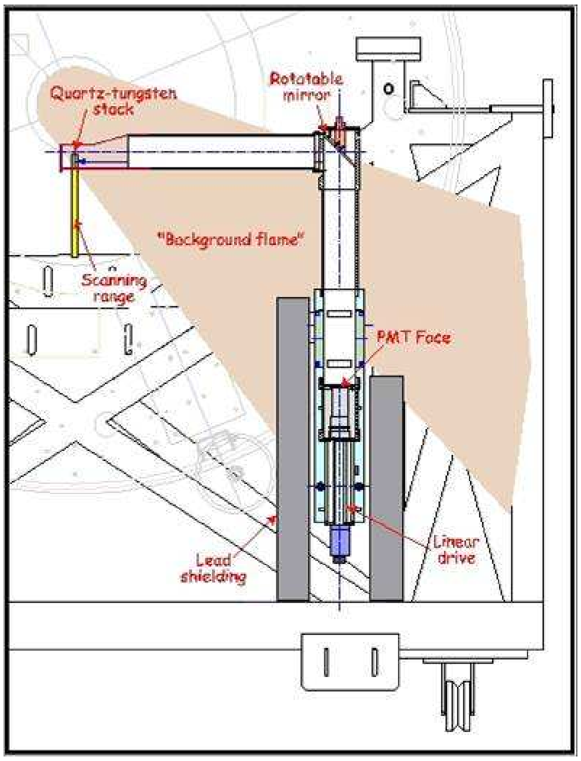

Figure 3.9: A schematic diagram of the polarimeter detector.

3.1.6 Electron Beam Characteristics

The polarized electron source produced 5×10^{11} electrons per pulse with 88% beam polarization at a repetition rate of 120 Hz. The experiment was carried out at two beam energyies, 48.3 GeV and 45.0 GeV in order to cancel systematic effects. A description of these effects will be disscussed later. The electron beam characteristics are summarized in Table 3.2.

Polarization	88%
Energy	45GeV
Intensity	5×10^{11} e^-/pulse
Pulse Length	275 ns
Repetition Rate	120 Hz
Beam Spot Size	$\sim$1 mm

Table 3.2: Beam characteristics.

3.2 Target

3.2.1 Liquid Hydrogen Target

The most practical source of target electrons is hydrogen since the relevant background are elastic and inelastic *ep* scattering and photonproduction of pions off protons at very low Q^2, which are well understood and can be suppressed. Moreover, it provides the least amount of radiation loss for a given target thickness. The number of incident electrons on the target was at the range of $2 - 5 \times 10^7$ electrons per pulse. More than 10^7 scattered electrons must be detected every beam pulse in order to achieve a statistical error close to 10^8 on A_{RL}.

E158's target was made of a aluminum pipe of 1.5 m-long, filled with liquid hydrogen [51]. One side of the pipe was connected to a heat exchanger that was designed to remove heat from the target and keep the target at a temperature of about 17.9 k. This heat exchanger was simply a copper coil through which helium (at 4 k) flows. The other side of pipe was connected to a pump in order to moves the hydrogen through the system at a flow rate of 10 m/s. A schematic of the target loop is shown in Figure 3.10

Inside the pipe, a series of wire-mesh partial-disks spaced along the hydrogen pipe. The purpose of the wire mesh was to introduce turbulence of about the beam spotsize (1-2 mm) as well as transverse flow in the target region. This technique allows the unheated liquid hydrogen to mix into the beam volume thoroughly. Therefore, the liquid hydrogen density fluctuations due to beam heating, which contributes to the physical asymmetry,can be minimized.

The hydrogen target was housed inside a vacuum aluminum chamber (2m $\times$ 2m) that was attached to the electron beam line. Inside this chamber, there was a table holding several solid carbon targets that were used for spectrometer and detector studies. The target loop can be moved vertically (up to 15 cm out of the beam) while the solid target table can be moved horizontally by remote control. Therefore, one of the targets, either the liquid hydrogen target or one of the carbon targets, can be in the beam path.

Liquid hydrogen density fluctuatuions due to beam heating are known as "*target boiling*". The effect of target boiling on the width of the physical asymmetry is given by [52]:

$$\sigma[A_{RL}] = \sqrt{\frac{1}{N} + (\frac{\sigma[l]}{l})^2}, \tag{3.11}$$

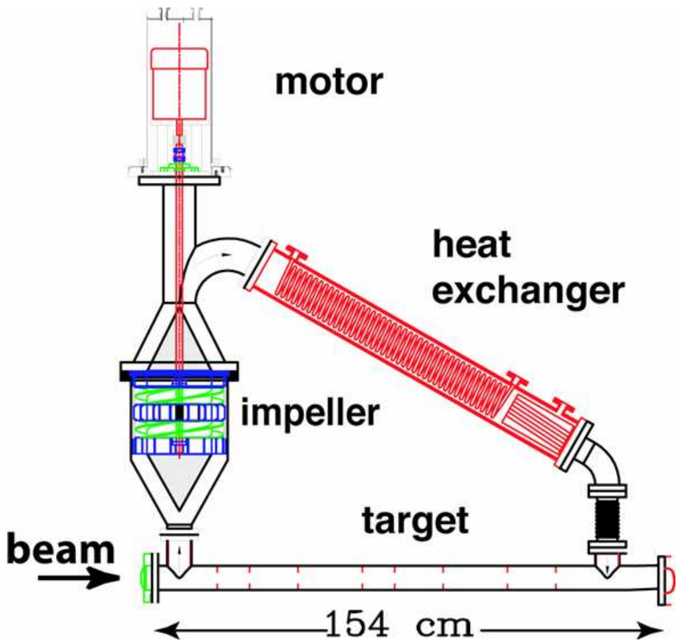

Figure 3.10: A schematic of the target loop.

where N is the number of events integrated, l is the effictive target length and $\sigma[l]$ is the RMS fluctuation in l. Therefore, we require $\frac{\sigma[l]}{l} \ll \frac{1}{N}$. There are two ways to determine this effect. The first is to measure the width of the asymmetry $\sigma[A_{LR}]$ as a function of the intensity I. If there is no boiling and $\frac{\sigma[l]}{l}$ is negligible,

$$\sigma[A_{RL}] \propto \sqrt{I^{-1}}. \tag{3.12}$$

The second test requires that there be two independent detectors measuring the asymmetries A^1_{RL} and A^2_{RL} simultaneously then a correlation between the asymmetries can be measured

$$C = \frac{< A^1_{RL} A^2_{RL} >}{\sigma[A^1_{RL}]\sigma[A^2_{RL}]} = \frac{(\sigma[l]/l)^2}{1/N + (\sigma[l]/l)^2}. \tag{3.13}$$

If C is small, boiling is negligible. For E158, the *Luminosity Monitor* played the role of the second detector as we will see later.

3.2.2 Longitudinally Polarized Iron Foil Target

The electron beam polarization was measured by measuring the right-left asymmetry when the electron beam scatters off a longitudinally polarized iron foil target. A set of three iron foils of different thicknesses (20, 50 and 100 μm), located in front of the schattering chamber, was used for this purpose. Each foil can be moved into and out of the beam. The polarization of the foils is provided by a Helmholtz coil magnet.

3.3 Spectrometer

E158's used several magnets and collimators to separate the scattered particles of interest from backgrounds and to define the kinematic acceptance. The spectrometer was designed to meet the following requirements:

1. Kinematics: The f.o.m.[1] varies slowly with θ_{cm} and is relatively flat in the range $-0.5 < \cos\theta_{cm} < 0$ (see Figure 3.11). On the other hand, the asymmetry is maximal at $E' = 25$ GeV and fall to zero at $E' = 0$ GeV and $E' = 50$ GeV. Therefore, the range of desired scattering energy is $10 < E' < 40$ GeV which corresponds to the range of scattering angles $2.25 < \theta_{lab} < 9$ mrad. Consequently, the spectrometer was designed for the detection of very

[1]The f.o.m. stands for *figure of merit* M_s that is defined by [52]

$$M_s = P_{e^-}^2 A_{PV}^2 \frac{d\sigma}{d\Omega} \Delta\Omega \sim \frac{1}{T}, \tag{3.14}$$

where P_{e^-} is the polarization, T is the total running time of the experiment, and $\Delta\Omega \sim \Delta\cos\theta_{lab}\Delta\phi$ is the solid angle. Here, θ_{lab} is the scattering angle in the lab frame and ϕ is the azimuthal angle.

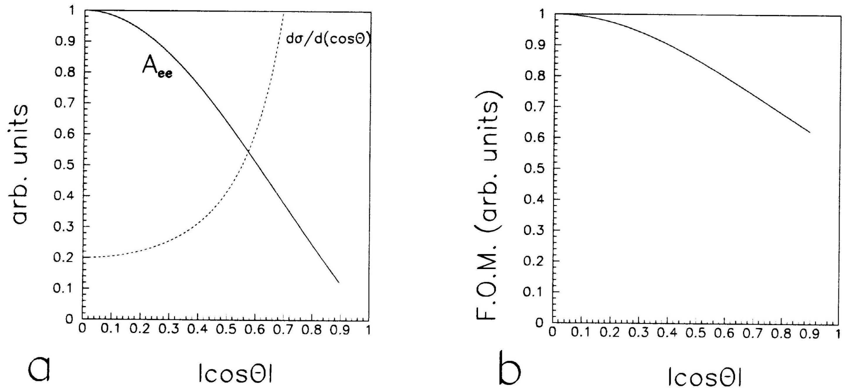

Figure 3.11: The behavior of the asymmetry, the differential cross section, and the figure of merit as a function of $|\cos\theta_{cm}|$.

forward-angle ($0.27^o - 0.41^o$) Møller scatters with the supperession of photon and *ep* elastic and inelastic background.

2. The experimental parity violating asymmetry A_{PV} was expected to be 150 ppb, which is almost eight order of magnitude smaller than the electromagnetic asymmetry A_{QED} from polarized electron-polarized iron. Therefore, all the spectrometer equibments should not be made of iron. Therefore, all pieces of beam pipe were made of Aluminum and all collimators have been made of copper or non-magnetic tungsten.

3. The Møller detector should be located as far from the target as possible so that the Møller/*ep* radial separation at the detector is maximized. Therefore, the spectrometer runs almost 60 meters.

A schematic of the spectrometer is shown in Figure 3.12.

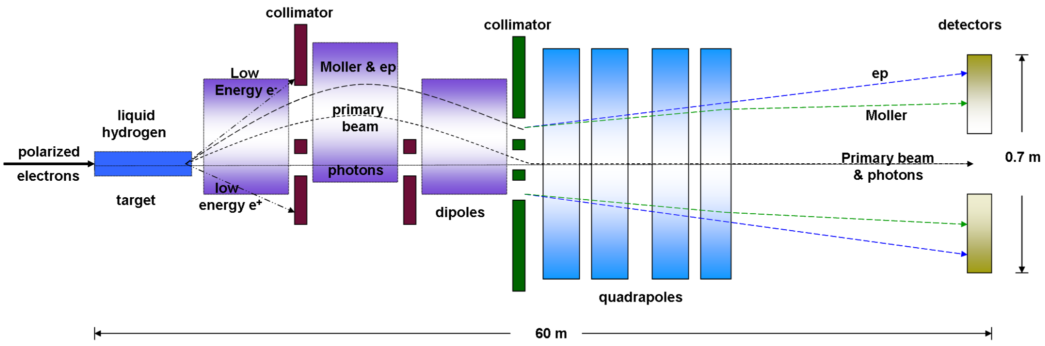

Figure 3.12: A schematic of the spectrometer

3.3.1 Dipole Magnets

The flux comming out from the Target going to the spectrometer include the following:

1. Møller scatters.

2. *ep* scatters.

3. Primary beam at the initial beam energy 48 GeV.

4. Soft (low-energy) particles which include photons, positrons and electrons.

The first part of the spectrometer is a set of 3 dipole magnets, known as the *dpiole chicane*. These magnets bend all charged particles away from the beam axis, allowing collimation of the high energy photons, which are generated by the target along the beam axis. Therefore, the primary beam as well as the Møller flux travel cleanly through the dipole magnets. Copper masks have been placed inside and between the the first and second dipole to block all electrons at energies less that 9 GeV.

The Dipole magnets were designed to preserve the azimuthal symmetry of the scattered flux. However, the azimuthal symmetry is slightly distored leaving the dipole magnets. This effect was corrected by the second set of magnets; *the quadrpole magnets* (discussed below).

All charged particles travelling through the dipole magnets exercise synchrotron radiation in the horizontal plane. This energy loss [2] causes the Møller flux to shift about 3 mm off-center at the detector face. This effect, however, can be corrected by adjusting the field of the third dipole to keep the Møller fulx.

3.3.2 Photon Collimators

Two photon collimators, each is a 40-radiation-length tungsten cylinder centered on the beam axis, have been used to suppress the photon flux. The first collimator is located between the first and second dipoles. The second collimator is immediately located behind the second dipole.

3.3.3 Momentum Collimator

The momentum collimator is immediately placed behind the third dipole magnet. It is made of two concentric cylinders, connected by two pices of metal in the horizontal plane as shown in figure 3.14. The thickness of the two cylinders as well as the two connectors is 20 *r.l.* of copper (the front side) plus 20 *r.l.* of tungsten (the rear side). This particular design for the momentum collimator defines the momentum acceptance of the spectrometer. Only Møller flux, with momenta in the range $11 - 25$ GeV, and *ep* scatters, with momenta of ~ 40 GeV, can pass

[2]The amount of energy loss due to the synchrotron radiation is proportional to the momentum-square of the charged particle

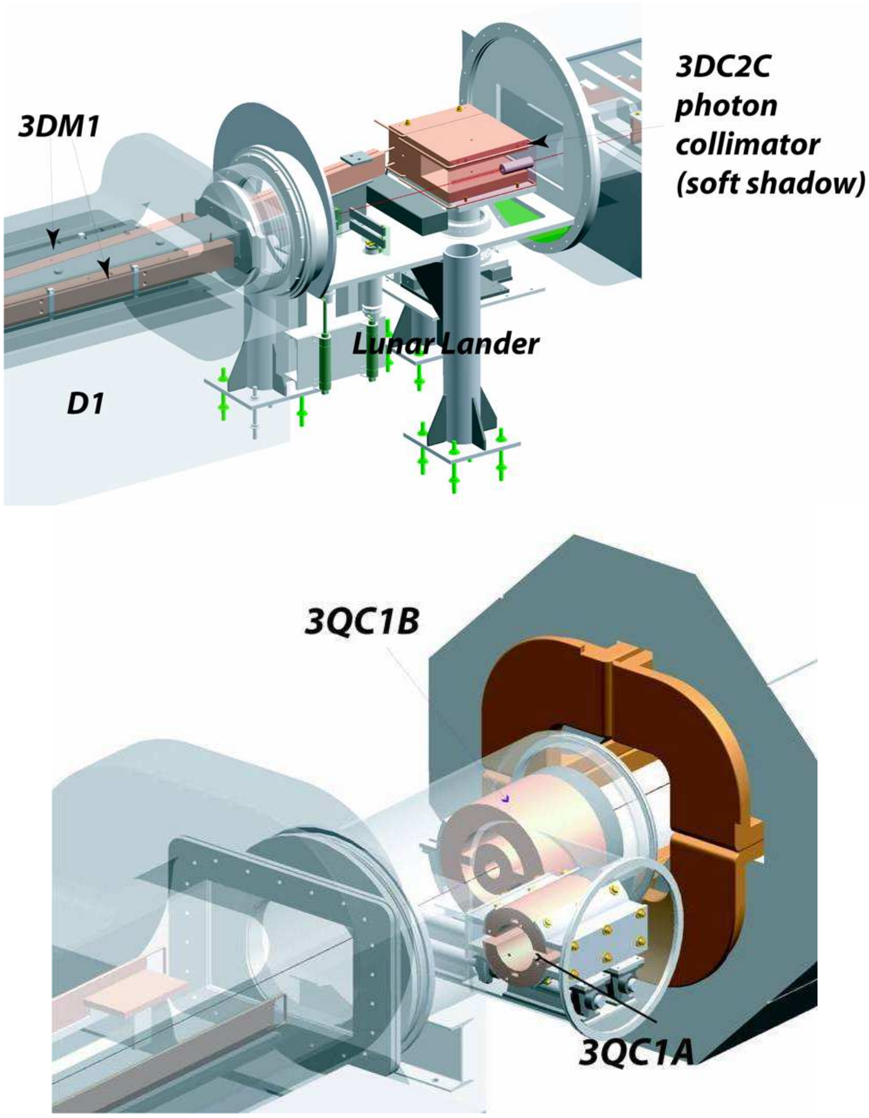

Figure 3.13: Top: a schematic of the photon collimator. Bottom: a schematic of the *holy* collimator (front) and the momentum collimator (back). 3QC1A and 3QC1B are the common experimentral names for the *holy* collimator and the momentum collimator, repectively

through this collimator.

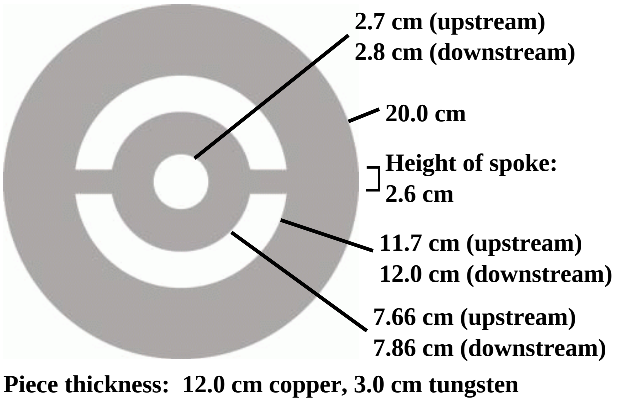

Figure 3.14: A schematic of the momentum collimator. Upstream and downstream refer to the front and rear sides, respectively.

3.3.4 *Holy* Collimator

The *holy* collimator can be moved into and out of the beam. When it is moved into the beam, it completely blocks the momentum acceptance of momentum collimator. It consists of two semi-cylindical shells as shown in Figure 3.13. The main use of this collimator is the study of the inelastic *ep* flux.

Four 1x1 cm holes have been cut in the holy collimator at various radii but they were 90^o apart. When this collimator was inserted, the holes created a very clean separation between the Møller and the ep flux at the detector face. Two larger holes (2x2.6 cm) were also cut in the holy collimator, which were used for the polarimetry measurement.

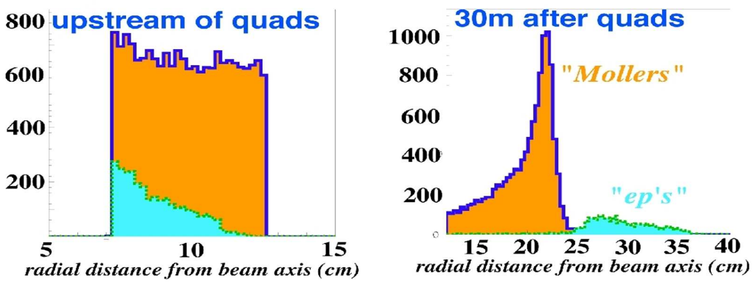

Figure 3.15: A simulated radial profile of the Møller and *ep* fluxes coming out from the momentum collimator (*left*) and after passing the quadrapole magnets (*right*).

3.3.5 Quadrupole Magnets

As we mentioned earlier, the flux leaving the momentum collimator is a mixture of 11-25 GeV Møller scatters and 40 GeV *ep* scatters with very-forward scattering angles: $4 < \theta_{lab} < 7$ mrad . Both scatters are then focused on the detector face by a lens consisting of four quadrupole magnets, which sit right after the momentum collimator. The quadrupole focusing is proportional to the energy of the particle passing through them. Therfore, the lower energy Møller flux is much more strongly focused than the *ep* flux, *i.e.*, the quadrupole magnets provided a clean separation between the Møller flux and the *ep* flux.

Figure 3.15 shows a simulated profile of the Møller and *ep* fluxes right after passing through the momentum collimator and 30 meters after passing the quadrapole magnets. This Figure illustrates the sigle peak for both Møller and *ep* scatters coming out from the momentum collimator. However, after passing the quadrupole magnets, there are two peaks: the inner one is for the lower energy Møller scatters and the outer peak is for the highr-energy *ep* scatters.

3.3.6 Synchrotron Collimators

There are two pices of metal, known as *the spokes*, that connect the inner and outer cylinders of the momentum collimator. These pices help to block the synchrotron radiation that is created in the dipole magnets. Therefore, they are called the synchrotron collimators. However, some light light passes through the central hole of the momentum collimator. Therefore, two additional sets of synchrotron collimators are used to block the remaining synchrotron radiation. The first set is made of tugsten (20 r.l. thick), and sits right after the quadrupole magnets. The second set is made of tungsten (20 r.l. thick) as well, but it is mounted to the detector face. Both sets remain in the shadow of the momentum collimator, so that they do not block the Møller flux. Yet, 11% of the Møller flux is lost due to the synchrotron collimators.

3.3.7 Drift Pipe

There is a 30 m drift region from the quadrupole magnets to the detectors. To maintain the quality of the flux, this drift region is enclosed in an aluminum pipe that was held under vacuum. Otherwise, the flux can degrade.

The synchrotron collimators, following the quadrupole magnets, sit inside this pipe. In addition, there are seven other collimators, known as the *masks*. These masks were placed inside drift pipe. They consist of tungsten rings supported by horizontal tungsten bars. With the help of these masks, background from low- and high-energy photons that are generated at the edges of the collimators, was blocked. Moreover, the tungsten bars provided additional synctrotron protection.

3.3.8 *ep* Collimator

The flux of electron hitting the *ep* detector can leak into the Møller detectror response due to shower spreading. Between Runs I and II, a new movable collimator was added just infront of the *ep* detector, which completely blocked and absorbed the charge particles, that would otherwise hit the *ep* detector [3].

3.4 Detectors

The E158 detectros were designed to monitor the Møller asymmetry as well as the asymmetries of background processes. Therfore, E158 has seven integrating detectors:

1. Møller Detector
2. *ep* Detector
3. Pion Detector
4. Luminosity Monitor
5. Synchrotron Light Monitor (SLM)
6. Profile Detector
7. Polarimetry Detector

A schematic of all these detectors is shown in Figures 3.16 and 3.17. In the following subsections, we will give a small idea about each one of them.

[3]Data collected during Runs II and III, was taken with the *ep* collimator inserted.

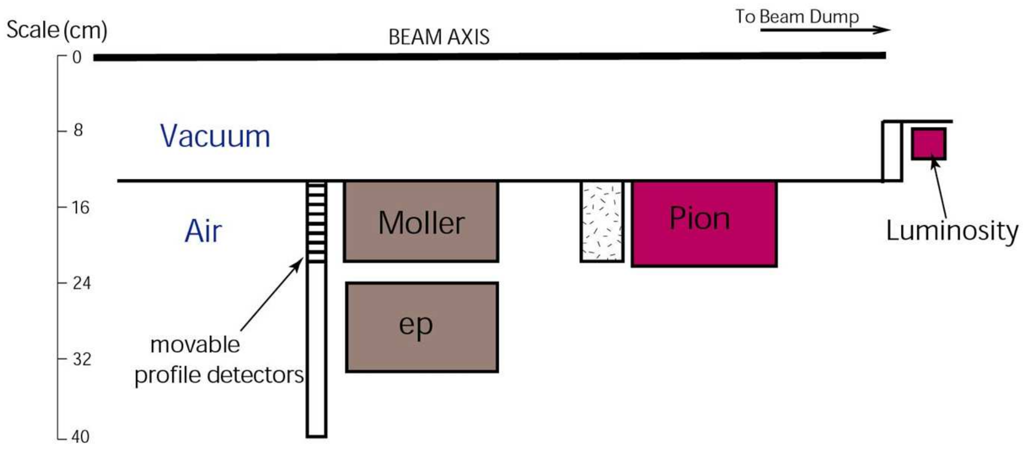

Figure 3.16: A schematic of all detectors in SLAC E158

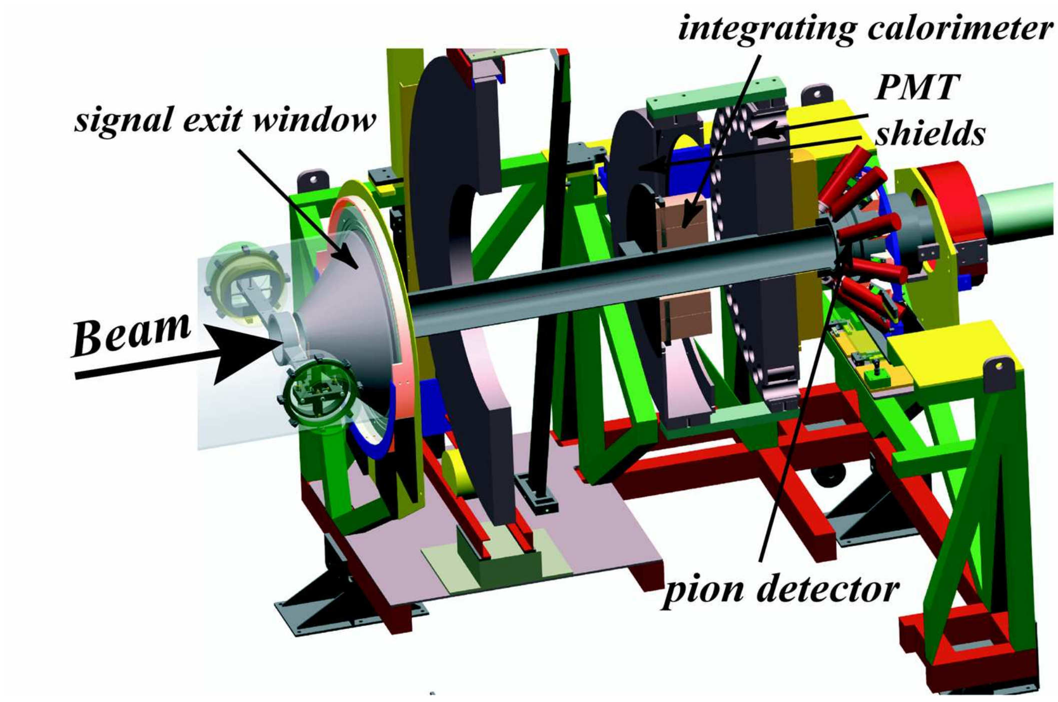

Figure 3.17: A cutaway of all detectors in SLAC E158

3.4.1 Møller and *ep* Detectors

The Møller calorimeter is the primary detector in the experiment. It was designed to meet the following requirements:

i- Maximum response to the elastically scattered electrons.

ii- Small response from pions, low energy photons, and hadrons.

iii- No response from heavy ions (non-relativistic particles).

iv- Excellent radiation resistance

The Møller and *ep* detectors [53, 54] have the same design and they are considered to be one unit, which was built using the "Quartz Fiber Claorimetry" technique. The basic principle for quartz fiber claorimetry is rather simple: when high-energy charged particles traverse dielectric media, part of the light emitted by exited atoms appears in the form of a coherent wavefront at fixed angle with respect to the trajectory–a phenomenon known as the Cherenkov effect. Such radiation is produced whenever the velocity of the particle exceeds c/n, where n is the refractive index of the medium. Here, the medium is the copper and the fibers act as optical guides for the generated light that propagates towards the photomultiplier tubes (PMTs).

The Møller-*ep* unit consists of two cylinders centered about the beam line as shown in Fig. 3.18. The inner cylinder detects the Møller electrons, while the outer one detects the *ep* electrons. Each cylinder consists of a sandwich of layers of copper plates and quartz optical fibres, oriented at 45^o to the incident electrons, so that most of the Cherenkov radiation will be emitted in a direction parallel to the fibers. The detector was 16 r.l., long enough for electrons to interact and short enough for pions not to interact.

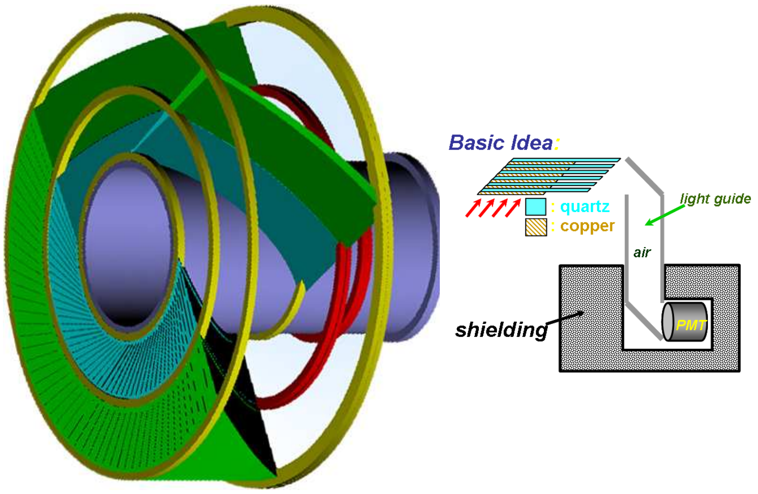

Figure 3.18: A schematic of the Møller-*ep* unit, which shows the orientation of the copper plates and quartz optical fibres with respect to the incident beam (*left*). A schematic of a layer of fibers that acts as an optical guide for the generated light that propagates towards the PMTs (*right*).

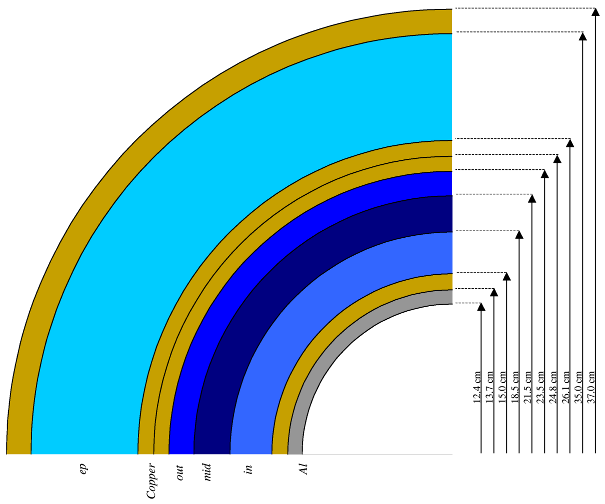

Figure 3.19: Radii of active regions of Møller and *ep* detectors.

Each layer of the 8.5 cm-wide fibers was divided into three sections (2 cm, 3 cm, and 3.5 cm) by collecting the fibers in three groups. This technique provided radial and azimuthal segmentation to the Møller detector, and divided the active volume in three rings: inner, middle, and outer as shown in Figure 3.19. Once the fibers exit the copper, they were bent, so that Cherenkov radiation–from particles travelling prallel to the beam line outside the coppler–does not produce photons. Groups of layes of fibers were bundled and connected to light guides that were buried in a lead shielding and connected to the photomultiplier tubes (PMTs).

3.4.2 Pion Detector

The π detector [55] measures the flux and rate asymmetry of the pions in the acceptance of the Møller detector. It is made of 10 fused quartz cyclinders ($\phi = 4$ cm, $L = 10$ cm) installed around the beam pipe with azimuthal asymmetry. They are tilted by 45 degrees with respect to the beam axis for better Cherenkov light collection (Figure 3.4.2).

The pion detector sits immediately behind the Møller detector and a heavy lead shielding 25 cm thick. The shielding was thick enough to kill the Møller electron flux, which was expected to be several hundred times higher than the π flux. Some shielding has also been inserted between the beam pipe and the pion counters to reduce the electromagnetic background.

3.4.3 Luminosity Monitor

The luminosity monitor is located about 70 m from the target. It was designed to detect *ep* scattered electrons as well as a large number of the high-energy Møller electrons at very forward-angle: 0.1 mrad in tha lab frame. The luminosity monitor

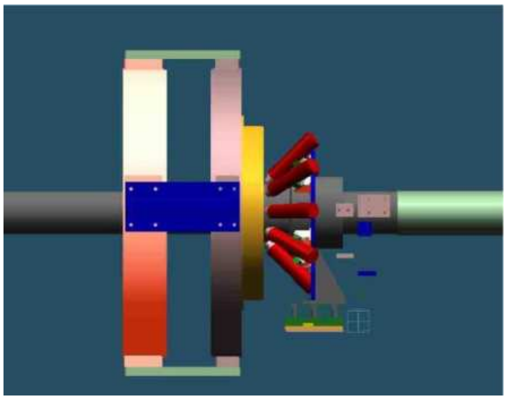

Figure 3.20: A schematic of the Møller, *ep*, and pion detectors. The pion PMTs are in red

was used to achieve two goals:

1. False beam asymmetry detection: In principle, the Møller and *ep* detectors and the heavy lead shielding sitting after the Møller detector should kill all Møller and *ep* electron flux. Therfore, the luminosity monitor should measure a null asymmetry. Therefore, any deviation from zero for the physics asymmetry, measured by the luminosity monitor, indicates a potential systematic false-asymmetry.

2. Measuring liquid hydrogen target desity fluctuations (*target boiling*): Target density fluctuations, due to the electron beam heating, can be measured by looking at the residual correlation between the Møller detector and luminosity monitor signals, after removing all fluctuations in beam parameters.

The luminosity monitor consists of 16 identical gas chamber proportional ion counters, devided into two rings, concentric around the beampipe [56]. The front ring is known as "flumi" and the rear ring is known as "blumi". There are 7 r.l. of Aluminum in front of the front ring, and 4 r.l. of Aluminum between the front ring and the rear ring. This amount of Aluminum helps to get rid of the synchrotron radiation as well as to shower the incoming signal. A schematic of the front view

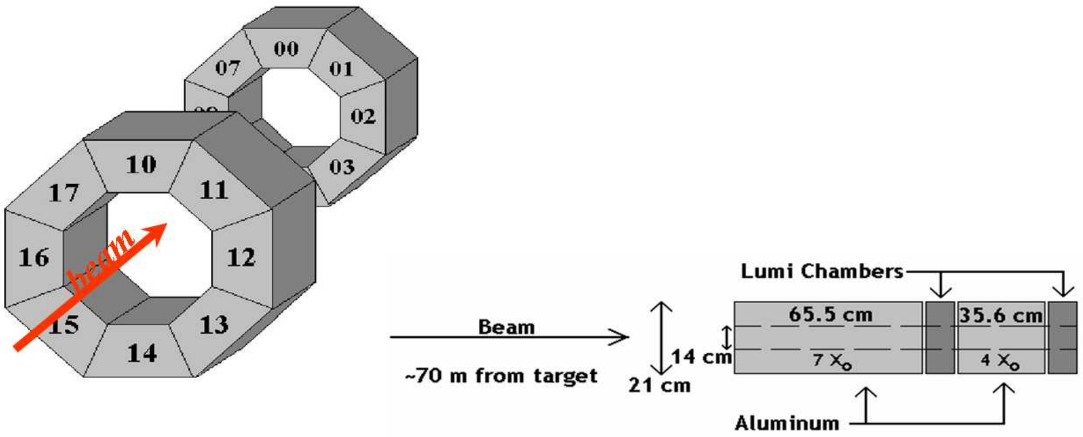

Figure 3.21: A schematic of the front view of the luminosity monitor

of the luminosity monitor is shown in figure 3.21

3.4.4 Synchrotron Light Monitor (SLM)

The synchrotron light monitor detector analyzes synchrotron radiation (SR) that is emitted when the electron beam bends at the A-Line. The SR penetrates through a 1 cm-thick aluminum flange and 1mm of Lead. These materials act as a converter to produce electrons and positrons from Compton scattering and pair production. These electrons and positrons then emit Cherenkov radiation in a 3 cm-thick quartz bar. The visible light produced is reflected by a mirror and detected by three 25 mm-diameter photodiodes housed in a lead shielding to prevent background from low-momentum photons. A schematic of the SLM is shown in figure 3.22.

The intensity of the emitted synchrotron light is directly proportional to square of the beam energy E^2. Therefore, the SLM can be used to measure the beam energy. The measurement, provided by the SLM, is not linear in the energy. Therefore, this measurement is not very useful to remove the systematic effects

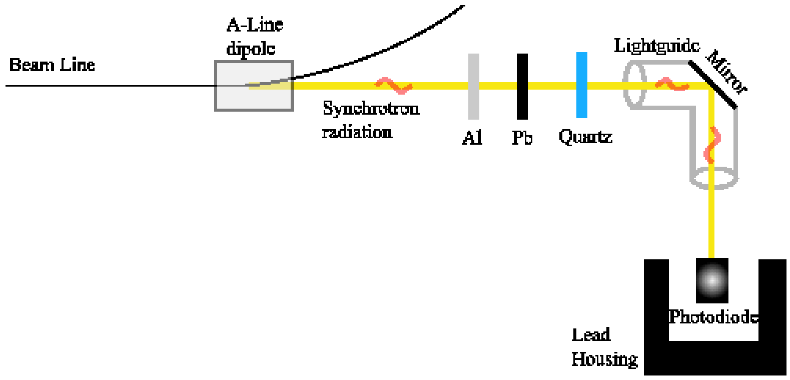

Figure 3.22: A schematic of the synchrotron light monitor (SLM).

due to the beam energy differences. Moreover, the beam position in the A-Line bend is very sensitive to variations in the beam energy.

3.4.5 Profile Detector

The profile detector is located few inches in front of the Møller detector. It was used to map the radial and azimuthal flux distribution incident on the Møller and *ep* detectors. It consists of four quartz Cherenkov counters. Each counter was mounted on a derive capable of moving radially to cover the full radial range of interest, or being away from the Møller and *ep* flux during the normal running. The derives are in turn mounted on a wheel capable of rotating 180 in order to cover the full azimuthal range (Figure 3.23).

In general, each of the quartz Cherenkov counters has a piece of quartz followed by a vacuum light guide to carry the Cherenkov light from the quartz to a PMT. However, two of them have extra features to minimize the background, for a very accurate measurements of the Møller and *ep* flux. The first feature is a tungsten

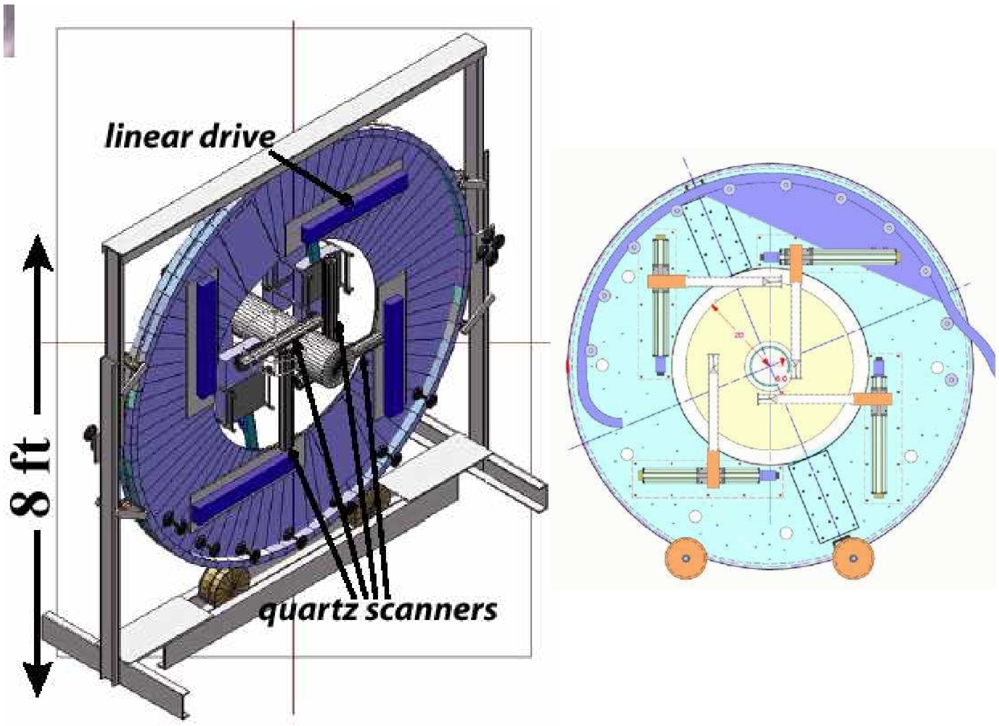

Figure 3.23: A schematic of the wheel and four Cherenkov counters of the profile detector.

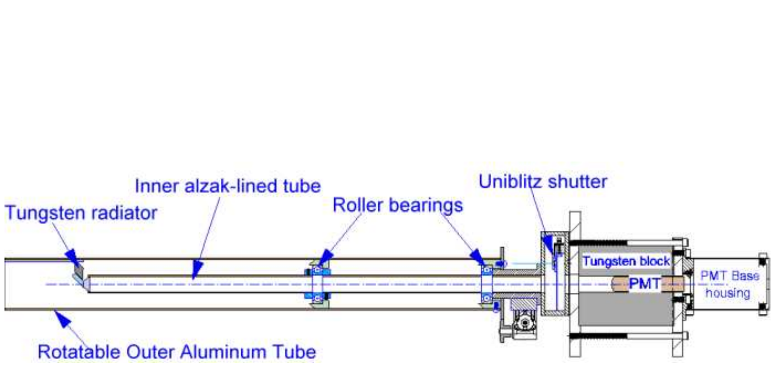

Figure 3.24: A schematic diagram of a single Cherenkov counter

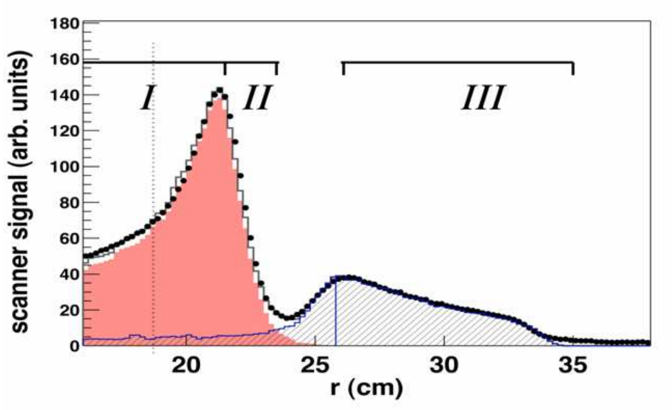

Figure 3.25: A profile scan by the profile detector. The location of the Møller detector, regions I and II, and the *ep* detector, region III, are indicated. Data are shown by closed circles. The Monte Carlo result is given by the open histogram with contributions from Møller (shaded) and *ep* (hatched) shown, separately

preradiator placed in front of the quartz to block the low-momentum particles and shower the high-momentum ones. The second feature is a shutter that blocks all photons. A schematic diagram of one of these two Cherenkov counters in shown in Figure 3.24. A tipical profile scan is shown in Figure 3.25, showing the radial acceptance of the Møller and *ep* detectors.

Chapter 4

Analysis of the Møller Asymmetry

4.1 Data

E158 collected physics data for three different periods of time (3 *Runs*[1]): spring 2002, fall 2002, and summer 2003. The number of pulse pairs that were collected for these three *Runs* is 107.8×10^6, 117.8×10^6, and 154.5×10^6 pairs, respectively. This data was collected at a rate of 120 Hz (most of the time) or 60 Hz and at two different beam energies (45 GeV and 48 GeV). The beam energy was changed 3, 2, and 7 times and the half-wave-plate state was flipped 20, 12, and 29 times in Runs I-III, respectively.

Each data set was divided into subsets of pairs, called "*runs*." Each run has typically 4×10^5 pairs. Each data set was also divided, on the basis of the energy

[1] *Run* refers to the data set that was collected for a certain period of time. *Run III* in particular refers to the data that was collected for the summer 2003.

state and the half-wave-plate state, into subsets of runs called "*slugs.*" For Run III, for instance, the data was divided into 37 slugs.

Not every event, collected during the physics Runs, can be used in the analysis. In fact, two types of *cuts* were applied to the whole data set. The first type is known as the *baseline cuts.* These cuts removed all data taken during any hardware failure. The second type of cuts were applied in the analysis process. They were used to reduce the systematic uncertainties. The details of these cuts are discussed in Ref. [50]. A list of all cuts and their effects on a data sample are shown in Table 4.1. The sample contains about 19×10^6 pulse pairs, which represents about 10.7% of the whole data set before applying any cuts. Both the basline cuts and the systematics cuts removed about 3×10^6 pulse pairs, *i.e.*, a loss of 15.6% only occurred. In fact, applying all cuts to the whole data set results in a reduction of only 14% only [57].

4.2 Møller Detector Analysis

In this section, we will discuss the analysis of the data that was collected by the Møller detector. Corrections from background processes will be discussed later.

4.2.1 Asymmetry Equation

Detector Signal

The cross section σ is proportional to the detected scattered flux, *i.e.*, the detector signal S. Therefore, the measured asymmetry $A_{p_i}^{meas}$ in the cross section is equivalent to:

$$A_{p_i}^{meas} = \frac{S_{R_i} - S_{L_i}}{S_{R_i} + S_{L_i}}, \tag{4.1}$$

Cut	**Number of Pairs ($\times 10^6$)**	**Percentage**
Baseline	1.279	6.61%
Regression Slopes	0.000	0.00%
Beam	1.112	5.74%
Toroid Agreement	0.001	0.01%
Transmission	0.010	0.05%
Energy	0.239	1.23%
BPM Phases	0.385	1.99%
Rate	0.000	0.00%
Total	3.025	15.63%

Table 4.1: List of all cuts and the number of pulse pairs that were removed by applying these cuts on a data sample.

where $S_{R_i}(S_{L_i})$ is the signal from the ith channel of the detector for the *right(left)* handed pair of pulse p.

Charge Normalization

By normalizing the channel signal to the beam charge, helicity-correlated differences in the beam intensity are automatically corrected

$$A_{p_i}^{meas} = \frac{\frac{S_{R_i}}{Q_R} - \frac{S_{L_i}}{Q_L}}{\frac{S_{R_i}}{Q_R} + \frac{S_{L_i}}{Q_L}}. \tag{4.2}$$

It is obvious form this equation that, to first order, the physics asymmetry can be written as $A_{PV} = A_{meas} - A_Q$, where the charge asymmetry, A_Q, is simply $(Q_R - Q_L)/(Q_R + Q_L)$. Yet, the residual beam asymmetry due to the beam intensity differences were calculated and subtracted from the physics asymmetry.

Beam Effects Subtractions

The corrections, due to beam asymmetries, can be expressed as a Taylor series. Taking into consideration the first-order terms only, the corrected asymmetry, for a channel i, is then given by

$$A_{p_i}^{corr} = A_{p_i}^{meas} - A_{p_i}^{beam}, \tag{4.3}$$

and

$$A_{p_i}^{beam} = s_{p_{ij}} m_p^j, \tag{4.4}$$

where $A_{p_i}^{meas}$ is the charge-normalized asymmetry for a channel i, $s_{p_{ij}}$ is a correction coefficient between this channel and the monitor j and m_p^j is the helicity-correlated difference in this monitor. The correction coefficients (slopes), s_{ij}, can be calculated in two different methods: *regression* and *dithering*.

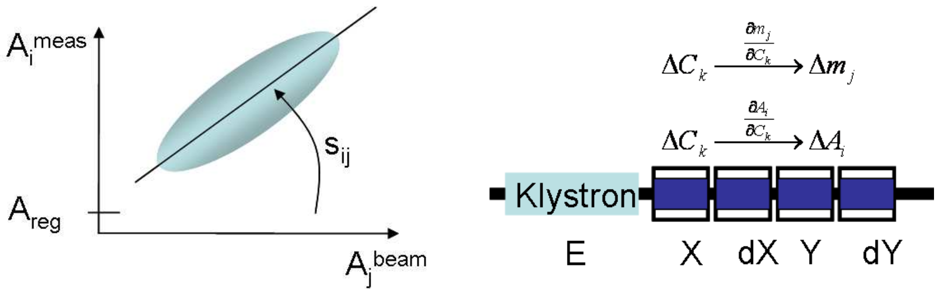

Figure 4.1: A schematic illustrating the regression (left) and dithering (right) methods of removing the beam contributions.

The correlation between the beam and the measured channel asymmetries is linear to fist-order. Consequently, it was possible to remove the beam contributions by applying a least square linear regression to the measured asymmetry of each channel. To do this, the asymmetry of each channel was plotted against all beam asymmetries (multi-dimensionally) and a single linear fit is made to the data. The regression slopes, s_{ij}, were then obtained for each channel i and for each beam parameter j. The regression slopes were calculated for every 10^3 pair of pulses, which was enough to minimize the statistical uncertainties of the linear fits.

The dithering slopes were obtained by perturbing steering coils in the accelerator C_k. We then measured the response of the BPMs, Δm_j, and the detector channels, ΔA_i^{meas}, to these perturbations. In other words, we measured the partial derivatives $\partial A_i^{meas}/\partial C_k$ and $\partial m_j/\partial C_k$. The required slopes, s_{ij}, were then obtained by solving the matrix equation

$$\frac{\partial A_i^{meas}}{\partial C_k} = \sum_j \frac{\partial A_i^{meas}}{\partial m_j}\frac{\partial m_j}{\partial C_k} = \sum_j s_{ij}\frac{\partial m_j}{\partial C_k}. \tag{4.5}$$

See Chapter 5 for more details on the dithering analysis.

The dithering method does not statistically minimize the width of the experimental asymmetry. Consequently, the width of the asymmetry determined from the dithering analysis might be larger than the width of the regressed asymmetry. Therefore, the regression analysis was the dominant for calculating the experimental asymmetry.

Weights

Our formula for calculating the asymmetry accounts for one channel only. However, the overall detector asymmetry must be calculated. The simplest formula for the total asymmetry is the sum of all individual channel asymmetries:

$$A_p^{reg} = \sum_i A_{p_i}^{reg}. \tag{4.6}$$

Since different channels detect different numbers of incident electrons, Equation 4.6 can not be useful. Therefore, individual channels should be weighted

$$A_p^{reg} = \frac{A_{p_i}^{reg} w^i}{w_i^i} = \frac{(A_{p_i}^{meas} - s_{p_{ij}} m_p^j) w^i}{w_i^i}. \tag{4.7}$$

The weighting scheme, w_i, should removes most of the statistical error. So in order to minimize the overall detector width, the variance

$$V(A) \quad = \quad W_i W_j cov(A^i, A^j), \tag{4.8}$$

where

$$\begin{aligned} W_i &= \frac{1}{\sigma^2(A_i)}, & (4.9)\\ cov(A_i, A_j) &= \frac{1}{N_p}(\sum_p A_i A_j) - \frac{1}{N_p^2}(\sum_p A_i)(\sum_p A_j), & (4.10) \end{aligned}$$

is minimized to obtain the weights w_i [58].

One-Run Asymmetry

So far, A_p^{reg} has been defined for one (L,R) pair of pulses, p. For one run, the value of the detector asymmetry, A_r^{reg}, is given as the mean value of the per-pair asymmetry, A_p^{reg}, over all pairs of this run:

$$\begin{aligned} A_r^{reg} &= \frac{\sum_p A_p^{reg}}{N_p} \\ &= \frac{1}{N_p}\sum_p [\frac{A_{p_i}^{meas} w^i - s_{p_{ij}} m_p^j w^i}{w_i^i}], \end{aligned} \tag{4.11}$$

where N_p is the total number of pulse pairs in one run, $A_{p_i}^{meas}$ the charge-normalized per-pair asymmetry of a channel i, $s_{p_{ij}}$ is the per-pair regression slope between this channel and a monitor j, m_p^j is the per-pair helicity-correlated difference of the monitor j, and w_i is the weight of this channel for a particular run. Note that the weights w_i are constant over the whole run, *i.e.*, are the same for all pulse pairs in one run. The width and the error of A_r^{reg} are simply obtained from the distribution:

$$\sigma^2(A_r^{reg}) = \frac{1}{N_p}\sum_p (A_p^{reg} - A_r^{reg})^2, \tag{4.12}$$

$$\delta A_r^{reg} = \frac{\sigma^2(A_r^{reg})}{\sqrt{N_p}}. \tag{4.13}$$

To obtain the asymmetry of a number of runs, N, the statistical-weighted average of A_r^{reg} is taken:

$$\begin{aligned} A^{reg} &= \frac{\sum_{r=1}^N A_r^{reg} w^r}{\sum_{r=1}^N w_r}, \\ w_r &= \frac{1}{\sigma_r^2}, \end{aligned} \tag{4.14}$$

where σ_r is the error on the detector regressed-asymmetry for a run r. The width and the error of A^{reg} are given by

$$\frac{1}{\sigma^2(A^{reg})} = \sum_{r=1}^{N} \frac{1}{\sigma^2(A_r^{reg})}, \tag{4.15}$$

$$\delta A^{reg} = \frac{\sigma^2(A^{reg})}{\sqrt{N}}, \tag{4.16}$$

where N is the total number of runs for a particular energy state.

One-Energy Asymmetry

To calculate the total experimental asymmetry, the data must be separated by energy state, so that the different ep corrections can be added to each set. Then we combine the asymmetry for two energy states according to:

$$A_{total} = \sum_E W_E A_E, \tag{4.17}$$

where

$$W_E = \frac{\frac{1}{\delta A_E^2}}{\sum_E \frac{1}{\delta A_E^2}}. \tag{4.18}$$

The statistical error on A_{total} are obtained by

$$\delta A_{total}(stat) = \frac{1}{\sqrt{\sum_E \frac{1}{\delta A_E^2}}}. \tag{4.19}$$

Blinding

Finally to prevent bias of the physics result, a simple blinding algorithm was used to hide the true value of the physics asymmetry. This algorithm shifts the raw asymmetry of each channel by a fixed amount A':

$$A_i^{meas} \rightarrow A_i^{meas} + A'. \tag{4.20}$$

A' is constant across all Møller channels and across all pairs.

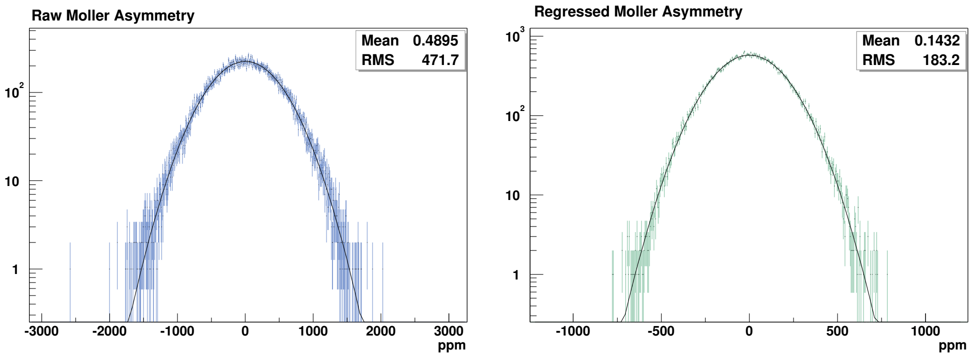

Figure 4.2: Regression analysis for the Møller detector

4.2.2 Regressed Møller Asymmetry

Only corrections due to the beam asymmetries will be taken into account in this section. Other corrections from background processes will be discussed later. The effects of the regression procedure for the Møller detector are illustrated in Figure 4.2. The first frame of this figure shows the raw asymmetry distribution for one *run*. The distribution has an *rms* of 471 ppm. Regression against the energy, position and angle BPMs, which is shown in the second frame, reduces the *rms* to 193 ppm.

In order to examine the distribution of the asymmetry and determine whether the data has outliers or not, we plot the asymmetry versus *run number* and versus *slug number*, as shown in Figure 4.3. The data is fit with a zero-degree polynomial, which gives the total asymmetry averaged over time. In principle, the χ^2 and the associated probability from this fit are a measure of experimental consistency. To see the shape of the distribution around the mean, one can look at the *pull plots* (Figure 4.4), where the quantities $\frac{A_r^{reg}-A_{total}}{\sigma(A_r^{reg})}$ and $\frac{A_p^{reg}-A_{total}}{\sigma(A_p^{reg})}$ are histogramed for all runs and for all pulse pairs , respectively.

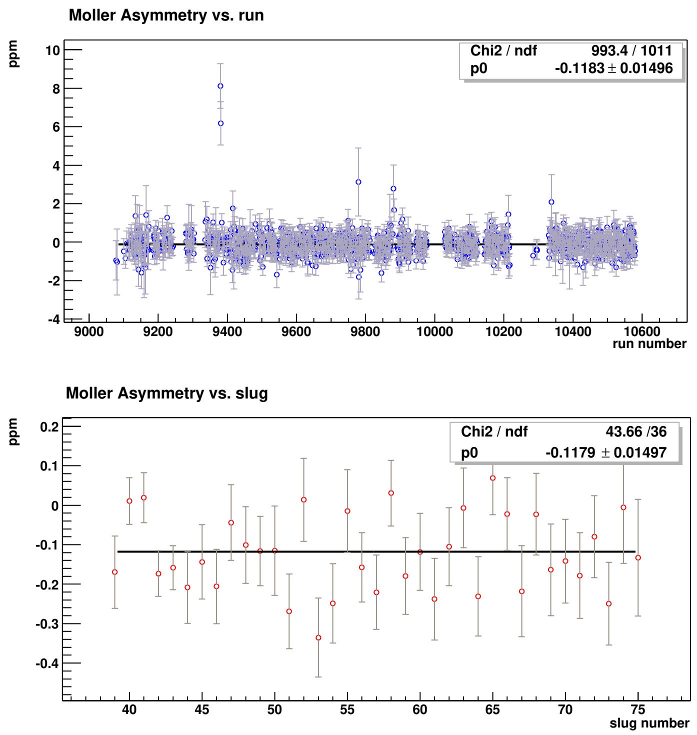

Figure 4.3: The regressed Møller asymmetry as a function of run number (top) and slug number (bottom) in Run III.

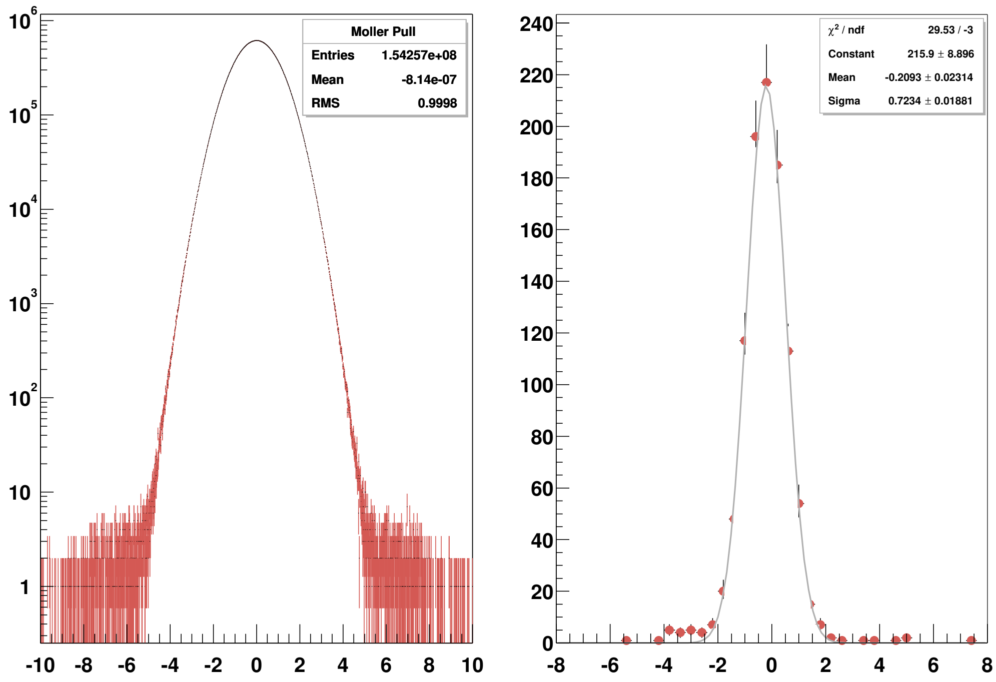

Figure 4.4: The regressed Møller asymmetry pull plot per pulse pair (*left*) and per run (*right*) in Runs III.

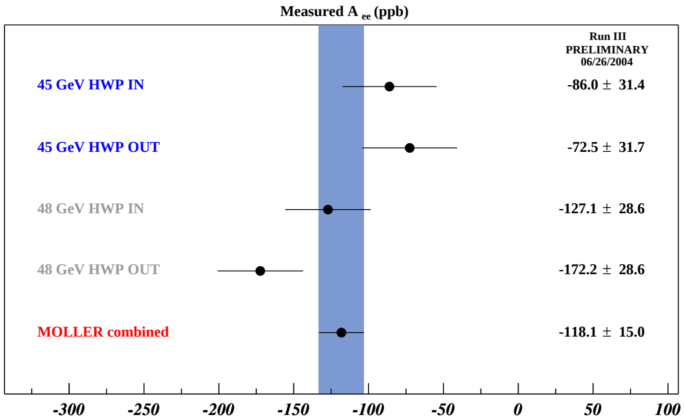

Figure 4.5: The regressed Møller asymmetry at different settings of the HWP and the energy in Run III. The asymmetries have already been corrected for the reversal sign.

As was discussed earlier, the asymmetry reversal techniques should cancel the systematic effects. Therefore, it is necessary to look at the experimental asymmetry for the different settings of the half-wave-plate and the energy of the beam. Figure 4.5 shows the asymmetry for these experimental settings.

Another comparison can be made by looking at the experimental asymmetry for the individual rings of the Møller detector, since the asymmetry is not expected to vary much between them (Figure 4.6). The IN and MID rings agree very well, but the OUT ring is slightly shifted. Higher-order systematics, which will be discussed later, are the cause of this shift.

The last comparison can be made by looking at the experimental asymmetry for the three data sets [2] as shown in Figure 4.7. Note that this is not the final

[2] Run I and Run II were discussed in details in Refrences [59, 60].

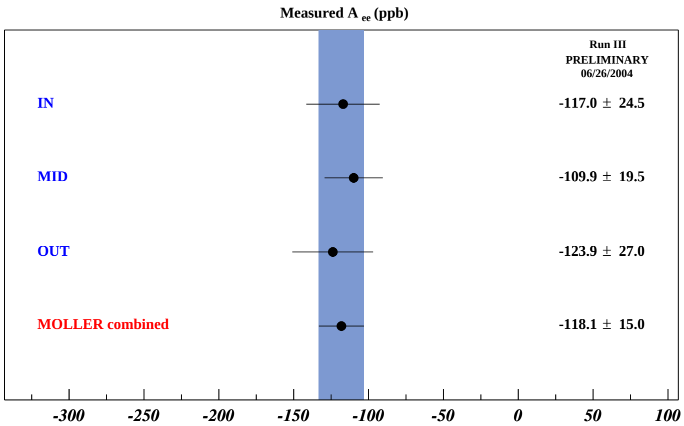

Figure 4.6: The regressed Møller asymmetry for each ring in Run III.

result yet. As was mentioned earlier, in this section we considered corrections due to beam fluctuations only. Therefore, the uncertainties shown in Figure 4.7 are only the statistical uncertainties.

4.2.3 Azimuthal Dependence in Møller Asymmetry

The actual measured Asymmetry, A_{meas}, has two components:

$$A_{meas} = A_{PV} + A_T, \tag{4.21}$$

where A_T is the transverse asymmetry due to a small component of transverse polarization of the beam (see Chapter 7 for more details). A_T can be written as

$$A_T = A_d \sin\phi, \tag{4.22}$$

where A_d is called the *dipole*, while A_{PV} refers to what is called the *monopole*. The azimuthal angle, ϕ, of the scattered electron around the beam direction is measured

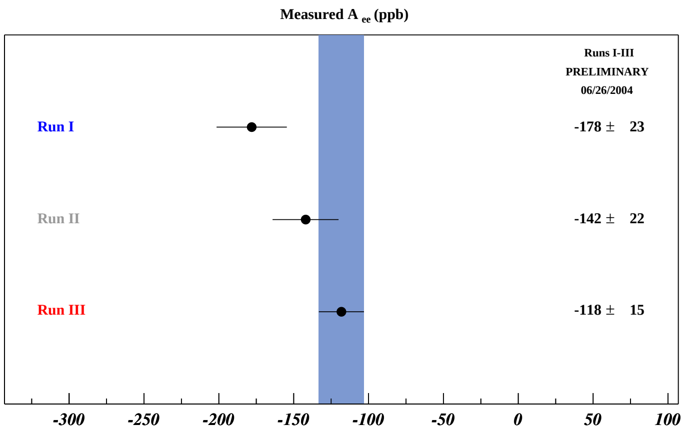

Figure 4.7: The regressed Møller asymmetry for Runs I-III. Only statistical uncertainty and beam corrections are considered in this plot.

from the direction of the transverse polarization. A dipoleY, A_{dy}, can result from a residual P_x component of the beam polarization, due to imperfect horizontal beam steering and a dipoleX, A_{dx}, can result from a residual P_y component of the beam polarization, due to imperfect vertical beam steering. Therefore, A_T takes the form

$$A_T = A_{dx} \sin\phi + A_{dy} \cos\phi. \tag{4.23}$$

The *dipole asymmetries* A_{dx} and A_{dy} can be then computed using the measured asymmetry after regression:

$$A_{dx} = \frac{2}{N_j} \sum_i A_i^{reg} \sin\phi^i, \tag{4.24}$$

$$A_{dy} = \frac{2}{N_j} \sum_i A_i^{reg} \cos\phi^i, \tag{4.25}$$

and

$$\phi^i = \frac{2\pi i}{N_j} - \delta_j, \tag{4.26}$$

where A_i^{meas} is the measured asymmetry for a channel i and N_j and δ_j are the number of channels and the phase of the ring j, respectively. The phases δ_j were calculated using the dithering analysis [61].

Figure 4.8 shows the observed *dipole* asymmetry as a function of the azimuthal angle ϕ (the channels of the individual rings of the Møller detector). Table 4.2 summarizes the observed dipole asymmetries of the Møller detector.

	A_{dx} (ppb)	A_{dy} (ppb)				
Detector	**Run I**		**Run II**		**Run III**	
IN	-74.6 ± 39.4	217.5 ± 36.9	-41.2 ± 36.0	41.5 ± 33.4	-60.9 ± 30.8	-15.4 ± 28.6
MID	-69.4 ± 32.8	155.8 ± 30.2	48.4 ± 30.2	62.0 ± 28.5	-50.8 ± 25.4	24.1 ± 22.8
OUT	99.0 ± 74.5	489.2 ± 73.4	320.8 ± 70.3	142.6 ± 61.2	-106.7 ± 38.0	122.2 ± 34.8

Table 4.2: The *dipole* asymmetry of the Møller detector in Runs I-III.

Now the question is how do we correct the measured Møller asymmetry due to that small non-zero transverse beam polarization?

This azimuthal asymmetry is not necessarily bad. These asymmetries, measured by the channels of the Møller detector, should average to zero (parity is conserved by QED interactions). This happens only if the weights of these channels are picked appropriately. Therefore, the channels weights w_i (Equation 4.8) should be modified in order to nullify the azimuthal dependence. The azimuthal bias in the measured asymmetry takes the form:

$$\Delta\langle A\rangle = A_{dx} W_i \sin\phi^i + A_{dy} W_i \cos\phi^i. \tag{4.27}$$

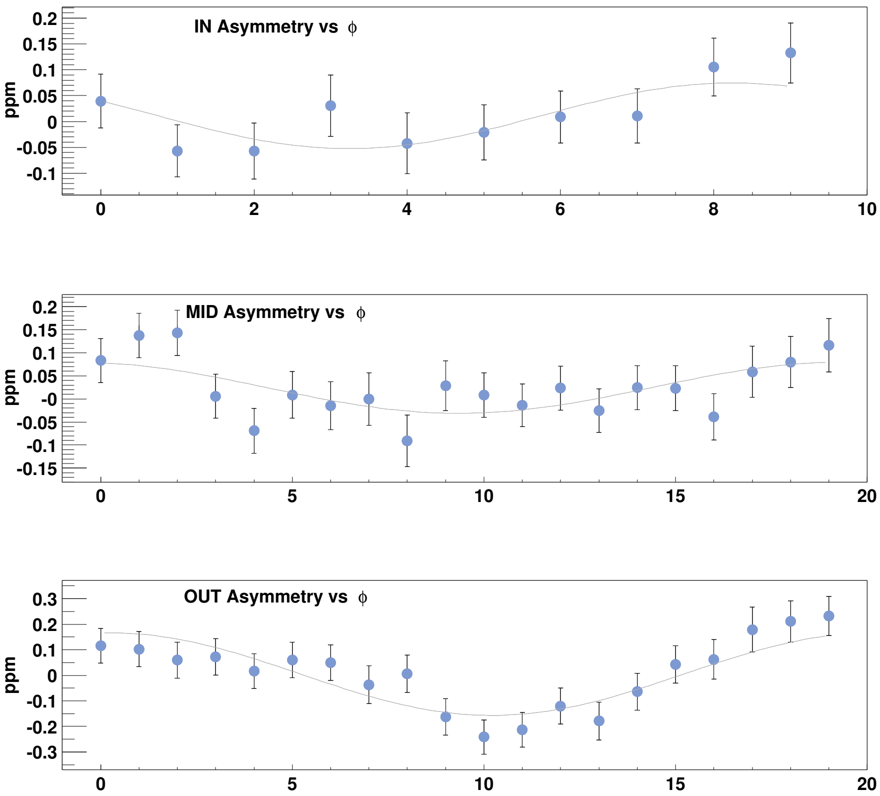

Figure 4.8: The dipole asymmetry vs. the azimuthal angle ϕ in Run III.

To avoid such bias, the sum $(A_{dx}W_i \sin\phi^i)^2 + (A_{dy}W_i \cos\phi^i)^2$ is simply minimized. Therefore, the whole sum:

$$W_i W_j cov(A^i, A^j) - (A_{dx}W_i \sin\phi^i)^2 - (A_{dy}W_i \cos\phi^i)^2, \tag{4.28}$$

should be minimized in order to get the weights w_i. This attepmt, unfortunately, results in a bigger statistical error in the Møller asymmetry. Therefore, it was not applied. On the other hand, from the data taken by running the electron beam at 46 GeV and 43 GeV, where the beam polarization was fully transverse, it was estemated that the contribution due to transverse polarization component was -8 ± 3 ppb for Run I, -5 ± 3 ppb for Run II, and -5 ± 2 ppb for Run III [62].

4.3 Asymmetry Corrections

The measured asymmetry may be written as:

$$A_{LR}^{meas} = A_{LR}^{phys} + A_{LR}^{beam} + A_{LR}^{bkgd}, \tag{4.29}$$

where A_{LR}^{phys} is the Møller physics asymmetry to be determined, and A_{LR}^{beam} and A_{LR}^{bkgd} are contributions to the measured asymmetry from beam asymmetries and from background processes. In the following secitons we will discuss these contributions to the measured asymmetry.

4.3.1 Beam Systematics

To first order, six correlated beam parameters described the trajectory of a beam pulse: charge, energy, and horizontal and vertical position and angle. The regressed beam asymmetries due to these six parameters are calculated in the same way the

Møller asymmetry is calculated (Equation 4.11). Therefore, for a single run, r, one can write:

$$A_r^{beam} = \frac{1}{N_p}\sum_p \frac{s_{p_{ij}} m_p^j w^i}{w_i^i}, \tag{4.30}$$

and the beam asymmetry for a set of runs, N, would be

$$A^{beam} = \frac{\sum_{r=1}^N A_r^{beam} w^r}{\sum_{r=1}^N w_r}, \tag{4.31}$$

where w_r is given by Equation 4.14. The beam asymmetries and their corrections are summarized in Table 4.3. Errors on corrections are not shown in this table, but they are discussed below.

Beam Parameters	**Beam Asym.**	**Corr. (ppb)**
Q	73.3±288 ppb	−0.9
E	−2.3±1.9 KeV	24.3
X	9.4±5.9 nm	−10.4
Y	11.8±6.0 nm	−20.8
θ_x	−0.0±0.2 nrad	6.2
θ_y	−0.2±0.1 nrad	3.2
Total	-	1.7

Table 4.3: Beam differences and asymmetries for Run III.

Systematic Uncertainties from First-Order Beam Asymmetries

The error for each beam correction is dominated by the jitter in the beam parameters. Therefore, they can not be assigned as a first-order systematic error on the experimental asymmetry. On the other hand, we used the the *timeslot* data to calculate these first-order systematic errors. Figure 4.9 shows a comparison between the two data: *timeslot 0* and *timeslot 1.* We take the difference between the regressed asymmetry of the *timeslot 0* and the regressed asymmetry of the *timeslot 1.* We then divide this difference by the difference between the corresponding beam corrections. This ratio is then used as a suppression factor for the beam corrections. To calculate these values, different detectors were examined so that we get the smallest suppression factor. For example, the dipole asymmetries are sensitive to beam asymmetries and in particular, dipoleX is sensitive to the beam position x and to the beam angle θ_x. Therefore, the dipoleX asymmetries of the MID and OUT detectors were used to calculate the systematic errors of the beam parameter x and θ_x, respectively. Similarly, the dipoleY asymmetries of the MID and OUT detectors were used to calculate the systematic errors of the beam parameters y and θ_y, respectively. Finally, the systematic error on the energy was estimated using the monopole asymmetry for the Møller detector.

Using the observed beam corrections, A_i^{beam}, we estimate the systematic errors, δ_i^{beam}, due to the first-order beam asymmetries according to [63]

$$\delta_i^{beam} = |\frac{A_0^{reg} - A_1^{reg}}{A_{0_i}^{beam} - A_{1_i}^{beam}} \cdot A_i^{beam}|. \tag{4.32}$$

where i here is an index for one of $E, x, y, \theta_x, \theta_y$. The total systematic error on the Møller asymmetry due to the the first-order beam corrections is then the quadrature sum of the systematic uncertainties on each beam correction;

$$\delta = \sqrt{\sum_i \delta_i^2}, \tag{4.33}$$

Table 4.4 summarizes the beam corrections, calculated by regression, the suppression factors, and the resulting systematic errors associated with each beam

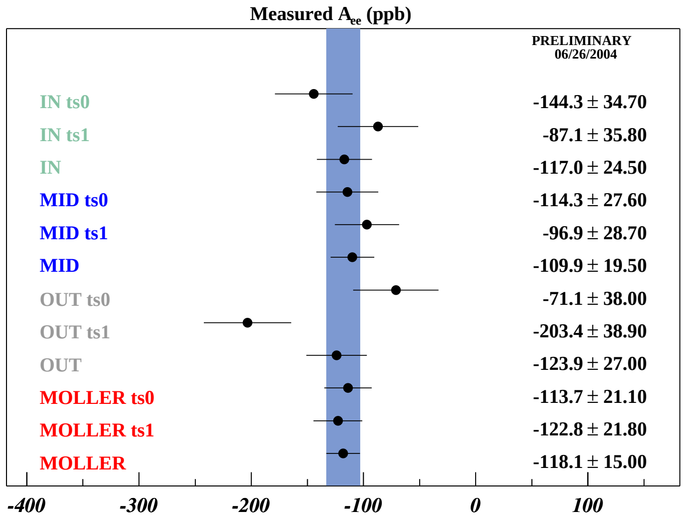

Figure 4.9: The regressed Møller asymmetry for the two timeslots (ts0 & ts1) in Run III.

parameter. For the ratio, $(A_0^{reg} - A_1^{reg})/(A_{0_i}^{beam} - A_{1_i}^{beam})$, used in Equation 4.32, one standard deviation was considered and not the central value. This is considered to be a conservative way to estimate the systematic errors δ_i^{beam}. By applying this procedure, the overall first-order systematic uncertainties, together with systematic uncertainties from beam false asymmetries (discussed below), were found to be $1.13 + 0.87 = 2$ ppb. By applying the same procedure to Run I and Run II, first-order systematic uncertainties were found to be 3 ppb and 2 ppb, respectively. An comparison between the beam corrections for Runs I-III is shown in Figure 4.10.

Systematic Uncertainties from Beam False Asymmetries

The readout of a monitor, X, can be written as $X = C \cdot V$, where C is the calibration constant and V is the voltage deposited in the cavity of the BPM.

Parameters	**Corr. (ppb)**	**Suppression**	**Error (ppb)**
Q	-0.9	-	0.0
E	24.3	2.58%	0.63
X	-10.4	2.04%	0.21
Y	-20.8	3.57%	0.74
θ_x	6.2	8.44%	0.52
θ_x	3.2	4.69%	0.15
Total	1.7	-	1.13

Table 4.4: Systematic uncertainties from first-order beam asymmetries.

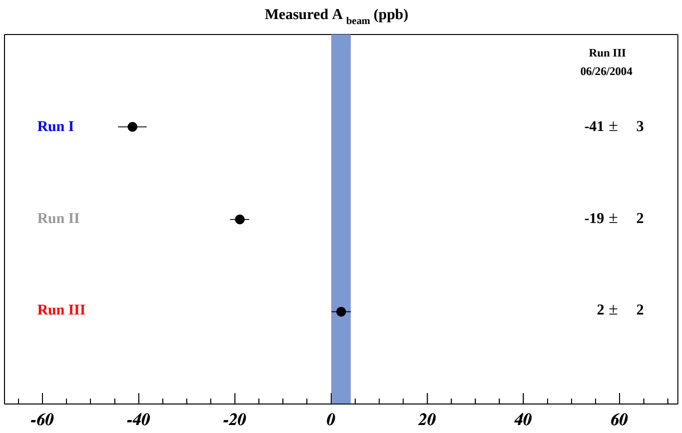

Figure 4.10: Beam corrections in Runs I-III.

Then the average and difference (known as BPM *agreement*) of two BPMs, which are measuring the same beam parameter, are given by:

$$X_{ave} = \frac{C_1V_1 + C_2V_2}{2}, \quad X_{agr} = \frac{C_1V_1 - C_2V_2}{2}.$$

Therefore, the width of the average and the difference can be written in the form:

$$\sigma(X_{ave}) = V \cdot \frac{C_1 + C_2}{2}, \quad \sigma(X_{agr}) = V \cdot \frac{C1 - C2}{2},$$

for some calculable voltage V. By solving these two equations, one can get

$$\sigma(X_{ave}) = \sigma(X_{agr}) \cdot \frac{C_1 + C_2}{C_1 - C_2}.$$

The r.h.s of this equation gives the false asymmetry. Now, if we multiply both sides of this equation with the regression slope of the associated beam parameter, we will get the systematic uncertainty due to the false asymmetry of that particular beam parameter. Results are shown in Table 4.5. The total uncertainty, which is given by the direct sum, is 0.87 ppb. Similarly, the systematic uncertainties due to the false beam asymmetry for Run I and Run II were found to be less than 1 ppb.

Systematic Uncertainties from Higher-Order Beam Asymmetries

In addition to the familiar beam systematics, which come from six beam parameters: Q, E, x, y, θ_x, and θ_y, the OUT ring of the Møller detector was particularly sensitive to other systematics. These extra systematics were unclear at first. As shown in Figure 4.11, the χ^2 distribution of the OUT ring showed significant non-statistical fluctuations, which were not explained by systematics uncertainties from first-order beam asymmetries or from false asymmetries in the beam monitors.

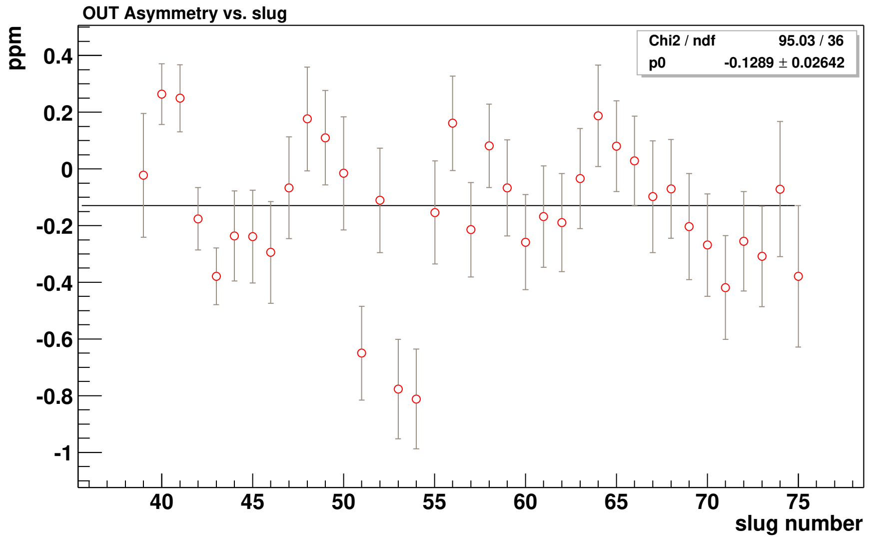

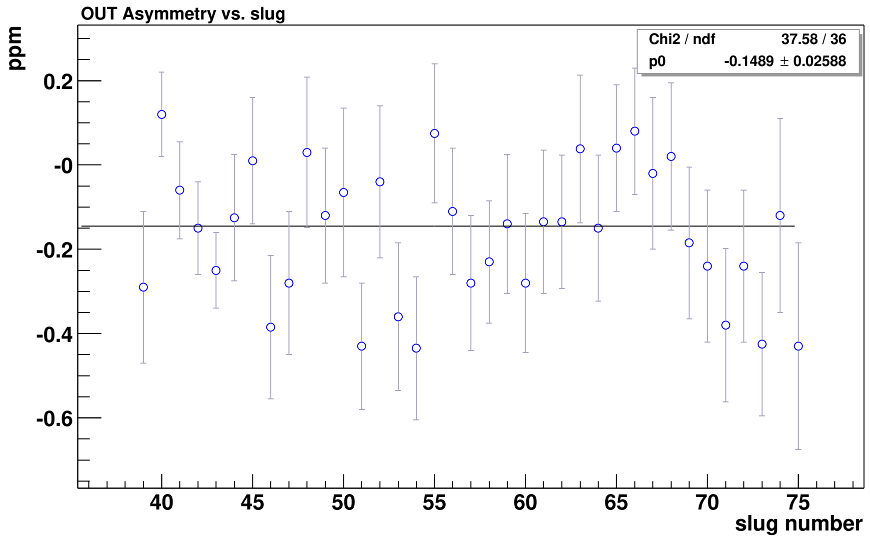

Figure 4.11: SLUG plot for the OUT ring without (*top*) and with (*bottom*) the time-dependant corrections. The χ goes down from 95/36 to 37/36.

Parameters	Regression slopes		False Asymmetry	Error (ppb)
E	-17.68	ppb/KeV	0.04 KeV	-0.77
X	0.003	ppb/nm	0.16 nm	-0.12
Y	-0.59	ppb/nm	0.07 nm	0.08
θ_x	-16.86	ppb/nrad	0.36 nm	-0.02
θ_x	18.91	ppb/nrad	0.22 nm	-0.04
Total	-		-	-0.87

Table 4.5: Systematic uncertainties from beam false asymmetries.

One hypothesis was that there is a significant variation in the shapes of the pulses, and that the electronics do not integrate pulses of different shapes in the same way. This hypothesis was carefully tested and it was proved to have a very weak effect. See Appendix A for more details.

Another possible hypothesis to explain these large χ^2 values was the existence of unmeasured beam parameters. The effects of these extra unmeasured beam parameters happen within the duration of one beam pulse and, therefore, they were undetected by the BPMs, since these BPMs integrate over the entire length of the electron beam pulse. We called these extra beam parameters: highr-order beam systematics.

In order to measure these extra beam parameters, we had to measure the beam asymmetries as a function of time inside the electron beam pulse. Therefore, we added *slice signals* from the cavity BPMs before we started collecting the data of Run III. We then regressed all detector asymmetries against these sliced signals. Such regression reduced the χ^2 of the OUT ring to roughly 1 per degree of freedom [64](Figure 4.11).

To estimate the higher-order beam systematics in Runs I and II, regression using the sliced signals for Run III, together with an analysis of the OUT ring for Runs I and II, were used [65]. The whole idea is to write down the measured asymmetry as a sum of the real physics asymmetry A_r and false asymmetry

$$A = A_r + \alpha A_{syst}, \tag{4.34}$$

where A_{syst} is the higher-order beam systematics that we hope to estimate, and α is a coefficient. Although we did not measure the quantity αA_{syst} in Runs I and II, we estimated its value using two detectors, *e.g.* IN+MID and OUT, with known expected asymmetries. If A_{r1} and A_{r2} are the known asymmetries of these two detectors, one we can solve Equation 4.34 for $\alpha_1 A_{syst}$

$$\alpha_1 A_{syst} = [(A_1 - A_2) - (A_{r1} - A_{r2})]\frac{\alpha_1}{\alpha_1 - \alpha_2} = \Delta A \frac{\alpha_1}{\alpha_1 - \alpha_2}. \tag{4.35}$$

The two coefficients α_1 and α_2 were estimated by various methods. One of these methods is the ratio of the charge slopes

$$\frac{\alpha_1}{\alpha_2} = \frac{Q_1}{Q_2}. \tag{4.36}$$

This is because most of the beam asymmetries are sensitive to charge. As a cross-check, the higher-order beam systematics in Runs III were estimated using this method as well as the sliced signals analysis. A very good agreement between the two methods was obtained [65]. In conclusion, the higher-order beam systematics were estimated to be at the level of 10 ppb, 15 ppb and 2 ppb for Runs I-III, respectively [65, 66].

Systematic Uncertainties from Beam Spotsize

The spotsize (the helicity-correlated differences in the beam size) was measured by the wire array device. It is defined as $S = \pi\sigma_x\sigma_y$, where σ is the width of the

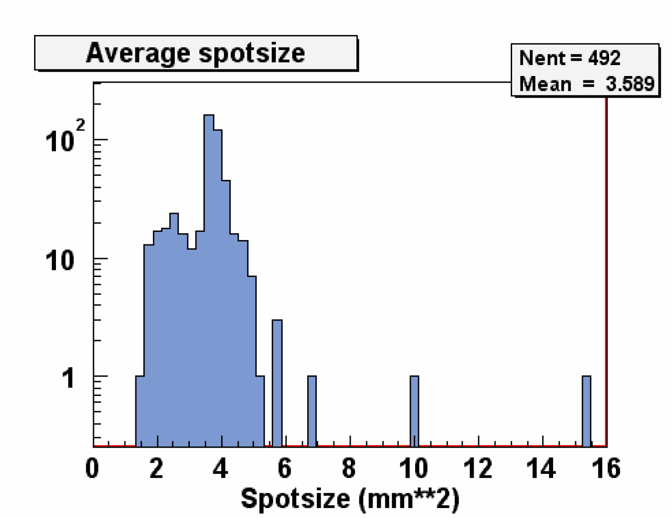

Figure 4.12: A histogram of the average spotsize, S.

beam size in either x or y. A histogram of the average spotsize, S, for each run is shown in Figure 4.12. The systematic uncertainties due to the beam spotsize is given by [67]

$$A_{spot} = \alpha[\pi\sigma_x\langle D_y\rangle + \pi\sigma_y\langle D_x\rangle], \tag{4.37}$$

where α is a correlation factor and $\langle D_x\rangle$ and $\langle D_y\rangle$ are the average x and y spotsize differences. The overall systematic uncertainty due to beam soptsize was found to be 0.05 ± 0.5ppb, -0.8 ± 0.7 ppb, and 0.5 ± 0.7 ppb for Runs I-III, respectively [68]. Because the effect of the beam spotsize is less than one ppb, it was neglected.

Comparing Regression with Dithering

As we mentioned earlier, the beam corrections to the measured asymmetry were calculated in two different methods: regression and dithering. The dithering/regression plays two important roles in the experiment:

1. Reduce the contribution to the width of the asymmetry due to beam noise.

2. Reduce the effect of helicity correlated beam differences on the average asymmetry.

In order to examine the reliability of the dithering/regression corrections, one needs to compute the width of the asymmetry with and without dithering/regression.

In addition, the asymmetry is not expected to vary much between the two methods. Therefore, it is necessary to make a comparison between the asymmetry corrected by regression and the asymmetry corrected by dithering. Although, the final result was computed using the regression corrections, dithering analysis worked as a very important double-check for the regression analysis.

The dithering coils did not work well for a number of runs we, therefore, carried out the dithering analysis on one common data set where both regression and dithering worked very well. The beam corrections for both regression and dithering are summarized in Table 4.6. The systematic uncertainties shown in this table were calculated using the same method that was discussed above. The overall difference between dithering and regression was about 1 ppb. Figure 4.13 shows the Møller asymmetry determined by dithering at the different settings of the half-wave-plate and the energy in Run III. A comparison between those asymmetries corrected by regression and those, corrected by dithering is shown in Figure 4.14.

4.3.2 Corrections from Background Processes

The detector signal S has two components:

$$S = S_M + S_B, \tag{4.38}$$

Beam Corrections (ppb)		
Beam Parameters	**Regression**	**Dithering**
Q	-0.4 ± 0.00	-2.7 ± 0.00
E	22.1 ± 0.58	27.0 ± 0.68
X	-11.5 ± 0.23	-5.4 ± 0.13
Y	-20.8 ± 0.75	-24.9 ± 0.87
θ_x	8.0 ± 0.64	1.7 ± 0.11
θ_x	1.5 ± 0.07	3.3 ± 0.15
Total	-0.1 ± 1.17	-2.3 ± 1.12

Table 4.6: Corrections due to the beam differences calculated by regression and dithering.

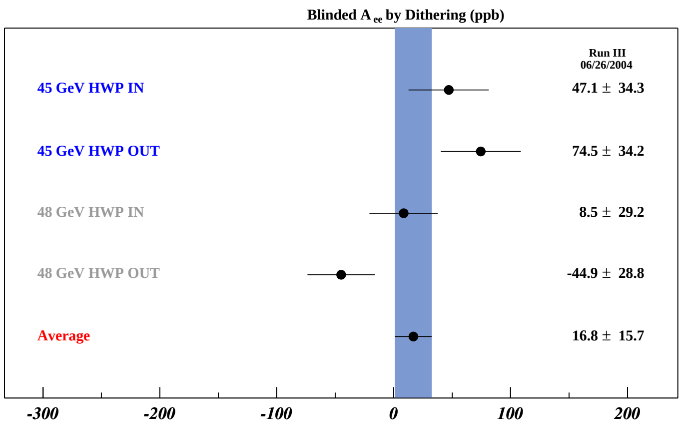

Figure 4.13: Blinded Møller asymmetry determined by dithering at different settings of the HWP and the energy in Run III. The asymmetries have already been corrected for the reversal sign.

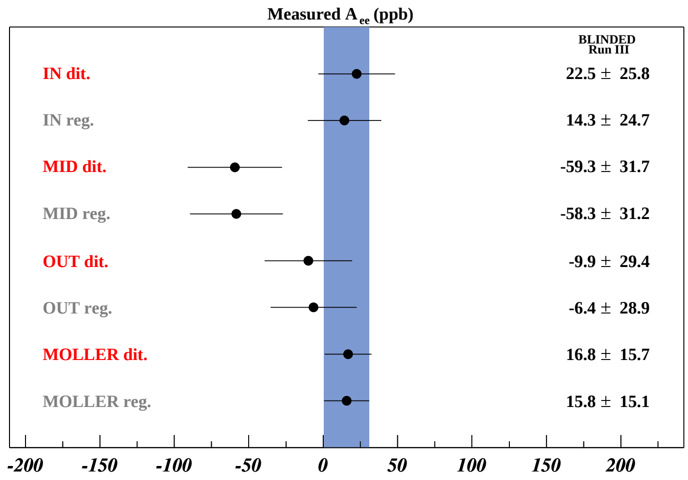

Figure 4.14: The blinded Moller asymmetries using regression and dithering corrections in Run III.

where S_M and S_B are the contributions to the signal due to Møller scattering and background processes, respectively. Therefore, the asymmetry takes the form

$$\begin{aligned} A &= \frac{S^R - S^L}{S^R + S^L}, \\ &= \frac{(S_M^R - S_M^L) + (S_B^R - S_B^L)}{(S_M^R + S_M^L) + (S_B^R - S_B^L)}, \\ &= A_M(1 - f_B) + f_B A_B, \end{aligned} \tag{4.39}$$

where

$$\begin{aligned} A_M &= \frac{S_M^R - S_M^L}{S_M^R + S_M^L}, \quad A_B = \frac{S_B^R - S_B^L}{S_B^R - S_B^L}, \\ f_B &= \frac{1}{1 + \frac{S_M^R + S_M^L}{S_B^R + S_B^L}}. \end{aligned} \tag{4.40}$$

The Møller asymmetry, A_M, can be then given in terms of the measured asymmetry, A, the background asymmetry, A_B, and a factor f_B:

$$A_M = \frac{A - f_B A_B}{1 - f_B}. \tag{4.41}$$

The factor f_B is called a *dilution factor* since it has a value < 1, *i.e.*, it leads to a dilution of (decrease in) the asymmetry A_{PV}. By taking, into consideration, all background processes, we end up with

$$A_{PV} = \frac{A^{meas} - \sum_{bkg} f_{bkg} A^{bkg}}{1 - \sum_{bkg} f_{bkg}} \equiv \frac{A^{meas} - \Delta A}{1 - f}. \tag{4.42}$$

In the following subsections, we will discuss these background processes and their contributions to the Møller asymmetry.

ep Corrections

Corrections due to elastic and inelastic *ep* processes were determined using the data that was collected by the MOTT detector, and by Mont Carlo simulation as well. Figure 4.15 shows the Monte Carlo simulation and a real data scan that was taken by the profile detector. This scan was taken using the *holy* collimator in order to create a clean separation between the Møller and the *ep* scatters.

The parity-violating *ep* asymmetry is given by [69]

$$A_{LR} = \frac{d\sigma_L - d\sigma_R}{d\sigma_L + d\sigma_R} = -\frac{G_F Q^2}{4\sqrt{2}\pi\alpha}[Q_W(p) + F^p(Q^2, \theta)], \tag{4.43}$$

where $Q_W(p)$ [3] is the weak charge of the proton and F^p is a form factor. This asymmetry was found to be -1.43 ± 0.04 ppm at 45 GeV and -1.74 ± 0.06 ppm at 48 GeV. The difference in the asymmetry is due to the fact that $A_{ep} \sim 10^{-4} Q^2$ for elastic and $A_{ep} \sim 10^{-5} Q^2$ for inelastic, and Q^2 itself is significantly different for the

[3] At the tree level, $Q_W(p)$ is given by $Q_W(p) = 1 - 4\sin^2\theta_W$.

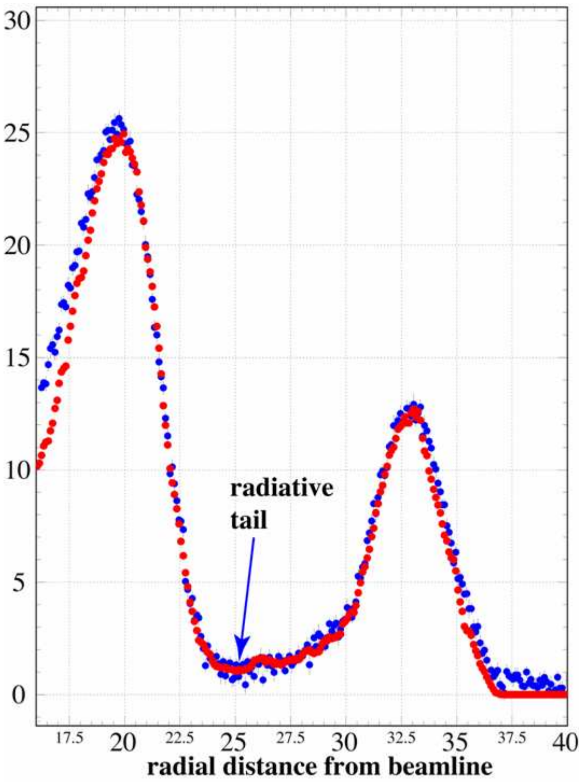

Figure 4.15: The Monte Carlo simulation (*blue*) and a real data scan (*red*) that was taken by the profile detector with the *holy* collimator inserted.

two energy states. This indicates that the Møller asymmetry must be separated by the energy state, so that the different *ep* corrections can be added to each sector. For a detailed description of the procedure for estimating both the elastic and the inelastic *ep* corrections, see Reference [70]. These corrections are summarized in Table 4.7.

Pion Corrections

The effect of the π background in the measured parity-violating asymmetry is given by [55]

$$A_{PV} = \frac{A_{meas} - \frac{\epsilon N_\pi}{N_e} A_\pi}{1 - \frac{\epsilon N_\pi}{N_e}}, \tag{4.44}$$

where A_π is the parity-violating asymmetry, measured by the π detector, N_π and N_e are the pions and electrons rate in the Møller detector, and ϵ is the ratio of the Cherenkov energy deposited by pions over the Cherenkov deposited by electrons in the Møller detector. In Equation 4.44, the term $\frac{\epsilon N_\pi}{N_e} A_\pi$ gives the correction to the experimental asymmetry due to the π background with a dilution factor of $\frac{\epsilon N_\pi}{N_e}$.

The flux ratio $\frac{N_\pi}{N_e}$ and the energy ratio ϵ were estimated via a GEANT simulation. The asymmetry measured by the π detector was found to be 1.35 ± 0.43 ppm, 0.78 ± 0.45 ppm, 0.55 ± 0.37 ppm with dilutions factors of 0.001 ± 0.001, 0.001 ± 0.001, and 0.002 ± 0.002 for Runs I-III, respectively [71]. A reduction of about 40% can be noticed in the measured A_π in Runs II and III. This reduction is due to the *ep* collimator [4], which was installed between Run I and Run II. Therefore, pions from *ep* detector were suppressed, while pions from Møller detector were seen by the pion detector. The overall pion correction is then 1.87 ± 1.54ppb, 1.08 ± 1.03 ppb, and 0.74 ± 0.75 ppb for Runs I-III, respectively.

[4] Also known as the 3CM8 collimator.

	ΔA (ppb)	f				
Elastic ep	**Run I**		**Run II**		**Run III**	
45 GeV	-8 ± 2	0.067 ± 0.006	-7 ± 1	0.055 ± 0.006	-8 ± 2	0.059 ± 0.008
48 GeV	-8 ± 2	0.059 ± 0.007	-7 ± 1	0.052 ± 0.005	-8 ± 1	0.055 ± 0.007
Total Elastic	-8 ± 2	0.064 ± 0.007	-7 ± 1	0.053 ± 0.005	-8 ± 1	0.057 ± 0.008
Inelastic ep						
45 GeV	-25 ± 6	0.011 ± 0.003	-20 ± 5	0.009 ± 0.002	-20 ± 5	0.009 ± 0.003
48 GeV	-26 ± 6	0.010 ± 0.003	-21 ± 6	0.009 ± 0.002	-22 ± 6	0.009 ± 0.002
Total Inelastic	-26 ± 6	0.011 ± 0.03	-21 ± 6	0.009 ± 0.002	-21 ± 6	0.009 ± 0.003
Elastic + Inelastic						
45 GeV	-33 ± 6	0.078 ± 0.007	-28 ± 5	0.064 ± 0.006	-28 ± 6	0.068 ± 0.009
48 GeV	-35 ± 6	0.070 ± 0.007	-29 ± 6	0.061 ± 0.006	-30 ± 6	0.063 ± 0.007
Total ep	-34 ± 6	0.075 ± 0.007	-29 ± 6	0.062 ± 0.006	-29 ± 6	0.066 ± 0.008

Table 4.7: Corrections, ΔA, and dilutions, f, from ep elastic and inelastic processes for Runs I-III.

Neutral Backgrounds

The corrections from neutral backgrounds (photons and neutrons) in the Møller detector and their dilution factors were estimated by auxiliary measurements made during Runs I,II, and III. The results from the analysis [72] of these background studies are summarized in Table 4.8

Luminosity Monitor Asymmetry

As mentioned earlier, the asymmetry measured by the luminosity monitor is expected to be zero. The luminosity asymmetry was calculated using the standard formula of the Møller asymmetry, except that extra cuts were applied to the raw data. These cuts remove any event that was collected when any of the channels of the luminosity monitor was dead. The luminosity monitor measured an asymmetry of -16 ± 15 ppb, -14 ± 12 ppb, and -45 ± 14 ppb in Runs I-III, respectively. The non-zero asymmetry, seen by the luminosity monitor especially in Run III, insure our hypothesis regarding the extra beam parameters, which were measured by the *sliced* beam signals. Figure 4.16 shows the asymmetry measured by the front luminosity monitor at the different settings of the half-wave-plate and the beam energy in Run III.

4.3.3 Beam Polarization

The measured asymmetry is related to the parity violating asymmetry by

$$A_{meas} = P_e \cdot A_{PV}, \tag{4.45}$$

where P_e is the longitudinal polarization of the electron beam. Therefore, an accurate measurement of P_e is required. By using the SLAC polarized electron

	ΔA (ppb)	f				
Source	**Run I**		**Run II**		**Run III**	
High energy photons	3±3	0.004±0.002	3±3	0.004±0.002	3±3	0.004±0.002
Synchrotron photons	0±5	0.002±0.001	0±2	0.002±0.001	0±9	0.002±0.002
Neutrons	−5±3	0.003±0.001	0±0	0.000±0.000	0±0	0.000±0.000

Table 4.8: Corrections, ΔA, and dilutions, f from neutral background processes for Runs I-III.

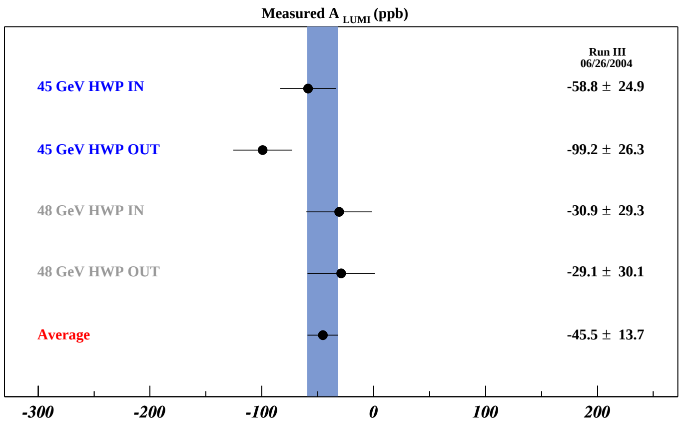

Figure 4.16: Luminosity monitor asymmetry at different settings of the HWP and the energy in Run III. The asymmetries have already been corrected for the reversal sign.

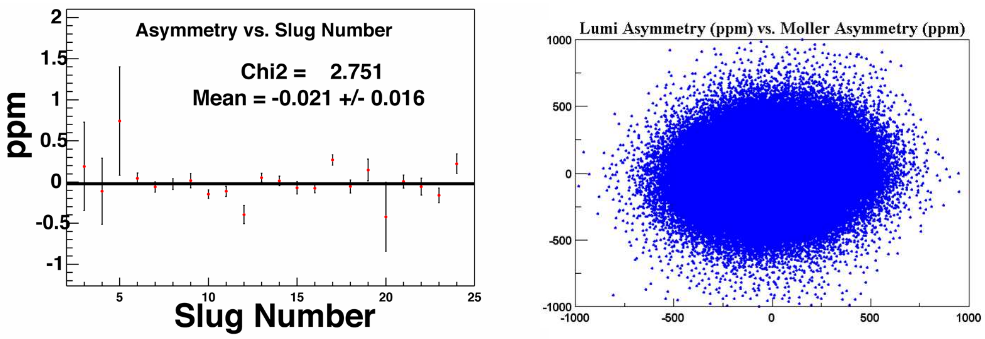

Figure 4.17: The left-right asymmetry as a function of data samples measured by the Luminosity monitor in Run I (*left*). The Møller asymmetry against the Luminosity monitor (*right*), which shows that there is no indication for *target boiling*.

beam scattering off a longitudinally polarized iron foil target, we computed the left-right asymmetry measured by the polarimeter detector [73]

$$\begin{aligned} A_{LR}^{polarimeter} &= \frac{d\sigma_{LL} - d\sigma_{RL}}{d\sigma_{LL} + d\sigma_{RL}} \\ &= P_{e^-}^{beam} \times P_{e^-}^{foil} \times \frac{(7+\cos^2\theta_{CM})\sin^2\theta_{CM}}{(3+\cos^2\theta_{CM})^2}, \end{aligned} \tag{4.46}$$

where $P_{e^-}^{beam}$ is the longitudinal beam polarization, $P_{e^-}^{target}$ is the longitudinal iron foil polarization , and θ_{CM} is the center of mass scattering angle.

For $\theta_{CM} = 90^o$ and $P_{e^-}^{foil} \sim 8\%$, the left-right asymmetry, measured by the polarimeter detector $A_{LR}^{polarimeter}$, is around 0.05. This asymmetry in turn had to be corrected from background scatters, which come mainly from *ep* electrons and low-energy photons. This background was estimated by GEANT simulation to be $(8 \pm 3)\%$ of the asymmetry measured by the polarimeter detector.

The overall electron beam polarization was 0.85 ± 0.05 for Run I, 0.84 ± 0.05 for Run II, and 0.85 ± 0.04 for Run III.

4.3.4 Linearity of the Møller Detector

The measured asymmetry is related to the parity-violating asymmetry by [75]

$$A_{meas} = \epsilon \cdot A_{PV}, \tag{4.47}$$

where ϵ is the detector linearity. In fact, ϵ directly depends on the flux F seen by the detector

$$\epsilon = 1 - \beta F + O(\beta F)^2, \tag{4.48}$$

where β is a constant. At large input signals, $\beta F \gg 1$, which means that the detector response is non-linear. A good method to measure ϵ is to compare the detector asymmetries obtained at different flux conditions. A low flux was obtained by covering the Møller PMTs with aluminum foil with half-inch hole punch through it. To get a higher flux, the hole diameter was increased to be one-inch instead of half-inch or the PMTs remained uncovered. We then estimated ϵ from

$$\frac{A_{meas}^{high}}{A_{meas}^{low}} = \frac{1-\beta F^{high}}{1-\beta F^{low}}. \tag{4.49}$$

assuming that $\beta F \gg 1$ *i.e.* the detector response is very linear at low flux [74]. Results from this analysis show that the linearity of the Møller detector is 0.99 ± 0.01 in Runs I-III.

4.4 A_{PV}

As mentioned earlier, in order to calculate the experimental asymmetry, the data must be separated by energy state, so that the different *ep* corrections can be added to each set. For one energy state, E, the physics asymmetry is given by:

$$A_E = \frac{1}{n}\frac{A_E^{meas} - \Delta A_E}{1-f_E}. \tag{4.50}$$

where $\Delta A_E \pm \delta(\Delta A_E)$ and $f_E \pm \delta f_E$ are the linear sums of all corrections and dilutions for various background sources, respectively. Their errors are the quadrature sum of the individual errors on the corrections or the dilutions;

$$\delta(\Delta A_E) = \sqrt{\sum_i \delta(\Delta A_E^i)^2}, \tag{4.51}$$

$$\delta f_E = \sqrt{\sum_i \delta(f_E^i)^2}. \tag{4.52}$$

$n \pm \delta n$ is a normalization factor, which is the direct product of the detector linearity, ϵ, and the beam polarization, P. The detector linearity and the beam polarization are the same for the two energy states. Therefore, the error on the normatization factor δn is calculated as

$$\delta n = n\sqrt{(\frac{\delta P}{P})^2 + (\frac{\delta\epsilon}{\epsilon})^2}. \tag{4.53}$$

All corrections, dilutions, and normalizations are listed in Table 4.9.

The statistical and systematic errors on A_E are obtained by

$$\begin{aligned} \delta A_E(stat) &= \alpha_E \delta A_E^{reg}, & (4.54) \\ \delta A_E(syst) &= \sqrt{\alpha_E^2 \delta(\Delta A_E)^2 + \beta_E^2 \delta f_E^2 + \gamma_E^2 \delta n^2}, & (4.55) \end{aligned}$$

where

$$\begin{aligned} \alpha_E &= \frac{1}{n(1-f_E)}, & (4.56) \\ \beta_E &= \frac{A_E}{1-f_E}, & (4.57) \\ \gamma_E &= \frac{A_E}{n}. & (4.58) \end{aligned}$$

To get the final physics asymmetry A_{PV}, we combine the asymmetries A_E due to the two energy states, using their statistical weights $\delta A_E(stat)$

$$A_{PV} = \sum_E W_E A_E, \tag{4.59}$$

where

$$W_E = \frac{\frac{1}{\delta A_E^2}}{\sum_E \frac{1}{\delta A_E^2}}. \tag{4.60}$$

The statistical and systematic errors on A_{PV} are obtained by

$$\begin{aligned} \delta A_{PV}(stat) &= \frac{1}{\sqrt{\sum_E \frac{1}{\delta A_E^2}}}, & (4.61) \\ \delta A_{PV}(syst) &= \sqrt{(\sum_E \alpha'_E \delta(\Delta A_E))^2 + (\sum_E \beta'_E \delta f_E)^2 + (\sum_E \gamma'_E \delta n)^2}, & (4.62) \end{aligned}$$

	$\Delta A \pm \delta(\Delta A)$ (ppb)	$f \pm \delta f$				
Source	**Run I**		**Run II**		**Run III**	
First-order beam	0±3	-	0±2	-	0±2	-
Higher-order systematics	0±10	-	0±15	-	0±2	-
Transverse polarization	−8±3	-	−5±3	-	−5±2	-
Elastic *ep*	−8±2	0.064±0.007	−7±1	0.055±0.006	−7±1	0.057±0.008
Inelastic *ep*	−26±6	0.011±0.003	−20±5	0.009±0.002	−31±10	0.009±0.003
High-energy photons	3±3	0.004±0.002	3±3	0.004±0.002	3±3	0.004±0.002
Synchrotron photons	0±5	0.002±0.001	0±2	0.002±0.001	0±9	0.002±0.002
Neutrons	−5±3	0.003±0.001	0±0	0.000±0.000	0±0	0.000±0.000
Pions	1±1	0.001±0.001	1±1	0.001±0.001	0±5	0.002±0.002
Total Background	−43±14	0.090±0.009	−30±17	0.075±0.008	−28±8	0.077±0.009

	Normilzation		
Source	**Run I**	**Run II**	**Run III**
Polarization	0.85±0.05	0.84±0.05	0.91±0.05
Detector Linearity	0.99±0.01	0.99±0.01	0.99±0.01
Total Normalization	0.84±0.05	0.83±0.05	0.90±0.05

Table 4.9: All corrections, $\Delta A \pm \delta(\Delta A)$, and dilutions, $f \pm \delta f$, for Runs I-III.

where

$$\alpha'_E = W_E \alpha_E,\ \beta'_E = W_E \beta_E,\ \gamma'_E = W_E \gamma_E. \tag{4.63}$$

Using these equations, the measured parity-violating asymmetry in the Møller scattering was found to be

Run I:	-175 ± 30 (stat.) ± 20 (syst.) ppb
Run II:	-144 ± 28 (stat.) ± 23 (syst.) ppb
Run III:	-107 ± 18 (stat.) ± 20 (syst.) ppb
Run I-III combined:	-128 ± 14 (stat.) ± 12 (syst.) ppb

A plot of the parity-violating asymmetry for each slug for Runs I, II, and III is given in figure 4.18. The sign flips, due to the energy state and half-wave-plate state, are not included in order to illustrate that the measured asymmetry has the expected sign flips with respect to energy and half-wave-plate configuration. A comparison of the parity-violating asymmetry between the three Runs and their average is shown in Figure 4.19.

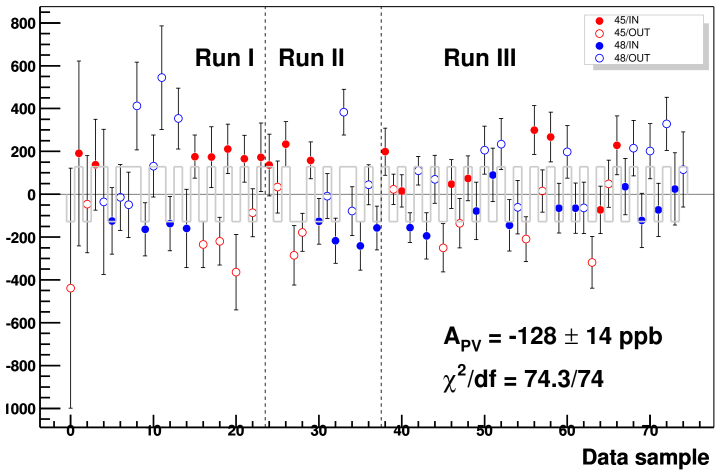

Figure 4.18: The parity-violating asymmetry for each slug in Runs I-III. The data has not corrected for asymmetry sign flips and the gray solid line represents the grand average with the expected asymmetry sign for each sign flip configuration. The uncertainty shown is only the statistical uncertainty.

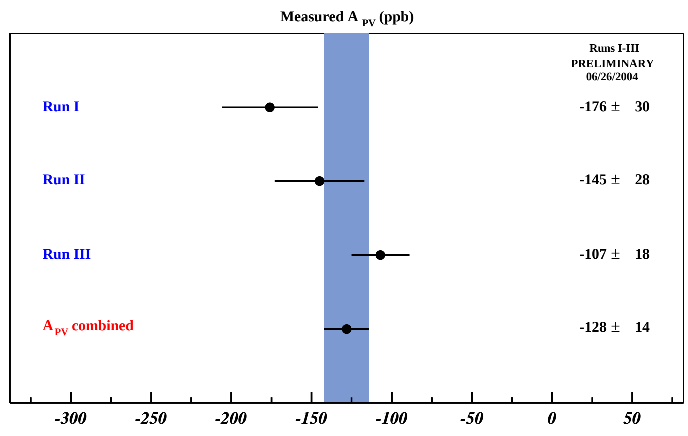

Figure 4.19: A comparison of the parity-violating asymmetry between Runs I-III and their average. The uncertainty shown is only the statistical uncertainty.

Chapter 5

Dithering Analysis

The cross-section is assumed to be sensitive to six independent beam parameters: charge, energy, 2 position coordinates, and 2 angle coordinates, namely: $Q, E, x, y, \theta_x, \theta_y$. The basic idea is to monitor the helicity-correlated differences in these parameters using two kind of devices, toroids and beam position monitors (BPMs), then evaluate the sensitivity of the cross-section to the beam motions as seen by these BPMs. From this information we should be able to evaluate the contribution to the measured raw asymmetry due to the helicity-correlated systematics differences in the position and the angle of the the electron beam.

5.1 Mathematical Formulation

The following is a mathematical formulation of the problem. From Equation 4.4, considering one PMT only, one has

$$A^{beam} = \frac{\partial A^{meas}}{\partial M_i} \Delta M_i \tag{5.1}$$

where $\partial A^{meas}/\partial M_i$ are the first-order correction coefficients, called *the dithering* *slopes* and ΔM_i are the helicity-correlated differences in the BPM i. We will drop the suffix "meas" in A_{meas} for simplicity.

Our goal is to find these slopes. This is achieved by perturbing steering coils in the accelerator C_j and then measuring the response of the BPMs and the cross-section to these perturbations. The partial derivatives that are being measured by perturbing the coils are

$$\frac{\partial A}{\partial C_j}, \frac{\partial M_i}{\partial C_j}, \tag{5.2}$$

which are called *the detector signal slopes* and *the beam parameter slopes* respectively.

The required partial derivatives $\partial A / \partial M_i$ can be then computed by solving the matrix equation:

$$\frac{\partial A}{\partial C_j} = \sum_i \frac{\partial A}{\partial M_i} \frac{\partial M_i}{\partial C_j}, \tag{5.3}$$

where j here is the number of coils. To solve Equation 5.3, we perform a standard χ^2 minimization with respect to $\frac{\partial A}{\partial M_i}$ where [77]

$$\chi^2 = \sum_{j=1}^{coils} \{ \frac{\partial A}{\partial C_j} - \sum_{i=1}^{5} \frac{\partial A}{\partial M_i} \frac{\partial M_i}{\partial C_j} \}^2. \tag{5.4}$$

Now let us impose the minimization condition:

$$\frac{\partial \chi^2}{\partial A / \partial M_i} = 0. \tag{5.5}$$

We get from Equation 5.3 and Equation 5.4

$$S = AM^{-1}, \tag{5.6}$$

where

$$S_i = \frac{\partial A}{\partial M_i}, \qquad i = 1, \ldots, 6, \tag{5.7}$$

$$A_k = \sum_{j=1}^{coils} \frac{\partial A}{\partial C_j} \frac{\partial M_k}{\partial C_j}, \qquad k = 1, \ldots, 6, \tag{5.8}$$

$$M_{ik} = \sum_{j=1}^{coils} \frac{\partial M_i}{\partial C_j} \frac{\partial M_k}{\partial C_j}, \qquad i, k = 1, \ldots, 6. \tag{5.9}$$

Note that the elements of the two matrices A and M can be easily computed, since they are given by the measured partial derivatives $\frac{\partial A}{\partial C_j}$ and $\frac{\partial M_i}{\partial C_j}$. Therefore, we can compute the required coefficients, which are the elements of the matrix S, once we invert the matrix M.

We also note that the dimensionality of the problem, which is defined by the dimension of the matrix M, is independent of the number of coils used. In reality, we used all working coils to perturb the position and the angle of the beam. However, we choose one set of four of coils to calculate the matrix elements M_{ik} and perform the analysis, which was enough for the precision of our measurements.

5.2 Data Analysis

Corrections to the measured asymmetry due to beam asymmetries were calculated using the dithering slopes as well as regression slopes as we discussed in Chapter 4. This was the most important gaol, since this test provided a crosscheck for the Møller asymmetry analysis. In the following subsections, we will view the other aspects of the dithering analysis.

5.2.1 Phase Angle of Dipole Asymmetry

Dithering slopes are very sensitive to the dipole asymmetries (Figure 5.1). In fact, they were used determine the phase angles which in turn determine the actual orientation of the detector. It was very important to determine those angles since they were used to calculate the azimuthal contribution to the asymmetry. In order to calculate these phases, we define the weighted average of the dithering slopes, R, for a particular beam parameter as follow

$$R = \sum_{k=1}^{N} w^k S_k, \tag{5.10}$$

where N is the number of channels in one of the rings of the Møller detector, w_k is the weight for a channel k, and S_k is the dithering slope for the channel k and for the beam parameter under consideration. We then calculated three quantities:

$$w^k = \begin{cases} \frac{2}{N} \\ \frac{2}{N}\ sin\phi^k \\ \frac{2}{N}\ cos\phi^k \end{cases} \tag{5.11}$$

where

$$\phi^k = \frac{2\pi i}{N} + \delta. \tag{5.12}$$

These three quantities give three different states, namely: Monopole (R_o), X-Dipole (R_X), and Y-Dipole (R_Y). Here δ is the phase angle and can be expressed as:

$$\delta = tan^{-1}(\frac{R_Y}{R_X}). \tag{5.13}$$

The above calculations show that the phase angles take the values:

$$\delta = \begin{cases} 137^o \quad IN \\ -65^o \quad MID \\ 131^o \quad OUT \end{cases} \tag{5.14}$$

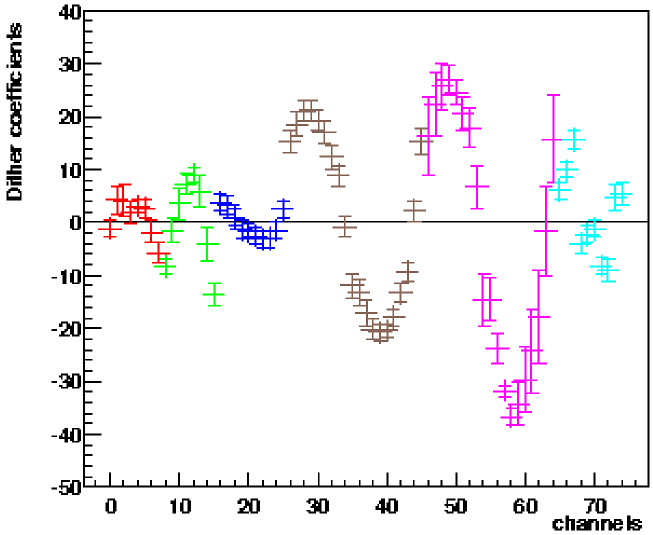

Figure 5.1: Dithering slopes ($\partial A/\partial y$) as a function of ϕ for each detector. The detectors in this graph go in the order: FLUMI, BLUMI, IN, MID, OUT, and EP.

5.2.2 Beam Sensitivity

We used the dithering slopes to study the sensitivity of the monopole and the dipole asymmetry to the beam asymmetries. This was done by examining the dithering slopes against time as shown in Figure 5.2, where one can tell that the Y-Dipole is sensitive to the y-position of the beam while the Monopole and the X-Dipole are not.

This particular test lead to a new fact that we learned about our experiment. We first noticed some oscillatory behavior in the dithering slopes for some detectors and not others. For example, Figure 5.3 shows this behavior in the Luminosity Monitor. An excellent candidate for such behavior was the temperature of the environment, which might affect the spectrometer tunning. In addition, the temperature might affect the length of the cable of the BPM that transfers the signal.

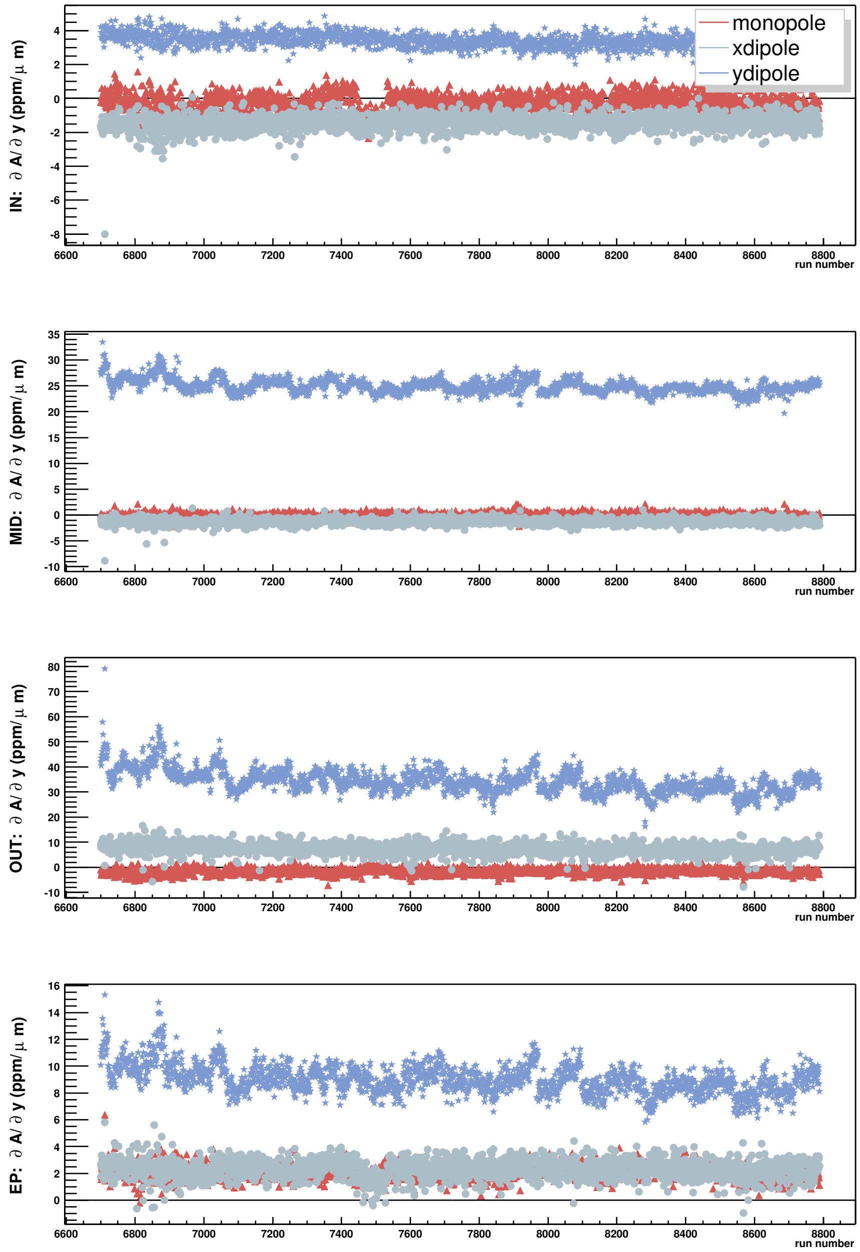

Figure 5.2: Dithering slopes ($\partial A/\partial y$) as a function of time at monopole and dipole for the Møller and ep detectors.

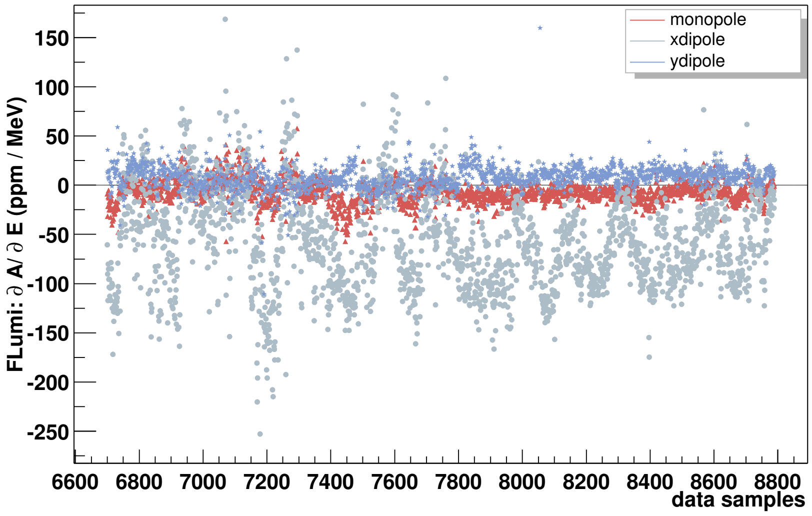

Figure 5.3: Dithering slopes ($\partial A/\partial E$) as a function of time at monopole and dipole for the Luminosity Monitor.

To investigate that, we plotted the dithering slopes vs time of day as shown in Figure 5.4. We found out that all beam parameters experience significant fluctuations due to the temperature of the environment. For example, the beam energy shows a fluctuation of 50 ppm/μm.

5.2.3 Correlation Between Beam Parameters

Correlation between beam parameters were examined by the dithering analysis. In fact, the mount of correlation between two beam parameters p_1 and p_2

$$corr(p_1, p_2) = \frac{(p_1 - \overline{p_1})(p_2 - \overline{p_2})}{\sqrt{(p_1 - \overline{p_1})^2 (p_2 - \overline{p_2})^2}}, \quad p_i = \partial A/\partial M_i \tag{5.15}$$

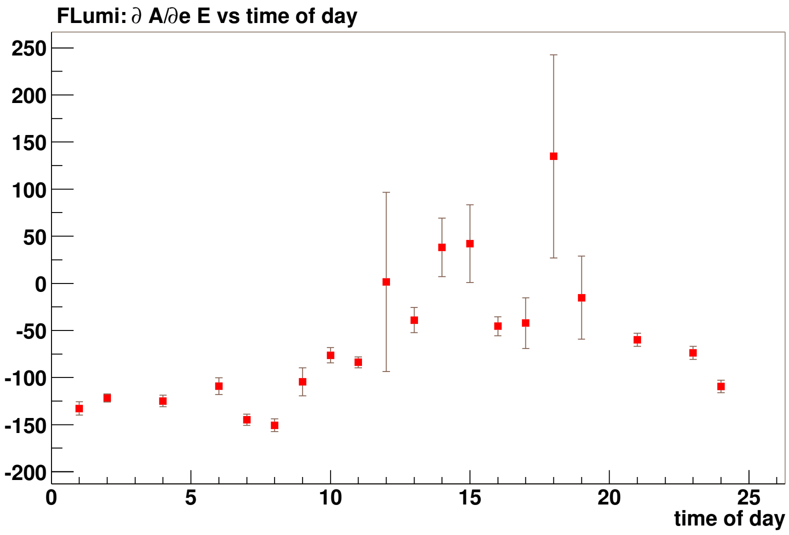

Figure 5.4: Dithering slopes ($\partial A/\partial E$) as a function of time of day for the Luminosity Monitor.

was calculated for each detector using the dithering slopes. These values give a symmetric correlation matrix. For the MID ring in Run I, for instance, the matrix took the form

	Q	E	x	y	θ_x	θ_y
Q	100%	33%	−9%	−7%	14%	−4%
E		100%	−32%	−22%	33%	−36%
x			100%	64%	39%	62%
Y				100%	46%	42%
θ_x					1.00%	0%
θ_y						100%

which tells us that there is a weak correlation appears between the beam position x and y while there is no correlation between θ_x and θ_y. The charge is weakly correlated to other beam parameters as well. The energy is not strongly correlated to other beam parameters either. This is shown in Figure 5.5 in which we plotted $\partial A/\partial M_i$ vs $\partial A/\partial M_j$ for some beam parameters. The non-observed correlation between the beam parameters indicates that the regression method can be safely used in the asymmetry analysis.

5.2.4 Weights

As we mentioned in the previous chapter, we tried various schemes of weight to calculate the overall detector asymmetry. Some of these schemes minimize the statistical width of the asymmetry, while other schemes take care of systematics errors such as the transverse (*dipole*) contribution. Dithering slopes helped to examine the different effects of these schemes. For example, we considered the two weighting schemes: *MollerE* and *MollerDipoleRing*. The first scheme gives a standard

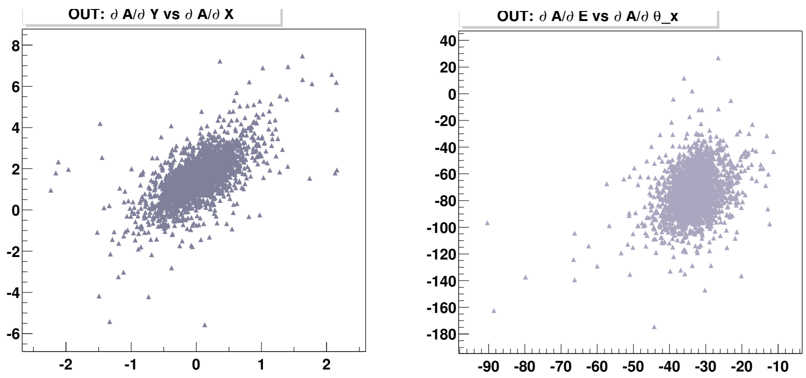

Figure 5.5: Shown are the weak correlation between the beam positions x and y (*left*) and the zero correlation between the energy and θ_x (*right*).

statistical minimization, while the second one minimizes the dipole contribution. A comparison between the two schemes shows a significant disagreement in the OUT ring (roughly 200 ppm/μm) while it shows an excellent agreement in IN and MID rings (Figure 5.6).

5.2.5 *Memo* Output

As mentioned earlier dithering/regression correction reduces the contribution to the width of the asymmetry due to beam noise. In order to study the noise at the run level, outputs for each run (similar to what is shown in Figure 5.7) provided useful information on how dithering/regression correction reduced the noise, especially for the sensitive rings. These outputs are known as the *Memo* outputs.

These outputs show two kinds of information, monitor and detector information. In the monitor section, the *memo* output included information about the BPM electronic noise, as well as the correlation between the beam parameters. For the detectors sector, the calculated dithering slopes were summarized. Also

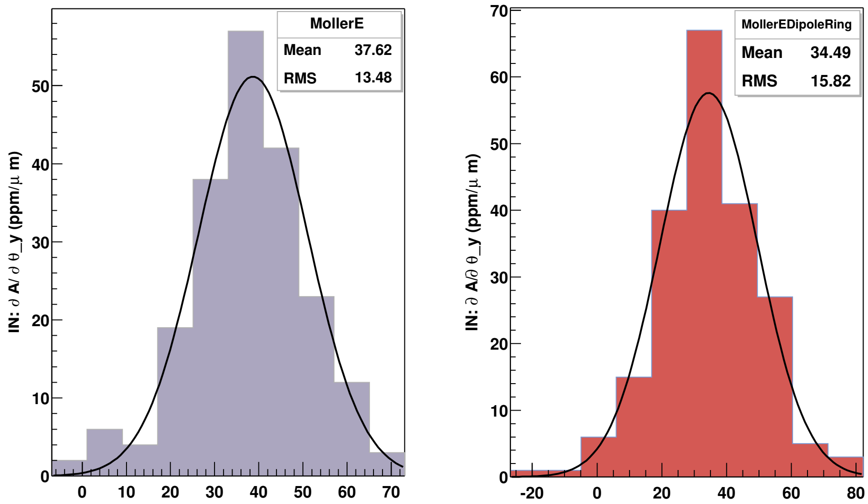

Figure 5.6: A comparison between two schemes of weights *MollerE* and *MollerDipoleRing*, using the dithering slopes.

the width of the raw and corrected asymmetry was provided.

5.3 Summary

In conclusion, dithering analysis played a very important role in the data analysis of E158. The dithering analysis really increased our knowledge about the systematics in the experiment. We obtained very useful information about the relationship between the beam and the detector that can be used not only in E158 but in future experiments as well.

Monitor Quantities

(1)	(2)	(3)	(4)	(5)	(6)	(7)	(8)	(9)	(10)	(11)
					Q	E	x	y	dx	dy
Q	3725.2	37.2	0.0		1.00	-0.78	0.90	0.72	-0.84	-0.84
E	23.6	6.6	0.0		-0.78	1.00	-0.81	-0.73	0.82	0.84
x	152.8	23.3	0.0	-2.65	0.90	-0.81	1.00	0.81	-0.94	-0.92
y	102.7	4.3	0.0	0.00	0.72	-0.73	0.81	1.00	-0.95	-0.84
dx	4.6	0.6	3729.6	0.05	-0.84	0.82	-0.94	-0.95	1.00	0.95
dy	1.2	0.2	23.6	0.03	-0.84	0.84	-0.92	-0.84	0.95	1.00

Detector Quantities

(12)	(13)	(14)	(15)	(16)	(17)	(18)	(19)	(20)	(21)
	Q	E	x	y	dx	dy	reg	dit	raw
moller	-0.02	-14.6	0.7	-0.3	-1.0	1.5	184	191	479
ep	0.07	-18.6	-3.4	-0.9	0.6	0.3	1635	1679	1652
in	-0.04	-14.1	1.2	-0.3	-1.6	1.1	290	312	574
inx	-0.03	1.8	0.3	-0.8	-4.8	-0.0	363	369	798
iny	-0.00	-2.8	-0.8	-0.7	-0.1	4.3	336	341	472
mid	-0.03	-19.7	1.2	-0.3	-1.8	1.3	233	250	750
midx	-0.02	8.6	-16.3	-1.1	-3.3	-0.5	299	347	2343
midy	0.01	-1.5	-0.9	13.7	-0.1	3.9	267	278	1267
out	0.03	-3.4	0.0	-0.3	0.6	2.6	320	341	372
outx	0.10	-10.4	-19.3	3.1	9.8	-0.7	440	484	3975
outy	-0.03	-1.1	2.0	22.3	-2.2	-9.6	410	454	3299
blumi	0.06	-7.9	-5.8	-0.4	1.9	-1.4	158	252	783
blumix	0.26	-36.0	4.5	1.4	15.0	1.5	375	620	1086
blumiy	-0.01	8.1	1.1	0.3	0.5	-14.1	374	551	797
flumi	-0.03	-1.7	-4.7	-0.5	0.8	-0.4	284	313	941
flumix	0.35	-51.6	12.2	2.3	20.1	1.3	514	894	1677
flumiy	-0.01	9.5	0.5	-5.6	0.8	-19.4	526	786	887

Key:

(1) Monitor
(2) Delta M (difference width)
(3) delta M (double difference width)
(4) Monitors resolution
(5) Dispersion = position & angle /energy
(6)..(11) Beam Correlation Matrix
(12) Pattern
(13)..(18) dAsy/dM
(19) regressed RMS
(20) dither RMS
(21) raw RMS

N.B. Angles are in microns, not microradians!

Figure 5.7: A sample of the *Memo* Output in Run III

Chapter 6

Weak Mixing Angle and Other Implications

6.1 Calculation of $\sin^2\theta_W$

Our measurement of A_{PV} is related to the electron weak charge, Q_W^e, by

$$A_{PV} = A_{RL} = \mathcal{A}(Q^2, y)Q_W^e, \tag{6.1}$$

where

$$\mathcal{A}(Q^2, y) = -\frac{G_F Q^2}{4\sqrt{2}\pi\alpha}\frac{1-y}{1+y^4+(1-y)^4}\mathcal{F}_b. \tag{6.2}$$

is known as the analyzing power. $\mathcal{A}(Q^2, y)$ depends on kinematics and the experimental geometry and was determined from a Monte Carlo simulation. The factor $\mathcal{F}_b = 1.016 \pm 0.005$ accounts for hard initial- and final-state radiation [78] (Figure 6.1). We may then write,

$$Q_W^e = \frac{A_{PV}}{\mathcal{A}(Q^2, y)}. \tag{6.3}$$

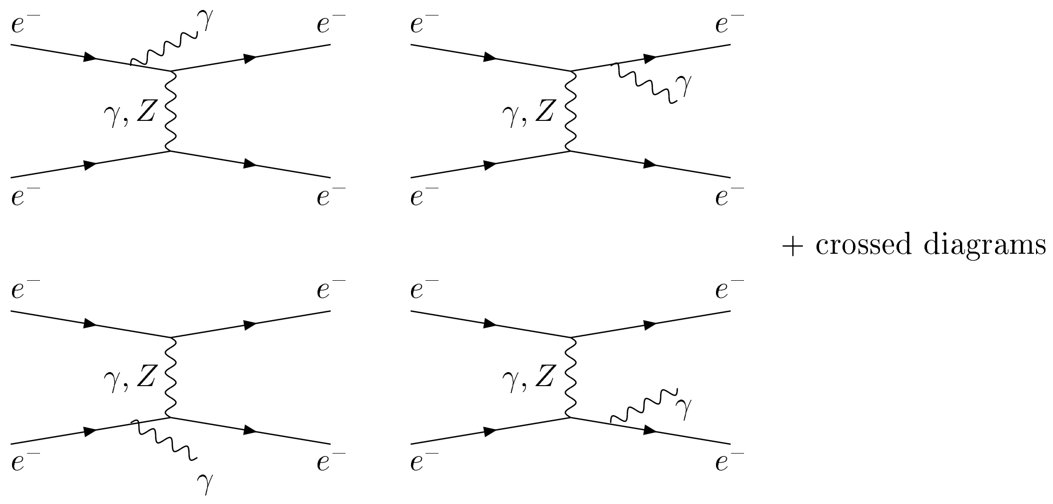

Figure 6.1: Bremsstrahlung corrections to the analyzing power.

The average values of the kinematics variables were $Q^2 = 0.025$ (GeV/c)^2 and $y = Q^2/s \simeq 0.57$. To take into account the LO corrections, we compute G_F form muon lifetime using one-loop formula [79]

$$G_\mu = 1.166 \times 10^{-5} GeV^{-2}, \tag{6.4}$$

and employ $\alpha(m_Z)$

$$\alpha(m_Z) = 127.9 \pm 0.1, \tag{6.5}$$

defined by modified minimal subtraction scheme ($\overline{MS}$) at $\mu = m_Z$, which reduces the NLO effects. Calculations of $\mathcal{A}$ showed that $\mathcal{A} = 3.28 \pm 0.06$ ppm in Run I, $\mathcal{A} = 3.34 \pm 0.05$ ppm in Run II, and $\mathcal{A} = 3.28 \pm 0.05$ ppm in Run III.

As shown Table 6.1, the weak charge of the electron Q^e_W was found to be

$$Q^e_W = -0.0388 \pm 0.0042 \text{ (stat.)} \pm 0.0040 \text{ (syst.)}, \tag{6.6}$$

which is consistent with the Standard Model expectations [80] of -0.046 ± 0.002.

	Q_W^e	Stat. Error	Syst. Error	$\sin^2\theta_{W_{\overline{MS}}}$	Stat. Error	Syst. Error
Run I	-0.0535	0.0092	0.0062	0.2292	0.0024	0.0016
Run II	-0.0433	0.0085	0.0069	0.2318	0.0022	0.0018
Run III	-0.0326	0.0055	0.0035	0.2346	0.0014	0.0009
Average	-0.0388	0.0042	0.0040	0.2330	0.0011	0.0010

Table 6.1: The E158 result for the weak charge for the electron. The first error is the statistical error while the second error is the systematic error.

In the $\overline{MS}$ scheme, $\sin^2\theta_{W_{\overline{MS}}}$ yields:

$$\sin^2\theta_{W_{\overline{MS}}} = 0.2330 \pm 0.0011\ (\text{stat.}) \pm 0.0010\ (\text{syst.}), \tag{6.7}$$

which gives a Standard Model pull of 1.2σ. This result, together with other experimental measurements, are presented in Figure 6.2.

In the effective scheme:

$$\sin^2\theta_W^{eff} = 0.2403 \pm 0.0010\ (\text{stat.}) \pm 0.0009\ (\text{syst.}) \tag{6.8}$$

which gives a significance of 6.5σ. This result is the most precise measurement of $\sin^2\theta_W$ at low Q^2. The result is plotted, together with a theoretical prediction from Czarnecki and Marciano, in Figure 6.3.

6.2 E158 Result and Physics Beyond the Standard Model

As we discussed earlier, the E158 result for the weak mixing angle can be used to set limits on certain physics theories beyond the Standard Model. As an example

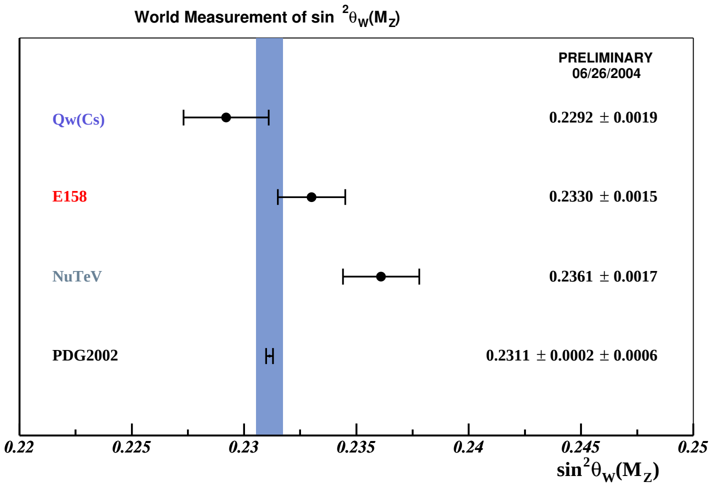

Figure 6.2: Summary of Weak Mixing Angle measurements at the Z^o pole.

of the sensitivity of the measurement to physics beyond the Standard Model, a limit can be set on the mass of the extra Z' boson in the SO(10) Model. The sensitivity is given by (Equation 1.96):

$$\frac{A_{PV}^{meas}}{A_{PV}^{SM}} = \frac{1 - 4\sin^2\theta_W^{meas}}{1 - 4\sin^2\theta_W^{SM}} = 1 + 7\frac{m_Z^2}{m_{Z'}^2}, \tag{6.9}$$

i.e.

$$m_{Z'}^2 = \frac{7m_Z^2(\frac{1}{4} - \sin^2\theta_W^{SM})}{\sin^2\theta_W^{SM} - \sin^2\theta_W^{meas}}. \tag{6.10}$$

By solving this equation, a limit of ~ 0.9 TeV can be set on the mass of Z'.

Another example of the sensitivity of the E158 result to physics beyond the Standard Model is the limit that can be set on the compositness scale Λ_{ee} for contact interactions among electrons. The sensitivity is given by (Equation 1.99):

$$\sin^2\theta_W^{meas} - \sin^2\theta_W^{SM} = \pm\frac{\pi}{G_F\sqrt{2}}\frac{\eta_{RR} + \eta_{LL}}{\Lambda_{ee}^{\pm}}, \tag{6.11}$$

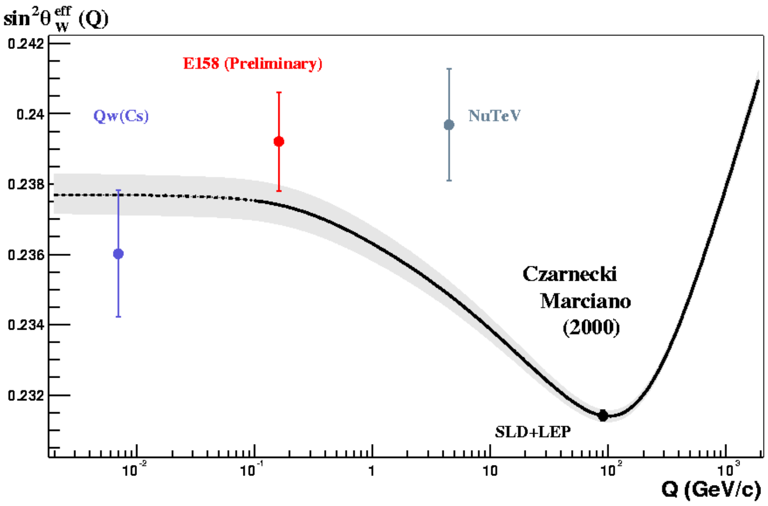

Figure 6.3: Measurement of $\sin^2\theta_W^{eff}$ as a function of momentum transfer Q. The solid line and the dotted line are the theoretical prediction at high and low Q, respectively

where $\eta_{RR} = \eta_{LL} = \pm 1$. At the 95% confidence level, this equation yields $\Lambda_{ee}^{+} \geq 6.4$ TEV and $\Lambda_{ee}^{-} \geq 13.9$ TeV for a positive and negative deviations from the Standard Model, respectively. And if the this four-electron interaction is mediated by a doubley-charged Higgs boson, Δ^{++}, a limit on the mass of this Higgs can be set to be:

$$\frac{g_{ee\Delta}^2}{m_\Delta^2} \simeq \frac{4\pi}{\Lambda_{ee}^2} = 0.2\ TeV, \tag{6.12}$$

using the upper limit of Λ_{ee}.

Chapter 7

Azimuthal Asymmetries in Transversely Polarized Scattering

In addition to the parity-violating asymmetry, A_{PV}, a nonzero azimuthal asymmetry A_T can be generated. This azimuthal asymmetry is governed by QED interactions alone. E158 measured such azimuthal asymmetry in single-spin, transversely polarized Møller scattering. In fact, a fraction of the running was carried out with transverse polarized electron beam in order to measure this azimuthal asymmetry, while most of the data was taken with longitudenal polarized electron beam in order to acheive our precise measurement of the parity-violating asymmetry, A_{PV}. Moreover, the longitudinally polarized beam, that was used to measure A_{PV}, was found to be $\sim 88\%$ polarized. This means that a correction to A_{PV}, due to a small non-zero transversely polarized beam, had to be made.

7.1 Theoretical Motivation

The azimuthal asymmetry, $A_T(\phi)$, for single-spin transversely polarized Møller scattering was calculated up to the leading one-loop order by Barut and Fronsdal in 1960 [81], and again by DeRaad and Ng in 1975 [82]. In 2004, calculations at the two-loop order were performed by Schreiber and Dixor [83].

The azimuthal asymmetry is governed by an operator of the form $\mathbf{S} \cdot (\mathbf{K} \times \mathbf{K}')$, where $\mathbf{S}$ is a spin and $\mathbf{K}$ and $\mathbf{K}'$ are two momenta for two different particles. This asymmetry arises at one-loop order from the interference between the tree diagrams and the box diagrams and it takes the form [83]

$$A_T(\phi) \equiv \alpha_T \sin\phi, \tag{7.1}$$

where ϕ is the azimuthal angle of the scattered electron around the beam direction, measured from the direction of the transverse polarization. If the central-of-mass energy is much larger than the electron mass $\sqrt{s} \gg m_e$, the asymmetry coefficient α_T at the leading-order takes the form

$$\alpha_T^{LO} = \alpha \frac{m_e}{\sqrt{s}} f(\theta), \tag{7.2}$$

where α is the fine structure constant, θ is the scattering angle in the center of mass frame, and $f(\theta)$ is given by:

$$f(\theta) = \frac{s\left\{3s\left(t(u-s)ln(-t/s) - u(t-s)ln(-u/s)\right) - 2(t-u)tu\right\}}{4(t^2+tu+u^2)^2} \cdot \sin\theta, \tag{7.3}$$

where

$$s = 2m_e E, \quad u = -\frac{s}{2}(1+\cos\theta), \quad t = -\frac{s}{2}(1-\cos\theta). \tag{7.4}$$

The function $f(\theta)$ is odd under $\theta \to \theta - \pi$. Therefore, the the asymmetry in ϕ can be completely canceled if there is a high acceptance in θ. Because of the θ

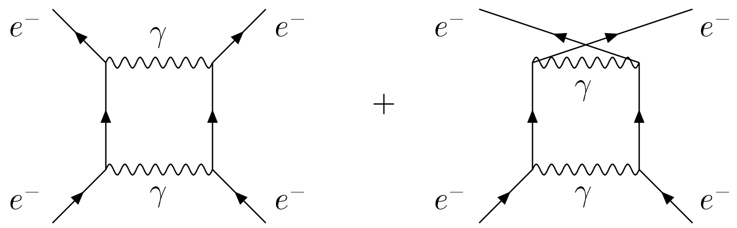

Figure 7.1: One-loop Feynman diagrams contributing to the azimuthal asymmetry for transversely polarized Møller scattering.

acceptance of the E158 Møller detector, the sensitivity of E158 to $A_T(\phi)$ is quite high. The E158 detector is well segmented in ϕ, but poorly segmented in θ.

This transverse asymmetry is not small. Given the fact that the CM energy at E158 is roughly 0.2 GeV, an azimuthal asymmetry at the order of $\alpha m_e/\sqrt{s} \sim 10^{-5}$ can be observed. This is two order of magnitudes larger than the parity-violating asymmetry, $A_{PV} \sim 10^{-5}$.

At this precision level, it is important to include the QED next-to-leading order (NLO) radiative corrections to $A_T(\phi)$. The NLO contribution to $A_T(\phi)$ comes mainly from two-loop scattering amplitudes for $e^-e^- \to e^-e^-$ and one-loop scattering amplitude for $e^-e^- \to e^-e^-\gamma$. The azimuthal asymmetry $A_T(\phi)$ is then modified as follows:

$$A_T(\phi) \equiv \alpha_T^{NLO} sin\phi. \tag{7.5}$$

where α_T^{NLO} is the NLO asymmetry coefficient. This leads to 1% increase in the magnitude of the asymmetry [83].

7.2 Data Analysis

In this chapter we will discuss the analysis of the data taken with a transverse electron polarization at beam energies 43 GeV and 46 GeV.

7.2.1 Data

The transverse-polarization data was collected for several days in Spring 2002, Fall 2002, and Summer 2003. E158 collected over 24×10^6 pulse pairs at two different beam energies (43 GeV and 46 GeV). The liquid hydrogen was used as a target for the data that was collected in Spring 2002 and Fall 2002, while the 8-gm carbon target was used in Summer 2003.

In order to clean the data from any outliers, certain cuts were applied to the data. These were the same cuts applied to the longitudinal-polarization data. Applying these cuts to the whole data set resulted in a reduction of about 16% in the number of pulse pairs [84].

7.2.2 *ee* & *ep* Transverse Asymmetries

The same method described in Chapter 4 was used to calculate both the longitudinal and trasnverse asymmetry. Only corrections due to the beam asymmetries were taken into account. Other corrections from background processes were not considered here.

Recalling equation 4.21

$$A_{meas} \equiv A_{PV} + A_T = A_{dx} \sin\phi + A_{dy} \cos\phi,$$

where the *dipole asymmetries*, A_{dx} and A_{dy}, are given by

$$A_{dx} = \frac{2}{N_j} \sum_i A_i^{reg} \sin\phi^i, \quad A_{dy} = \frac{2}{N_j} \sum_i A_i^{reg} \cos\phi^i,$$

where

$$\phi^i = \frac{2\pi i}{N_j} - \delta_j.$$

Here A_{PV} is the parity-violating asymmetry due to a small component of a longitudinal polarization of the beam. Therefore, we expect A_d to be few ppm while A_{PV} should be 0 for a 100% polarized beam.

Figure 7.2 shows the sin function of the experimental asymmetry, which meets our expectations. In a manner similar to the longitudinal Møller asymmetry, we first examine the distribution of the asymmetry and determine whether the data has outliers or not. In this context, we plot the asymmetry against data samples (*slugs*). This is shown in Figure 7.3. Despite the big statistical error on the second and the fourth slugs, the data seems to be clear from any outliers.

We expected the elimination of the systematic effects by the use of the asymmetry reversal techniques. The experimental asymmetry was then calculated for the different settings of the half-wave-plate and the energy. We also did not expect the asymmetry to vary much between the individual rings of the Møller detector. Figure 7.4 shows that, particularly in the OUT detector, there is no significant cancellation.

In conclusion, the observed azimuthal asymmetry in the Møller detector is $A_T^{Møller} = 2.7$ ppm, which is consistent with the theoretical predictions. In the ep detector, the observed transverse asymmetry is $A_T^{ep} = 2$ ppm, which is about five orders of magnitude smaller than the predicted asymmetry.

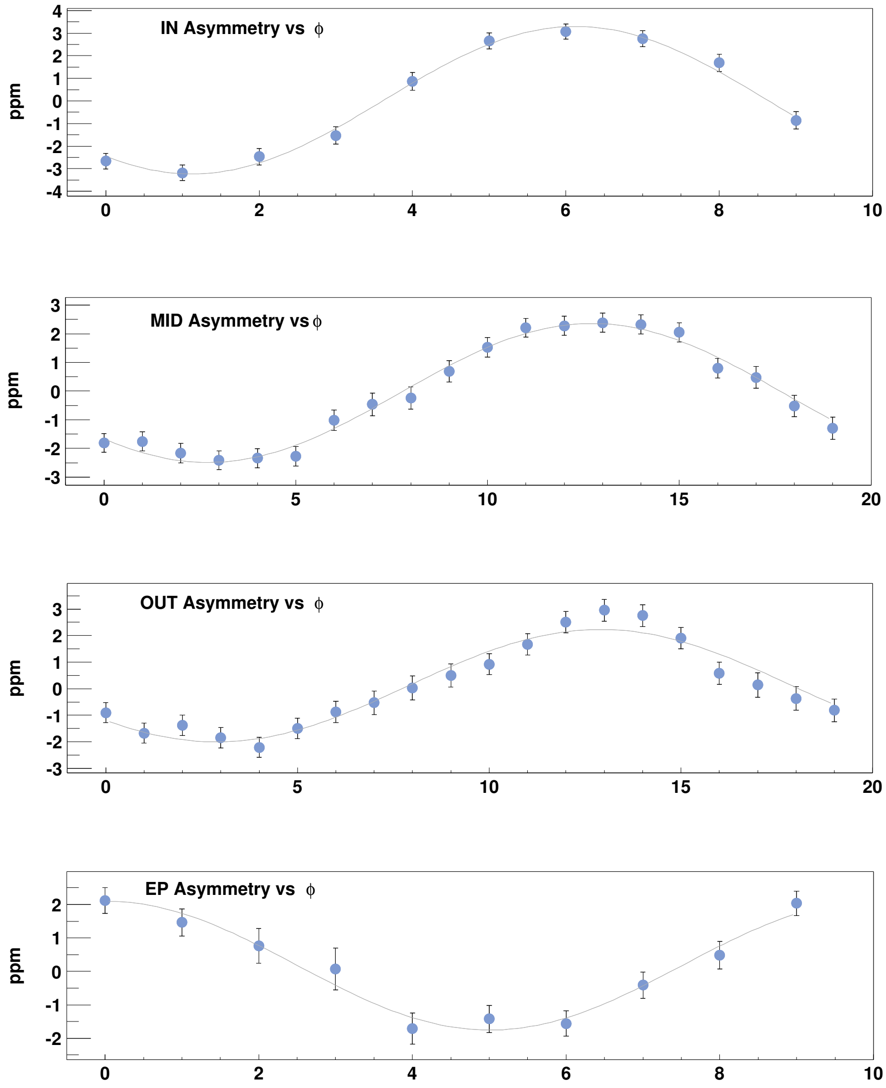

Figure 7.2: Transverse asymmetry for the individual rings of the Møller Detector and the Mott detector as a function of the azimuthal angle, ϕ, for Run III data set.

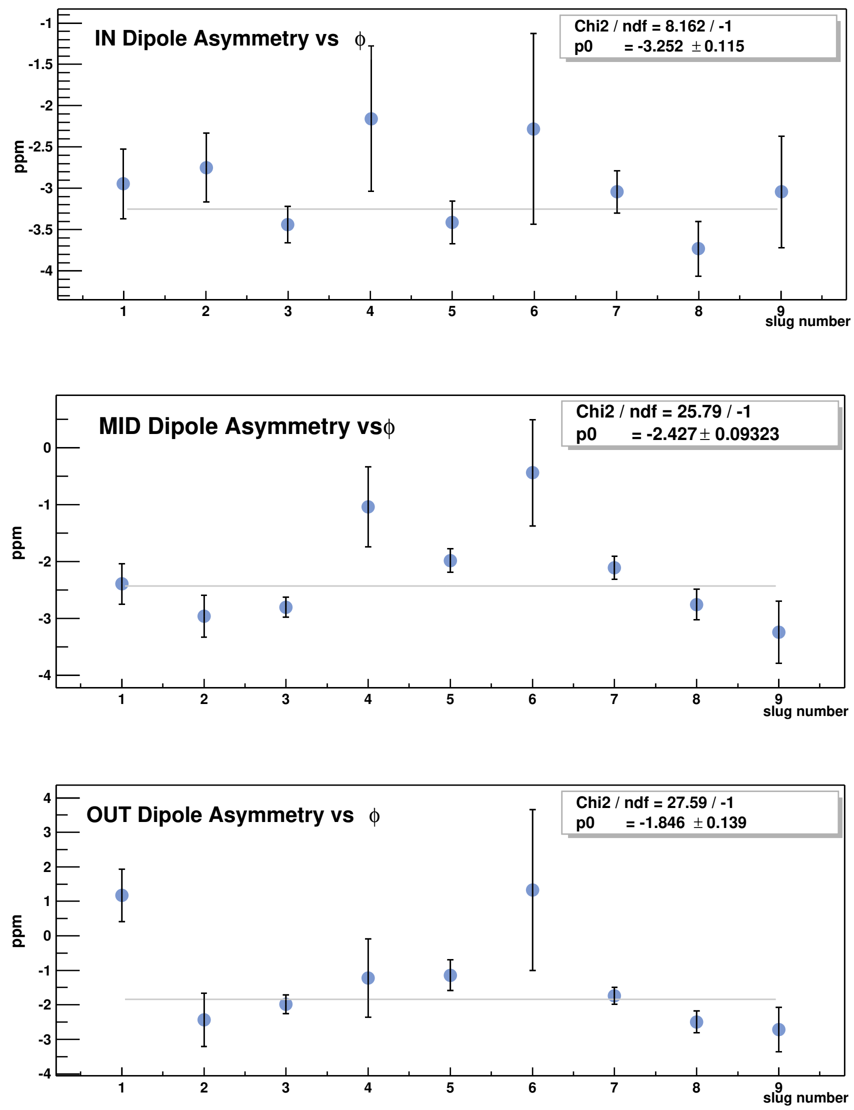

Figure 7.3: Transverse asymmetry for the individual rings of the Møller Detector as a function of slug number for Run II and Run III.

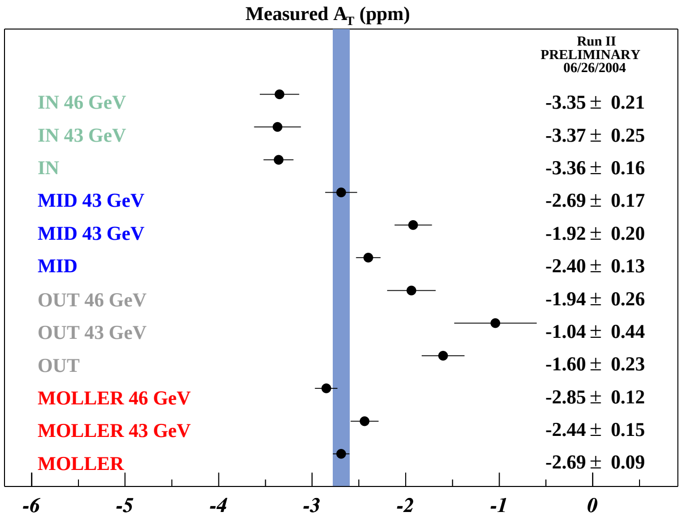

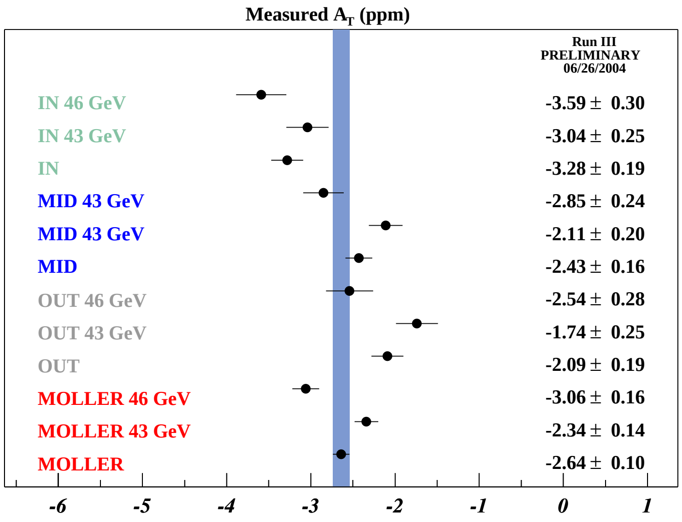

Figure 7.4: Transverse asymmetry of the Møller detector for Run II (*top*) and Run III (*bottom*).

A_T (ppm)	Monopole			Dipole X			Dipole Y		
Run I	**46 GeV**	**43 GeV**	**Total**	**46 GeV**	**43 GeV**	**Total**	**46 GeV**	**43 GeV**	**Total**
IN	-0.23 ± 0.26	-	-0.23 ± 0.26	0.15 ± 0.31	-	0.15 ± 0.31	-2.85 ± 0.30	-	-2.85 ± 0.30
MID	0.26 ± 0.21	-	0.26 ± 0.21	0.10 ± 0.27	-	0.10 ± 0.27	-2.67 ± 0.26	-	-2.76 ± 0.26
OUT	-	-	-	-	-	-	-	-	-
EP	0.16 ± 0.33	-	0.16 ± 0.33	0.26 ± 0.47	-	0.26 ± 0.47	-2.16 ± 0.39	-	-2.16 ± 0.39
Run II									
IN	-0.11 ± 0.20	-0.26 ± 0.23	-0.17 ± 0.15	0.35 ± 0.23	0.45 ± 0.27	0.05 ± 0.18	-3.35 ± 0.21	-3.37 ± 0.25	-3.36 ± 0.16
MID	0.54 ± 0.16	0.45 ± 0.19	0.51 ± 0.12	0.03 ± 0.18	-0.07 ± 0.22	-0.01 ± 0.22	-2.69 ± 0.17	-1.92 ± 0.20	-2.40 ± 0.13
OUT	-0.41 ± 0.18	-0.49 ± 0.35	-0.44 ± 0.17	0.01 ± 0.29	0.05 ± 0.58	0.03 ± 0.28	-1.94 ± 0.26	-1.04 ± 0.44	-1.60 ± 0.23
EP	0.13 ± 0.22	0.36 ± 0.26	0.22 ± 0.17	0.51 ± 0.32	0.12 ± 0.39	0.35 ± 0.25	1.71 ± 0.27	1.81 ± 0.33	1.75 ± 0.21
Run III									
IN	-0.09 ± 0.24	-0.09 ± 0.21	-0.01 ± 0.16	0.50 ± 0.32	0.25 ± 0.27	0.08 ± 0.21	-3.59 ± 0.30	-3.04 ± 0.25	-3.28 ± 0.19
MID	0.02 ± 0.20	0.01 ± 0.17	0.01 ± 0.13	0.26 ± 0.26	0.00 ± 0.22	0.12 ± 0.17	-2.85 ± 0.24	-2.11 ± 0.20	-2.43 ± 0.16
OUT	-0.05 ± 0.22	-0.01 ± 0.20	-0.02 ± 0.15	-0.41 ± 0.31	-0.29 ± 0.26	-0.34 ± 0.20	-2.54 ± 0.28	-1.74 ± 0.25	-2.09 ± 0.19
EP	0.05 ± 0.26	0.25 ± 0.21	0.17 ± 0.17	-0.80 ± 0.38	-0.02 ± 0.31	0.31 ± 0.24	1.68 ± 0.33	2.03 ± 0.27	1.89 ± 0.21

Table 7.1: Transverse asymmetry of the Møller and ep detectors for Runs I-III. Shown is the asymmetry for the two energy states as well as their average.

7.2.3 Other Transverse Asymmetries

Verifying the transverse asymmetry of the π detector was critical, since few hundred ppm in the π detector could easily result in 1 ppm in the ep transverse asymmetry. The transverse asymmetry of the π detector was found to be at the level of 1 ppm. The luminosity detector, on the other hand, shows a significant dipole asymmetry at the ppm level. The cause of this asymmetry is not yet clear, but it may result from higher-order beam systematics. Anlaysis using the *sliced* signals is occurring to detrmine the cause.

	Syst. Error	
Detector	**Run II (ppb)**	**Run III (ppb)**
Møller	15	1
ep	16	4
Lumi	33	9

Table 7.2: First-order uncertainties for the transverse asymmetry.

7.2.4 First-Order Beam Systematics

We followed the same procedure that was used to estimate the first-order systematics on the longitudinal data. In fact, the same suppression factors–the ratios between the difference in the regressed asymmetry for the two timeslots and the difference in the corresponding beam corrections for the two timeslots–were used in the transverse analysis. First-order uncertainties were then calculated according to

$$\delta_i^{beam} = \left|\frac{A_0^{reg} - A_1^{reg}}{A_{0_i}^{beam} - A_{1_i}^{beam}} \cdot A_i^{beam}\right|. \tag{7.6}$$

Here, A_i^{beam} are the beam corrections for the transverse asymmetry. Calculations showed that these errors are few ppb and can therefore be disregarded (Table 7.2).

Chapter 8

Future Experiments and Final Conclusions

8.1 Future Experiments at LHC

The Large Hadron Collider (LHC) currently under construction at the European Organization for Nuclear Research (CERN) is believed to hold the key to many new discoveries in particle physics. The LHC project was approved by the CERN Council in December 1994. Inside the 8.6-km-diameter LHC ring, two 7-TeV proton beams with a center-of-mass energy of 14 TeV and a luminosity of 10^{34} $\mathrm{cm}^{-2}\ \mathrm{s}^{-1}$ will collide with each other. The machine is expected to start operating in 2007.

8.1.1 LHC Plans

Several experiments are planned to participate at the LHC. The two largest experiments are a Compact Muon Solenoid (CMS) [85] and A Toroidal LHC Apparatus

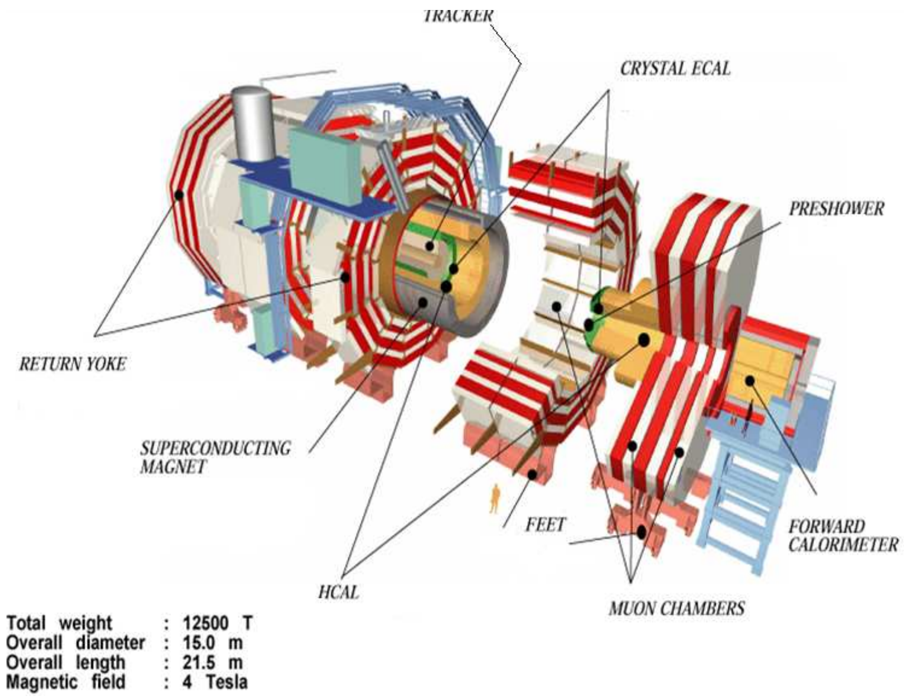

Figure 8.1: Cutaway view of the CMS detector.

(ATLAS) [86]. The CMS detector is designed to detect the Higgs boson, while the ATLAS detector will carry out precise measurements of the Standard Model parameters. Layouts of the CMS and ATLAS detectors are shown in Figures 8.1 and 8.2, respectively.

Two other experiments have been approved to run at the LHC: A Large Ion Collider Experiment (ALICE) and Large Hadron Collider Beauty (LHCb) [87] experiment. ALICE is a heavy ion detector designed to study the physics of nucleus-nucleus interaction at LHC energies. The goal is to study the physics of strongly interacting matter at extreme energy densities, where the formation of a new phase of matter–the quark-gluon plasma–is expected.

The goal of the LHCb experiment is to perform measurements of CP violating

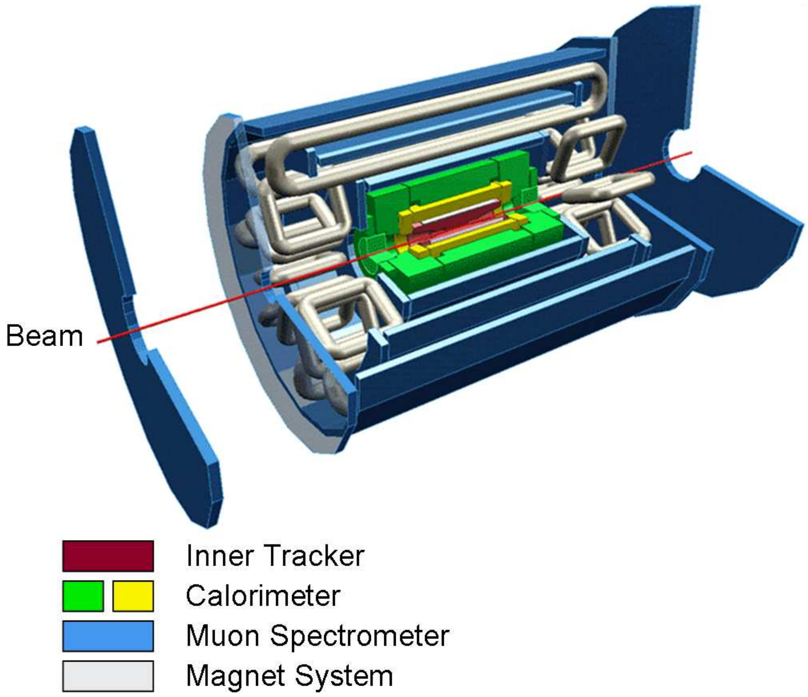

Figure 8.2: Cutaway view of the ATLAS detector.

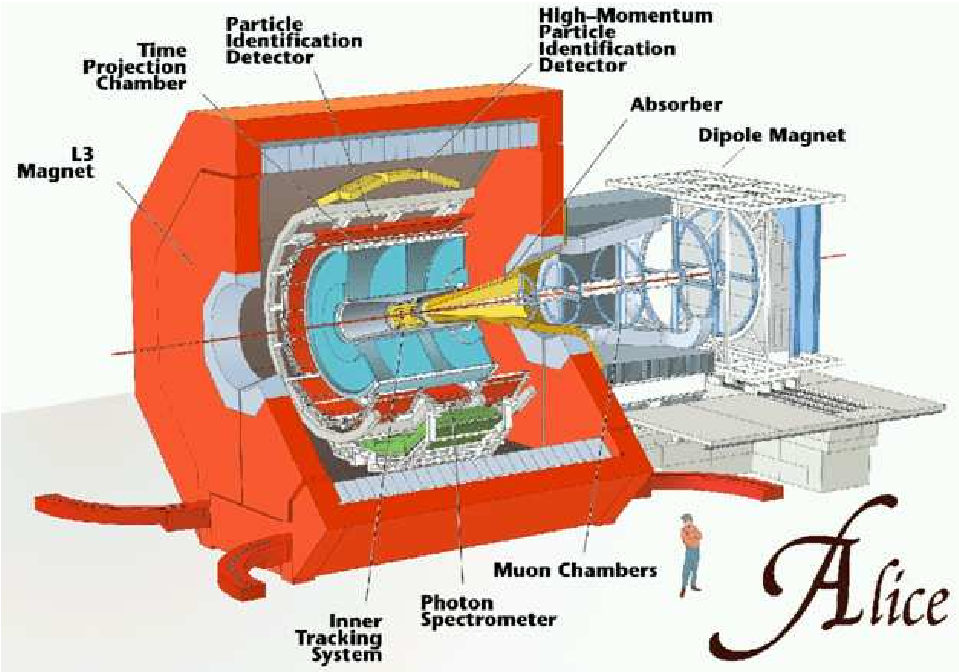

Figure 8.3: Cutaway view of the ALICE detector.

processes and rare decays in the B meson systems with unprecedented precision. By measuring CP violation in many different decay modes of B mesons and comparing the results with predictions from the Standard Model, researchers will surely lead to a new interpretation of physics beyond the Standard Model. Cutaway views of the ALICE and LHCb detectors are shown in Figures 8.3 and 8.4, respectively.

8.1.2 Possible SUSY Decays and Productions at LHC

Electroweak symmetry breaking now takes various approaches. Some of these approaches depend on the Higgs mechanism, while others are Higgsless. Ultimately, the experiment determines what form of electroweak symmetry breaking is applicable, making the Higgs boson the primary goal of the LHC project.

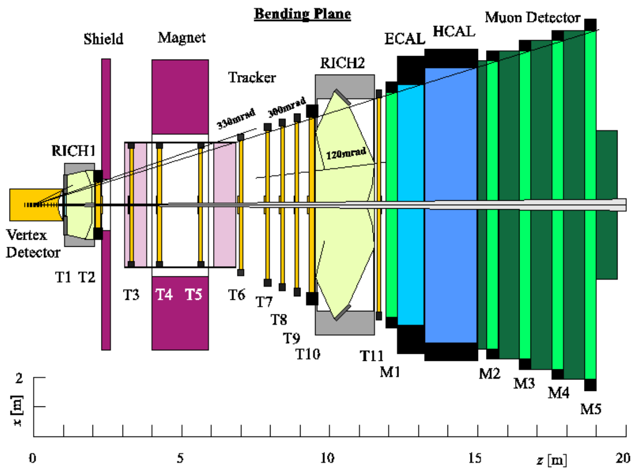

Figure 8.4: A schematic of the HLCb detector.

The symmetry of the MSSM is broken by two Higgs doublets giving five Higgs bosons: two CP-even Higgs bosons h^0, H^0, a CP-odd Higgs boson A^0, and a pair of charged Higgs bosons $H^{\pm}$. Although a discovery of the lightest Higgs boson at the LHC will favor Supersymmetry, failure to discover a Higgs boson below 130 GeV will rule out the MSSM [1].

The possible Higgs production channels at LHC would be [88]

$$
\begin{aligned}
gg &\rightarrow H, \\
VV &\rightarrow H, \\
q\bar{q} &\rightarrow V + H, \\
gg, q\bar{q} &\rightarrow Q\bar{Q} + H,
\end{aligned}
$$

where V refers to W or Z boson and Q refers to the heavy quarks, namely b and t.

[1] The upper limit on the lightest Higgs is $M_h \leq 130$ GeV at the loop level.

In addition to the Higgs production at LHC, the cross-section of a number of SUSY decays and productions will be measured. These cross-sections are well described by the mSUGRA model [2]. Within this model, the lightest charginos ($\tilde{\chi}_1^{\pm}$) have the following leptonic decay modes [88]:

$$\begin{aligned}
\tilde{\chi}_1^{\pm} &\rightarrow \tilde{\chi}_1^0 l^{\pm} \nu \\
\tilde{\chi}_1^{\pm} &\rightarrow \tilde{l}_L^{\pm} \nu \rightarrow \tilde{\chi}_1^0 l^{\pm} \\
\tilde{\chi}_1^{\pm} &\rightarrow \tilde{\nu}_L l^{\pm} \rightarrow \tilde{\chi}_1^0 \nu \\
\tilde{\chi}_1^{\pm} &\rightarrow \tilde{\chi}_1^0 W^{\pm} \rightarrow l^{\pm} \nu
\end{aligned}$$

Notice that in all above decay modes, one lepton ($l^{\pm}$) and missing energy ($\tilde{\chi}_1^0$) are produced. On the other hand, leptonic decays of $\tilde{\chi}_2^0$ give two leptons and missing energy.

The squarks and gluinos can also be studied at the LHC, and these can have strong decays [89]:

$$\tilde{q}_{L,R} \rightarrow q\tilde{g},\ q\bar{\tilde{q}}_{L,R},\ \bar{q}\tilde{q}_{L,R},$$

[2]There are several MSSM models. Each model is based on a certain mechanism of supersymmetry breaking. These models predict different experimental signatures. The Minimal Supergravity (mSUGRA) is the model most often used to interpret experimental data. It has only five free parameters and therefore, it is widely used to study production and decay of SUSY particles. The five free parameters of this model are

m_0	The common scalar mass at GUT scale,
$m_{1/2}$	The unifying gaugino mass,
A_0	The common trilinear term,
$\tan\beta$	The MSSM mixing angle: $\tan\beta = v_u/v_d$,
$\mu H_u H_d$	The sign of the Higgs bilinear term.

or they can have weak decays:

$$\tilde{q}_{L,R} \to q\tilde{\chi}_i^0, \quad \tilde{q}_L \to q'\tilde{\chi}_i^{\pm}, \quad \tilde{g} \to q\bar{q}\tilde{\chi}_i^0,\ q\bar{q}'\tilde{\chi}_i^{\pm},\ g\tilde{\chi}_i^0.$$

The left sleptons can decay to charginos and neutralinos through the following decays [88]:

$$\tilde{l}_L^{\pm} \to l^{\pm}\tilde{\chi}_{1,2}^0,\ \nu_l\tilde{\chi}_1^{\pm}, \quad \tilde{\nu}_l^{\pm} \to \nu_l\tilde{\chi}_{1,2}^0,\ l^{\pm}\tilde{\chi}_1^{\mp}.$$

The right sleptons only decay to neutralinos and mainly to the LSL:

$$\tilde{l}_R^- \to l^-\tilde{\chi}_1^0.$$

The total cross sections of all these decays have been studied [89].

8.1.3 CP Violation at LHC

One of the mysteries of elementary particle physics is the CP violation that can be generated in both weak and strong interactions. The first observation of a CP violation was made in 1964 [91] in neutral kaon decays. CP violation has been detected only in K measons. However, some experiments such as CLEO, BABAR, and BELLE are searching for CP violation in B measons so will LHCb. B meason has an enormous number of decay modes and, therefore, provides a wealth of opportunities to seach for a CP violation.

The CKM matrix, introduced by Kobayashi and Maskawa [90] to specifies the couplings between the quarks, is the cause of the CP-violating phenomena in the weak interactions

$$U = \begin{pmatrix} U_{ud} & U_{us} & U_{ub} \\ U_{cd} & U_{cs} & U_{cb} \\ U_{td} & U_{ts} & U_{tb} \end{pmatrix}. \tag{8.1}$$

The elements of this matrix generate nine unitary conditions. Six of these conditions can be presented as triangles in the complex plane using Wolfenstein's parameterization [92]. The angles of these triangles, α, β, and γ, can be obtained from direct measurements of the CP asymmetries in B meason decays.

Various decay modes of the B measons will be studied through the LHC, for example [87]:

$$
\begin{aligned}
B_d^0 &\rightarrow \pi^+\pi^-, \\
B_d^0 &\rightarrow K\pi^-, \\
B_d^0 &\rightarrow \rho^+\pi^-, \\
B_d^0 &\rightarrow J/\psi\, K_s.
\end{aligned}
$$

The LHCb detector also has the capabilities finding rare decays of B and τ measons.

8.2 BTeV at the Tevatron p-p̄ Collider

The Tevatron proton-antiproton (p-p̄) collider at the Fermi National Accelerator Lab (Fnal) is being prepared to host a new experiment called BTeV [93]. This experiment, which is expected to commence operation in 2009, will study CP violation in mixing and rare decays of beauty and charm quark states.

The BTeV experiment has almost the same goals as LHCb. Both experiments intend to run at luminosity of 2×10^{32} cm^{-2} s^{-1}. However, both experiments have advantages and disadvantages. One of the issues that favors LHCb, for instance, is the cross-section of the b production, which is expected to be five times larger at the LHC than at the Tevatron. On the other hand, BTeV and LHCb have

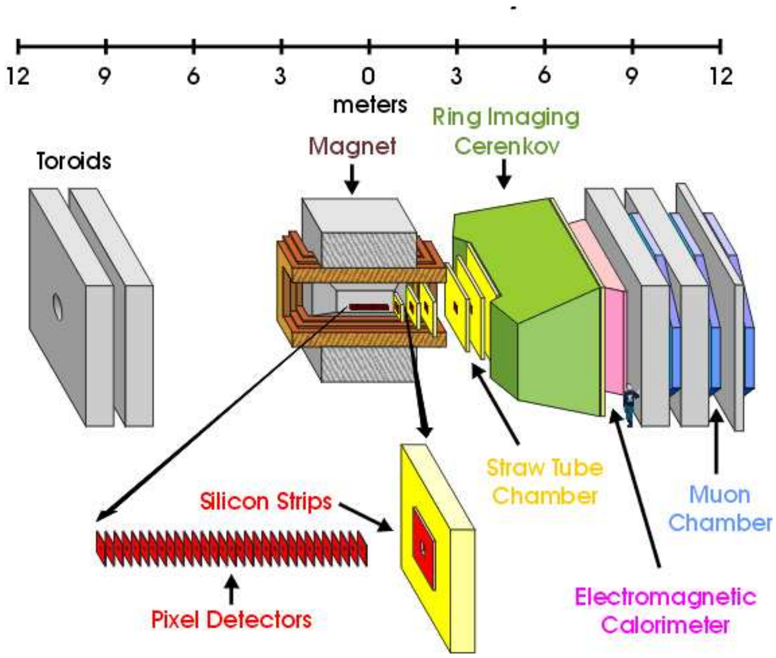

Figure 8.5: Layout of the BTeV detector.

comparable sensitivities in charged modes. However, BTeV is superior in modes with γ's and π^0's due to the pixel ditectors of the BTeV detector [94, 95].

A layout of the BTeV detector is shown in Figure 8.5. The main components of this detector consist of the following

1. Pixel Ditectors: to measure the positions of charged particles.

2. Silicon Strips: to measure the momenta of charged particles.

3. Ring Imaging Cherenkoc Detector (RICH): to identify charged particles.

4. Electromagnetic Calorimeter: to detect photons and electrons.

5. Muon Champers: to identify muons using a toroidal magnet.

8.3 Conclusions

The results from the first of three E158 run periods have been already published [96]. Here, we report on the preliminary results from the full data set. The SLAC-E158 experiment provided a very precise measurement of parity violation in Møller scattering. The measured parity-violating asymmetry is

$$A_{PV} = -128 \pm 14 \text{ (stat.)} \pm 12 \text{ (syst.)} \times 10^{-9}. \tag{8.2}$$

This is the most precise asymmetry ever measured in a parity-violating electron scattering. In the context of the Standard Model, A_{PV} result determines the weak mixing angle:

$$\sin^2\theta_{W_{\overline{MS}}} = 0.2330 \pm 0.0011 \text{ (stat.)} \pm 0.0010 \text{ (syst.)}. \tag{8.3}$$

This gives a Standard Model pull of 1.2σ.

In addition to the parity-violating asymmetry, we provided a measurement of the transverse asymmetry in Møller scattering and ep scattering. The observed asymmetries are $A_T^{Møller} = 2.7 \times 10^{-6}$ and $A_T^{ep} = 2 \times 10^{-6}$, respectively.

The consistency of the result with the theoretical prediction provides new limits at the TeV scale, comparable in sensitivity and complementary to other weak neutral current measurements at low Q^2. A limit of 0.9 TeV was set on the mass of the extra Z' boson in the SO(10) Model. At the 95% C.L., limits of 14 TEV and 6 TeV were set on the compositness scales Λ_{ee}^{+} and Λ_{ee}^{-}, respectively. Finally, a limit of 0.2 TeV was set on the ratio of the doubly-charged Higgs mass to the $ee\Delta$ coupling $g_{ee\Delta}^2/m_\Delta^2$.

Appendix A

Electronics Noise Test

As discussed in the Chapter 4, the OUT ring of the Møller detector was particularly sensitive to other hidden beam parameters. The χ^2 distribution of the OUT showed significant non-statistical fluctuations. One hypothesis was that, there is a significant variation in the shapes of the pulses, and that the electronics do not integrate pulses of different shapes in the same way. This variation in the pulse shapes is caused by the *banana* shape of the beam. The banana effects are small on the beam positions x and y. Therefore, the IN and MID detectors that were at most sensitive to x and y deal with constant pulse shapes. On the other hand, the OUT and LUMI detectors deal with variable pulse shape, generated by the beam banana shape [97]. The evidence that supports this idea was the linearity that the OUT detector shows under dithering but not under changes in the beam charge, Q. Dithering does not change the shape of the pulse. Changing Q, however, may change the pulse shape.

Luckily, the effect of pulse shape was measured. The idea was to produce two different pulse shapes. One is a square box and the second is a square box

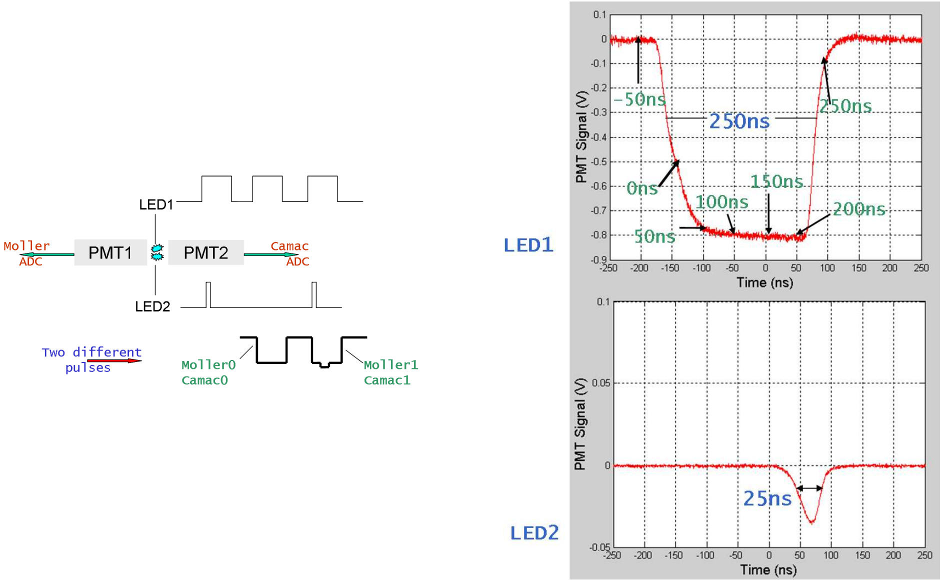

Figure A.1: A schematic illustrating the electronics noise test (left) and the actual obtained signals from the LEDs (right).

with a spike at the end. The signals were then measured by two different ADC's (Figure A.1). Therefore, a system of two PMTs looking at the same two LEDs was built in a dark box. One PMT was connected to the regular Møller detector electronics. The other PMT was connected to different electronics: *camac* that are known to have responses independent of the pulse shape. One LED fired on the even pulses and both fired on the odd pulses. This setup created two signals of different amplitudes proportional to the amount of light coming out from the LEDs, *i.e.*, LED_1 and $LED_1 + LED_2$. This means that the *moller* ADC should give two integrating values called, for instance, $moller^0$ and $moller^1$ depending on the ingoing signal. Similarly, the *camac* ADC does.

The quantity studied is the super-ratio

$$SR = \frac{R_{moller}}{R_{camac}} \tag{A.1}$$

where

$$R_{moller} = \frac{moller^1}{moller^0}, \quad R_{camac} = \frac{camac^1}{camac^0}. \tag{A.2}$$

In the ideal scenario, this ratio mathematically should be equal 1. However, it can be different than 1 for one of two reasons: the geometry of the setup that actually can be detected by just switching the PMTs, or the ADCs do not integrate the two different pulses in the same way.

The result of this test is shown in Figure A.2. The noise effect was found to be less than 1%. Therefore, it was neglected. It was obvious then that the hypothesis is wrong. Therefore, we worked on the *sliced* signal regression to minimize the residual systematics effects.

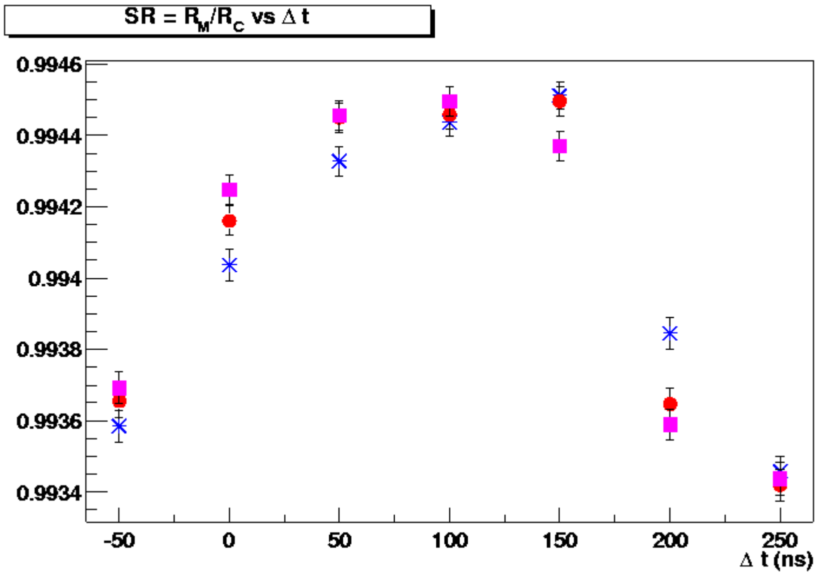

Figure A.2: The super-ratio SR as a function of pulse shapes. Different pulse shapes were created by varying the delay time between the two LEDs. The test was repeated more than once to make sure that the data reproduce. Therefore, the graph has three sets of points.

Bibliography

[1] S.L. Glashow, Nucl. Phys. **22**, 579 (1961).

[2] S. Weinberg, Phys. Rev. Lett. **19**, 1264 (1967).

[3] G. 't Hooft, Nucl. Phys. **B33**, 173 (1971).

[4] David Griffiths, *Introduction to Elementary Particles*, Hohn Wiley & Sons, Inc. (1987)

[5] Chris Quigg, *Gauge Theories of the Strong, Weak, and Electromagnetic Interactions*, Addison Wesley Longman, Inc. (1997)

[6] Donald H. Perkins, *Introduction to High Energy Physics*, Addison-Wesley Publishing Company, Inc. (1987)

[7] Atsushi Hosaka and Hiroshi Toki, *Quarks, Baryons and Chiral Symmetry*, Worl Scientific Publishing Co. Pte.Ltd. (2001)

[8] D. Abbaneo *et al.*, hep-ph/0112021 (2002).

[9] G.P. Zeller *et al.*, Phys. Rev. Lett. **88**, 091802 (2002).

[10] W. Marciano, Phys. Rev. **D20**, 274 (1979).

[11] W. Marciano and A. Sirlin, Phys. Rev. Lett. **46**, 163 (1981).

[12] A. Sirlin, Phys. Rev. **D22**, 971 (1980).

[13] P. Gambino and A. Sirlin, Phys. Rev. **49**, R1160 (1994).

[14] K. Ackerstaff *et al.*, CERN-EP/2002-053 (2002).

[15] K. Abe *et al.*, Phys. Rev. Lett. **86**, 1162 (2001).

[16] K.-P. Diener *et al.*, Phys. Rev. **D69**, 073005 (2004).

[17] S.J. Brodsky *et al.*, SLAC-PUB-9677 (2004).

[18] S.C Bennett and C.E. Wieman, Phys. Rev. Lett. **82**, 2484 (1999).

[19] A. Derevianko, Phys. Rev. Lett. **85**, 1618 (2002).

[20] P.A. Souder *et al.*, SLAC-E158 Prposal (1997).

[21] D. Armstrong *et al.*, Jlab Proposal PR02-020 (2001).

[22] E. Derman and W. Marciano, Ann. Phys. **121**, 147 (1979).

[23] C. Prescott *et al.*, Phys. Lett. **B77**, 347 (1978).

[24] W. Heil *et al.*, Nucl. Phys. **B327**, 1 (1989).

[25] P.A. Souder *et al.*, Phys. Rev. Lett. **65**, 694 (1990).

[26] B. Mueller *et al.*, Phys. Rev. Lett. **78**, 3824 (1997).

[27] K. Aniol *et al.*, Phys. Rev. Lett. **82**, 1096 (1999).

[28] A. Czarnecki and W. Marciano, Phys. Rev. **D53**, 1066 (1996).

[29] A. Czarnecki and W. Marciano, Int. J. Mod. Phys. **A13**, 2235 (1998).

[30] A. Czarnecki and W. Marciano, Int. J. Mod. Phys. **A15**, 2365 (2000).

[31] F.J. Petriollo, Phys. Rev. **D68**, 033006 (2003).

[32] A. Ferrogila, G. Ossola, and A. Sirlin, Eur. Phys. J. **C34**, 165 (2004).

[33] M.J. Ramsey-Muosolf Phys. Rev. **C60**, 015501 (1999).

[34] E.J. Eichten *et al.*, Phys. Rev. Lett. **50**, 811 (1983).

[35] B. Schrempp *et al.*, Nucl. Phys. **B296**, 1 (1988).

[36] J.F. Gunion *et al.*, Phys. Rev. **D40**, 1546 (1989).

[37] M.L Swartz, Phys. Rev. **D40**, 1521 (1989).

[38] G. Feinberg and S. Weinberg, Phys. Rev. Lett. **6**, 381 (1961).

[39] Hitoshi Murayama, hep-ph/0002232 (2000).

[40] J. Wess and J. Bagger, *Supersymmetry and Supergravity*, Princeton University Press (1991)

[41] Manuel Drees, hep-ph/9611409 (1996).

[42] Janusz Rosiek, Phys. Rev. **D41**, 13464 (1990).

[43] J. Erler *et al.*, Phys. Rev. **D68**, 016006 (2003).

[44] A. Kurylov *et al.*, hep-ph/0205183 (2002).

[45] M. Woods *et al.*, *Synchrotron Background Analysis for Run I*, E158 Technical Note **39**, (2003).

[46] K. Abe *et al.* (SLD collaboration), Phys. Rev. Lett. **79**, 804 (1997).

[47] B. Humensky, PhD Thesis, Princeton University, (2003)

[48] P. Horowitz and W. Hill, The Art of Electronics, Cambridge Uinversity press, Cambridge (1980)

[49] B. Humensky *et al.*, *SLAC's Polarized Electron Source Laser System and Minimization of Electron Beam Helicity Corrections for the E158 Parity Violation Experiment*, SLAC-PUB-9381 (2002).

[50] P. Mastromarino , *Beam Asymmetry Analysis for E158 for Run 1*, E158 Technical Note **34**, (2003).

[51] J. Gao *et al.*, Nucl. Inst. and Meth. **A498**, (2003).

[52] P.A. Souder, *in Lecture Notes on Strange Quarks and Parity Violation*, Syracuse University (2000)

[53] I. Younus, PhD Thesis, Syracuse University, (2003).

[54] I. Younus, *E158 Calorimeter*, E158 Technical Note **47**, (2003).

[55] D. Lhuillier, *Pion Detector Analysis*, E158 Technical Note **42**, (2003).

[56] M. Jones, *Luminosity Monitor April-June Run of E158*, E158 Technical Note **21**, (2001).

[57] W. Emam, *Run III Møller Asymmetry Analysis*, E158 Technical Note **57**, (2004).

[58] Z. Marshall, *Regression Using Covariance Matrices*, E158 Technical Note **51**, (2003).

[59] D. Relyea, *Run I Asymmetry Analysis*, E158 Technical Note **53**, (2003).

[60] K. Bega, *Run II - Summary of Moller Unblinded Results*, E158 Technical Note **52**, (2003).

[61] W. Emam, *Dithering Analysis*, E158 Technical Note **32**, (2003).

[62] Y. Kolomensky, *Run III Results*, Jefferson Lab, E158 Collaboration Meeting, (June 2004).

[63] Y. Kolomensky, *private communication*

[64] A. Vacheret, *Run III Higher Orders Systematic Studies*, E158 Technical Note **59**, (2004).

[65] Y. Kolomensky, *Higher Order Asymmetry Systematics*, E158 Technical Note **56**, (2003).

[66] A. Vacheret, *Run III Results*, Jefferson Lab, E158 Collaboration Meeting, (June 2004).

[67] M. Woods *et al.*, *Spot Size Analysis for Run I*, E158 Technical Note **40**, (2003).

[68] M. Woods, *Spotsize Analysis*, Jefferson Lab, E158 Collaboration Meeting, (June 2004).

[69] M.J. Musolf *et al.*, Phys. Rep. **239**, 1 (1994).

[70] C. Arroyo, *EP Inelastic Scattering Asymmetry Correction*, E158 Technical Note **33**, (2003).

[71] Z. Marshall, *Updated on Pion Analysis*, E158 Technical Note **64**, (2004).

[72] K.S. Kumar, *Update on Neutral Backgrounds*, E158 Technical Note **55**, (2004).

[73] J. Arrington *et al.*, Nucl. Inst. and Meth. **A311**, 39 (1992).

[74] I. Younus, *Linearity of the Møller Detector*, E158 Technical Note **27**, (2003).

[75] M. Cooke, *Probing Møller Detector Linearity with the Polarized Iron Foil and Light Filters*, E158 Technical Note **48**, (2003).

[76] D. Relyea, PhD Thesis, Princeton University, (2003).

[77] K.S. Kumar, PhD Thesis, Syracuse University, (1990).

[78] V. Zykunov, Yad. Phys. **66**, annot (2003).

[79] T. Kinoshita and A. Sirlin, Phys. Rev. **113**, 1652 (1959).

[80] Particle Data Group, K. Hagiwara *et al.*, Phys. Rev. **60**, 010001 (2002).

[81] A.O. Barus and C. Fronsdal, Phys. Rev. **120**, 1871 (1960).

[82] L.L. DeRaad and Y.J. Ng, Phys. Rev. **D11**, 1586 (1975).

[83] L. Dixon and M. Scheirber, Phys. Rev. **D69**, 113001 (2004).

[84] W. Emam, *Transverse Asymmetries*, UC Berkeley, E158 Collaboration Meeting, (April 2004).

[85] CMS Collaboration, CMS Proposal, CERN/LHCC/94-38 (1994).

[86] ATLAS Collaboration, ATLAS Proposal, CERN/LHCC?94-43 (1994).

[87] LHCb Collaboration, Proposal, CERN/LHCC 998-4 (1998).

[88] S. Khalil, Contemp. Phys. **44**, 193 (2003).

[89] CMS Collaboration, J. Phys. **G28**, 469(2002).

[90] M. Kobayashi and K. Maskawa, Prog. Theor. Phys. **49**, 652 (1973).

[91] J. Christenson *et al.*, PRL. **13**, 138 (1964).

[92] L. Wolfenstein *et al.*, PRL. **51**, 1983 (1983).

[93] Penny Kasper, *BTeV Status*, Presented at Beach2004, IIT, Chicago (2004).

[94] BTeV collaboration, *Some Comparisons of BTeV's Staged Physics Reach with LHCb*, (2004).

[95] Tomasz Skwarnicki, *private communication*

[96] P.L. Anthony *et al.*, Phys. Rev. Lett. **92**, 181602 (2004).

[97] P.A. Souder, *private communication*

VITA

NAME OF AUTHOR: Waled Sayed Abd Elzaher Emam

PLACE OF BIRTH: Cairo, Egypt

DATE OF BIRTH: December 10, 1974

GRADUATE AND UNDERGRADUATE SCHOOL ATTENDED:

- Syracuse University, NY, USA
- International Center for Theoretical Physics (ICTP), Trieste, Italy
- Ain Shams University, Cairo, Egypt

DEGREES AWARDED:

- M.S. in Physics, Syracuse University
- Diploma in High Energy Physics, 1999, ICTP
- B.S in Mathematics, 1997, Ain Shams University

AWARDS AND HONORS:

- Medal of Best Student in Mathematics from Ain Shams University, Cairo, Egypt, 1997.
- First Place in Ain Shams Mathematics Department, 1995-1997.

PROFESSIONAL EXPERIENCE:

- Visiting Student Researcher, Dept. of Physics, University of California at Berkeley, CA, 2003.
- Research Assistant, Dept. of Physics, Syracuse University, NY, 2000-2004.

- Teaching Assistant, Dept. of Physics, Syracuse University, NY, 1999-2000.
- Teaching Assistant, Dept. of Applied Mathematics, Ain Shams University, Cairo, Egypt, 1997-1998.